



Technisch-Naturwissenschaftliche  
Fakultät

# **Infrared photodetectors based on silicon–organic hybrid heterojunctions**

DISSERTATION

zur Erlangung des akademischen Grades

**Doktor**

im Doktoratsstudium der

**Technischen Wissenschaften**

Eingereicht von:

Mateusz Andrzej Bednorz

Angefertigt am:

Institute of Semiconductor and Solid State Physics

Beurteilung:

em. Univ. Prof. Dr. Günther Bauer (Betreuung)

o.Univ. Prof. Mag. Dr. DDr. h.c. Niyazi Serdar Sariciftci

Mitwirkung:

Dr. Thomas Fromherz

Linz, February, 2013

# Eidesstattliche Erklärung

Ich erkläre an Eides statt, dass ich die vorliegende Dissertation selbstständig und ohne fremde Hilfe verfasst, andere als die angegebenen Quellen und Hilfsmittel nicht benutzt bzw. die wörtlich oder sinngemäß entnommenen Stellen als solche kenntlich gemacht habe. Die vorliegende Dissertation ist mit dem elektronisch übermittelten Textdokument identisch.

Mateusz Bednorz

Linz 12.02.2013

# Acknowledgements

First of all I would like to thank Professor Günther Bauer for official supervision of this thesis and Dr Thomas Fromherz, a direct co-supervisor, for his guidance, help in experimental works, long hours of scientific discussions, a critical evaluation of the thesis and a kind and friendly attitude over past years. I also thank Gebi Matt for scientific discussions, a good company, a valuable advice and for sharing his experience during common work in the laboratory.

I would like to thank Professor Niyazi Serdar Sariciftci for allowing me to conduct my research at LIOS and be a member of his group, as well as for a good advice and many fruitful scientific and social discussions. Direct acknowledgements to: Saeed Zamiri for common work during first two years, Jacek Gašiorowski for help with electrochemistry measurements, Eric Głowacki for great ideas and help with the choice of materials and preparation, Philipp Stadler and Mujeeb Ullah for help with OFET fabrication and measurements, Alberto Montaigne for AFM measurements, Markus Scharber for interesting discussions and a good advice.

I also thank Professor Christoph Brabec from University of Erlangen for his constant support of our work and fruitful discussions and input during writing publications together.

I appreciate the assistance of Gerda Kalab and other technical personnel of LIOS and HLPHYS as well as invaluable help in maneuvering through bureaucracy from Petra Neumaier, Susi Schwind and other administration personnel.

I acknowledge all of my friends and colleagues from LIOS, HLPHYS and other institutes, encountered over last years. Thank you for sharing your cultures, your friendship, good humor, and great time spent together during all kinds of social activities, parties, and skiing–hiking trips.

Finally I would like to thank my family, my parents and my dear wife Božena for their love and support and my son Dominik for the joy, happiness and inspiration he brings to my life.

# Zusammenfassung

In dieser Arbeit werden hybride anorganisch - organische Heteroübergangsbaulemente vergleichend untersucht. Dioden, bei denen eine dünne Schicht des organischen Materials [6,6] phenyl-C<sub>61</sub> butyric acid methyl ester (PCBM, eine lösliche Form von Fullerenen), auf ein p-dotiertes Si Substrat aufgebracht wurde, wurden als Photodetektoren im infraroten Spektralbereich verwendet. Die elektrischen Eigenschaften dieser Dioden wurden mit Strom-Spannungs (J-V) - und Kapazitäts - Spannungsexperimente (C-V) untersucht. Ein auf dem Shockley-Read Formalismus beruhendes Modell wird vorgeschlagen, das den Diodenstrom als Generations-Rekombinationsstrom beschreibt. Es wird gezeigt, daß die Kapazität der Heterodiode in Sperrichtung als Kapazität einer Verarmungszone im Si in Serie mit der geometrischen Kapazität der PCBM Schicht verstanden werden kann. Darauf basierend werden für den p-Si/PCBM Übergang die relativen energetischen Lagen der Energiebänder im Si und PCBM aus den C-V Daten ermittelt und die Barrierenhöhe zwischen der Valenzbandkante in Si und dem LUMO (lowest unoccupied molecular orbit, niedrigstes unbesetztes Molekülenergieniveau) in PCBM konsistent mit  $\simeq 0.55$  eV abgeschätzt. Abweichungen von der Shockley-Read-Beschreibung des Diodenstromes, die vor allem für den Strom in Sperrichtung beobachtet werden, werden hinsichtlich einer Ladungsträgergeneration in der Si Sperrichtung, hinsichtlich thermischer Anregung von tiefen Störstellen in der organischen Schicht und hinsichtlich technologischer bedingter Kurzschlüsse diskutiert.

Der spektrale Verlauf des Photostroms der Heterodioden wurde mit Hilfe eines Fourierspektrometers untersucht, wobei die Heterodiode als externer Detektor für das Spektrometer verwendet wurde. Der energetische Einsatzzpunkt des Photostroms stimmt mit der Barrierenhöhe zwischen dem Si Substrat und dem organischen Film überein. Die Photostromerzeugung beruht auf der optischen Anregung von Elektronen im Si Valenzband in die LUMO Zustände des PCBM Films unter der eventuellen Beteiligung eines energetisch tief liegenden Zustandes in der Grenzschicht zwischen Si und PCBM. Photostromspektren gemessen bei unterschiedlichen Temperaturen, unterschiedlichen externen Diodenspannungen sowie an Dioden mit unterschiedlichen Metallen als Kontakte zu den organischen Schichten und mit verschiedenen PCBM-Modifikationen werden verglichen. Außerdem wurde der Einfluß einer zusätzlichen, wenige nm dicken LiF Schicht auf den Photostrom untersucht, die eine Verbesserung der Kontakteigenschaften von Al zum PCBM Film bewirkt. Als Referenz wurden außerdem Si-Metal Schottky Dioden untersucht, die im selben Herstellungsprozess, jedoch ohne organischen Film hergestellt wurden.

Heterodioden mit von PCBM unterschiedlichen organischen Filmen wurden ebenfalls untersucht. Diese Filme sind einerseits ein Perylen Diimid Derivat

(N,N'-Dimethyl-3,4,9,10-Perylentetracarboxylic diimide, DiMe-PTCDI) und andererseits Indigoide (Indigo und Tyros-Purpur). Mit diesen Materialien, die in den entsprechenden Kapitel genauer charakterisiert werden, konnte in auf p-Si basierenden Heterodioden die Responsivität signifikant verbessert werden. Allgemein Schlußfolgerungen hinsichtlich der Funktionsweise der organisch-anorganischen Heterodioden Photodetektoren sind am Ende dieser Arbeit zusammengefaßt.

Außerdem wurde eine ergänzende spektral aufgelöste Untersuchung des Photostroms in organischen Feldeffekttransistoren (OFETs) durchgeführt. Es wurde eine durch die Gatespannung aktivierte Absorption im nahen infraroten Spektralbereich mit einer Einsatzenergie von 0.5 eV und einem Maximum nahe bei 0.7 eV beobachtet und der Photogeneration eines  $C_{60}^-$  Anions (oder negativ geladenen Polarons) zugeschrieben, das bei größer werdenden Gatespannungen im Kanal des OFETs induziert wird. In der Literatur wird eine ähnliche Absorption von  $C_{60}^-$  berichtet. Durch weiterführende Untersuchungen von photoinduzierter Absorption (PIA) an einer Mischung aus Kupferphthalocyanin (CuPC) und  $C_{60}$  konnte diese Zuschreibung erhärtet werden.

Das detaillierte Verständnis der Funktionsweise der organisch-anorganischen Heterodioden ermöglicht sowohl eine weitere Verbesserung dieser Bauelemente hinsichtlich ihrer Anwendung als mit der Standardsiliziumtechnologie kompatible Infrarotphotodetektoren, als auch die Entwicklung von Photodetektoren basierend auf alternativen organischen Materialien. Der einfache Fabrikationsprozess dieser Detektoren ermöglicht eine direkte Implementierung in integrierte Schaltkreise aus Si, wobei die niedrigen Kosten, die großflächige Prozessierbarkeit und die Umweltverträglichkeit, die typisch für organische Materialien sind, eine solche Kombination aus organischer und anorganischer Elektronik besonders attraktiv erscheinen lassen.

# Abstract

In this work, a comprehensive study of hybrid inorganic-organic heterojunction devices is presented. Devices composed of a thin layer of organic material ([6,6] phenyl-C61 butyric acid methyl ester (PCBM) a soluble derivative of C<sub>60</sub> fullerene) deposited on a p-doped silicon substrate, were applied as photodetectors in the infrared spectral range. The electrical operation of these diodes was studied with current density-voltage (J-V) and capacitance-voltage (C-V) measurements. A thorough model for a recombination-generation current based on Shockley-Read derivation and a junction capacitance analysis assuming a depletion layer in silicon and a constant electric field in PCBM are proposed. For the interface between p-Si and PCBM, a band alignment scheme derived from energy values obtained experimentally from C-V measurement is presented. The barrier height corresponding to the difference between Si valence band and LUMO level of PCBM is consistently estimated to be  $\simeq 0.55$  eV. Deviations from the adapted Shockley-Read theory, most prominently observed for the reverse current of the diode, are discussed in terms of charge generation in the Si space-charge region, thermal excitations of deep traps in the organic film and technological shunts.

The photoresponse of the detectors was spectrally resolved using a Fourier-Transform-Infrared spectrometer, with the sample under investigation working as an external detector of the spectrometer. The onset of the spectrally-resolved photocurrent matches the interface barrier height. The photocurrent generation mechanism is ascribed to photoexcitation of an electron from the Si valence band into the LUMO level of PCBM, with a possible participation of an interface localized deep trap state in the organic material. Results of photocurrent measurements under varying temperatures, varying external bias, different material used as top metal electrode and different chemical structure of the PCBM derivative are presented. Moreover, the influence of a LiF/Al electrode instead of an Al one as a contact to the fullerene layer on photodiode operation is presented, as well as a complementary electrical and photoelectrical study of p-Si/metal devices, fabricated in the same technological process.

Heterojunction diodes comprising different organic materials were also studied within this work. These materials were: N,N'-Dimethyl-3,4,9,10-Perylentetracarboxylic diimide (DiMe-PTCDI), which is a derivative of perylene diimide and Indigoids (Indigo and Tyrian Purple). Using these materials, the performance of the diodes as infrared detectors could be improved significantly. A short characterization of each material is given in the corresponding chapters treating each heterojunction. A general conclusions on photodetectors operation and the mechanism of photocurrent generation are summarized at the end of this work.

Additionally, a complementary study of spectrally resolved photoconductivity in C<sub>60</sub> organic field effect transistor (OFET) is given. A gate activated absorption

in the NIR range with onset energy close to 0.5 eV and a maximum close to 0.7 eV was observed and ascribed to the photoexcitation of  $C_{60}^-$  anions (or negatively charged polarons), which are induced in the transistor channel by increasing gate voltage. The  $C_{60}^-$  absorption resulting in a similar spectrum was reported in the literature and was further endorsed within this work by a photoinduced absorption (PIA) experiment performed on the blend of copper-phthalocyanine (CuPC) and  $C_{60}$ , showing the correspondence of OFET photocurrent spectra and PIA spectra close to the onset energy.

Based on the detailed understanding of the diode operation principle, further improvements of the device with respect to its application as infrared photodetector compatible with standard Si technology as well as the development of photodetectors based on alternative organic semiconductors becomes possible. A simple fabrication process of the discussed device would allow a direct incorporation of infrared detectors onto any silicon circuit, utilizing organic semiconductors, characterized by low-cost, large-area processability, inherently low price of the materials and the potential for environmental sustainability.

# Contents

<b>Acknowledgements</b>	<b>3</b>
<b>Abstract</b>	<b>6</b>
<b>Table of Contents</b>	<b>9</b>
<b>1 Introduction and motivation</b>	<b>10</b>
<b>2 Theoretical background</b>	<b>12</b>
2.1 Basics of electronic transport in organic materials . . . . .	12
2.2 Overview of inorganic–organic hybrid heterojunctions . . . . .	14
2.3 Overview of photodetectors . . . . .	16
<b>3 Sample preparation procedures and measurements techniques</b>	<b>19</b>
3.1 Sample preparation procedures . . . . .	19
3.2 Measurement techniques . . . . .	22
3.2.1 Electrical studies . . . . .	22
3.2.2 Spectrally resolved photocurrent . . . . .	22
<b>4 p-Si/fullerene heterojunction photodiodes</b>	<b>27</b>
4.1 C <sub>60</sub> and PCBM material characteristics. . . . .	27
4.2 p-Si/PCBM heterojunction photodiodes . . . . .	30
4.2.1 Electrical studies of p-Si/PCBM heterojunction photodiodes	30
4.2.2 Photoresponse - spectrally resolved photocurrent . . . . .	50
4.2.3 Device improvement by adding LiF current enhancement layer to the top contact . . . . .	67
4.3 p-Si/C <sub>60</sub> heterojunction photodiodes . . . . .	71
4.4 Reference Schottky diodes . . . . .	76
<b>5 Spectrally resolved photocurrent of C<sub>60</sub> Organic Field Effect Transistors</b>	<b>82</b>
5.1 Fabrication and characteristics of C <sub>60</sub> OFETS . . . . .	82
5.2 Measurement setup of spectrally resolved drain-source photocurrent	83
5.3 Results, discussion and comparison with fullerene diodes . . . . .	84
<b>6 Other p-Si/organic heterojunction photodiodes</b>	<b>92</b>
6.1 p-Si/perylene diimide heterojunction diodes . . . . .	92
6.1.1 DiMe-PTCDI material characteristics . . . . .	92
6.1.2 Morphology of the organic layer . . . . .	93
6.1.3 Electrical characteristics . . . . .	95



6.1.4	Photoresponse - spectrally resolved photocurrent . . . . .	98
6.1.5	The influence of p-Si surface treatment on electrical characteristics and photoresponse . . . . .	105
6.1.6	Photodetector performance . . . . .	107
6.2	p-Si/Indigoids heterojunction diodes . . . . .	109
<b>7</b>	<b>Comparison of all studied heterojunctions, general conclusions</b>	<b>114</b>
<b>8</b>	<b>Summary and outlook</b>	<b>120</b>
	<b>Appendix</b>	<b>121</b>
<b>A</b>	<b>Cavity analysis</b>	<b>122</b>
<b>B</b>	<b>Analysis of applicability of Schottky model</b>	<b>125</b>
	<b>Bibliography</b>	<b>138</b>
	<b>Curriculum vitae</b>	<b>139</b>

# Chapter 1

## Introduction and motivation

The dawn of organic electronics might be associated with a development of the first conductive polymer, polyacetylene  $-(CH)_n$  [1, 2] by Heeger, Shirakawa and McDiarmid in the end of 1970's what eventually brought them the Nobel Prize in 2000. In the last decade, the technology of organic semiconductors has made a huge step towards a large-scale industrial production and the presence in the major markets. Samsung has produced millions of organic displays (OLED) for the consumer electronic market. As of 2012 organic solar cells have reached an efficiency of 10.6% [3], bringing them closer to commercial success. The first roll to roll printed organic solar cells haven been already produced by Konarka.

In the modern world concerned about energy and environmental issues the big attraction of organic electronics, frequently also labeled as "green electronics", is their outstanding low environmental impact. Such a benefit is attributed to: low material consumption, low temperature deposition and material production techniques with a low energy impact and the fact that most of the used organic semiconductors belong to the class of Hydrocarbons and as such they are non-toxic and degradable. These expectations can be confirmed by a life cycle analysis for organic solar cells, based on the standard production processes of organic electronic products, presented by Roes [4]. Overall, the environmental impacts of an organic solar cell technology were found to be significantly lower than for multi crystalline silicon technology, for CI(G)S technology and even for the thin film silicon technology. To summarize, organic semiconductors combine low-cost, large-area processability, with inherently cheap materials with the potential for environmental sustainability.

The detection of light in the near infrared (NIR) and infrared (IR) spectral range is a technology demand in many different branches of modern industry. The most important are: optical data transmission where wavelengths close to  $1.55\ \mu\text{m}$  are used, quality control and material identification in many industrial applications (biology, food industry, etc.), the imaging systems for transport and car industry. Moreover it is clear that the future development of information technology will feature an integration of optoelectronic building blocks, including detectors converting optical signals into electrical ones, into the integrated electronic circuit based on silicon.

Due to the transparency of Si for photon energies smaller than 1.12 eV, conventional detectors sensitive in the telecom-wavelength region are mostly based on inorganic compound (III-V) semiconductors, characterized by a direct band gap resulting in a high absorption coefficient [5]. They are all processed using

high-energy input epitaxial ultra high vacuum processes such as molecular beam epitaxy (MBE) or metallo-organic chemical vapor deposition (MOCVD) and are additionally toxic during various parts of their lifecycle, especially during the mining, extraction and purification stages. The processing and integration with the CMOS technology of the currently used detectors is thus not only the most expensive but also the most environmentally-unfriendly process step in the production of integrated optoelectronic circuits. Any technology that allows to circumvent these process steps has a huge impact on the ecological footprint of the future information technology, as it drastically diminishes energy consumption and environmental hazardous fabrication steps required for the InGaAs, AlGaAs, and HgCdTe semiconductors that are used as optoelectronic materials in the current optoelectronic technology generation. Other material used for light detection in the NIR range is germanium, which absorbs photons with energies higher than 0.65 eV. However, similar to detectors based on compound semiconductors, Ge has to be epitaxially deposited in order to integrate the device with electrical circuit. Additional disadvantage in comparison to for example InGaAs detectors is a very high dark current due to thermal generation of carriers.

In our previous work [6] it was shown that an inorganic-organic heterojunctions diodes, consisting of [6,6] phenyl-C61 butyric acid methyl ester (PCBM) a soluble derivative of C<sub>60</sub> fullerene, spin casted on a p-type Si substrate, can be used to detect NIR and IR radiation, even though both Si and PCBM are transparent in this spectral range.

A simple fabrication process of the discussed device would allow a direct incorporation of infrared detectors onto any silicon circuit.

In this work we present a comprehensive study of hybrid inorganic-organic heterojunction, composed of a thin layer of organic material deposited on a p-doped silicon substrate, applied as a photodetector in NIR and IR range. A detailed model of the electrical operation of the diode is given, supported by the results of current density-voltage (J-V) and capacitance-voltage (C-V) measurements, as well as spectrally resolved photoresponse studies. The archetype organic material used in the device was the PCBM, a soluble derivative of buckminster fullerene C<sub>60</sub> and the C<sub>60</sub> itself. The main studies and conclusions are given for the diode composed of those materials. However the heterojunctions of different organic materials were also studied: N,N'-Dimethyl-3,4,9,10-Perylentetracarboxylic diimide (DiMe-PTCDI) a derivative of perylene diimide and Indigoids: Indigo and Tyrian Purple, resulting in an improved performance. A short characterization of each material is given in corresponding chapters treating each heterojunction. Additionally a complementary studies of spectrally resolved photoconductivity in C<sub>60</sub> organic field effect transistor (OFET) is given as well as an electrical and photoelectrical study of reference metal/p-Si devices.

# Chapter 2

## Theoretical background

### 2.1 Basics of electronic transport in organic materials

The electronic phenomena in organic and hybrid semiconductor devices are strongly dependent on the charge carrier transport in the materials composing a device. The understating of transport mechanisms has been a fundamental issue in the research community since the early years of organic electronics, yet it is still a subject of an ongoing debate [7]. The films of disordered materials and organic materials in particular are characterized by the absence of translational symmetry with a three-dimensional periodic lattice, resulting in a random distribution of potential wells yielding a distribution of localized density of states (DOS). Moreover due to a weak intermolecular interaction of van der Waals type and a low dielectric permittivity a certain degree of charge self localization (the creation of polaron i.e. a charge with its associated lattice distortion) is present [8]. Therefore the percolation/hopping approach, assuming the existence of only localized states, was introduced (see Fig. 2.1a). It proved useful in explaining some often reported phenomena, such as temperature dependence of charge carrier mobility described by Mott [9] with variable-range hopping theory (VRH), resulting in conductivity  $\sigma \propto \exp -(T_0/T)^{1/4}$ , extended further with different exponents from 2 to 4 [10, 11] and simulated numerically by Bässler [12].

On the other hand many authors stated that crystallinity is not necessary to provide a material with semiconducting (band) properties, and the application of band theory is justified [13–15], despite the fact that in the case of molecular semiconductors the bands predicted by the molecular orbital calculations are in the range of  $\approx 0.01 - 0.1$  eV i.e. very narrow as compared to inorganic counterparts [16, 17].

The existence of localized states (traps), in addition to delocalized states [18], leads to the modified band theory like Poole-Frenkel model (see Fig. 2.1c) and multi-trap-and-release (MTR) model, which was applied to explain a temperature dependence of transport in polycrystalline sexithiophene in OFET configuration [19, 20]. The Pool-Frenkel theory assumes a charge transport through the conduction (and valence) bands with additional efficient traps (deep localized states). In order to contribute to the current, a trapped charge needs first to be thermally excited to a conductive band (delocalized states) and a direct hopping from trap to trap is not possible. In the Pool-Frenkel model, the mobility is as-

sumed field dependent, whereas in MTR the field dependence of mobility is not present and otherwise identical assumptions as in the Pool-Frenkel model apply. Important to point out is the fact that in the described models the traps are not necessary defined as either extrinsic or intrinsic (associated with a self-trapping effect i.e. a polaron) [21].

In Fig. 2.1b an other possible conduction mechanism is shown. This mechanism involves two bands, an extended one (in Fig. 2.1b the conduction band) and a localized one (traps in Fig. 2.1b). Provided that the trap density is large enough, hopping from one site to site of a nearest-neighbor hopping or variable-range hopping occurs [10, 22]. Such a hybrid model that assumes a transport via the delocalized band in parallel to a direct hopping over localized states is frequently employed to describe the conduction in low-mobility inorganic semi-conductors such as for example a non-stoichiometric GaAs [18, 23].

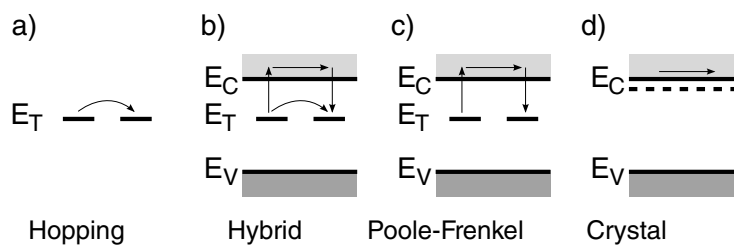


Figure 2.1: Conduction models presented above: a) hopping/percolation Conduction consists of infrequent jumps from one localized state to another. b) Hybrid (hopping + Poole - Frenkel). c) Poole - Frenkel (MTR). Conduction consists of charge being promoted to delocalized levels, where it can move freely. d) Crystal/band theory, conduction occurs in the conduction band (for electrons). Fig taken from [18].

In the scientific community, the existence of a mobility edge for transport in disordered material is well documented [24–26]. In his work from 1967 [27], Mott stated that if the ratio of the random fluctuations of a periodic potential to the bandwidth is lower than a critical value, the two energetical regions exist, namely the localized states in the low excitation-energy tail of the density of states function and the delocalized states. Those two regions are separated by a sharp energy level  $E_\mu$  that is called the mobility edge. In a highly disordered material, where the Fermi level is situated below (above)  $E_\mu$  for electrons (holes), transport is thermally activated and occurs at low temperatures dominantly via hopping mechanism or at high temperatures by band transport, when electrons (holes) can be effectively excited into states above (below)  $E_\mu$ . In this cases the

conductivity can be expressed by an Arrhenius type relation [28]:

$$\sigma \propto \exp\left(-\frac{E_{\mu} - E_F}{k_B T}\right) = \exp\left(-\frac{E_a}{k_B T}\right) \quad (2.1)$$

where  $E_a$  denotes the activation energy.

## 2.2 Overview of inorganic–organic hybrid heterojunctions

The initial studies of hybrid inorganic–organic heterojunction were reported by Forrest [29] in 1981. The research was focused on the investigation of physical properties of 3,4,9,10perylene-tetracarboxylic dianhydride (PTCDA). The reported PTCDA/p-Si heterojunction, contrary to previous believes, exhibited a rectifying behaviour. The following applications of hybrid heterojunctions were aiming at the analysis of free carrier density and defects of inorganic substrate [30, 31]. However the derivatives of PTCDA were over the years successfully applied in organic field effect transistors [32], photodetectors [33], as well as organic solar cells [34].

At first, a Schottky metal-semiconductor model was adopted as a description of the operation of hybrid devices, soon to be found not sufficient enough to tackle all aspects of inorganic–organic heterojunctions [35]. Nevertheless a direct Schottky-like modeling (described with Eq. B.1) of inorganic–organic heterojunctions, can still be found in literature, specially for a case of very thin organic layers of for example metal-fluorescein sodium salt (FSS) [36], PCBM [37], methyl red( $\text{NC}_6\text{H}_4\text{COOH}$ ) [38]. Such devices are sometimes referred to as a modified Schottky diodes as in the case of PTCDA and DiMe-PTCDI on sulphur passivated GaAs [39]. The analysis presented in Appendix B shows that such an approach is not applicable in case the diodes discussed in this work, composed of organic material deposited on p-Si substrate.

In order to overcome the shortcomings of the Schottky-like model, a more appropriate picture was introduced. A junction composed of intrinsic undoped organic layer and extrinsic inorganic semiconductor was thoroughly described in [40], featuring a thermionic emission over potential barrier at low current densities and a space-charge limited current in the organic material at high current densities. The barrier itself, pictured in Fig. 2.2 as  $\Phi_B$ , was – depending on the type of inorganic semiconductor – defined as an energy difference between lowest unoccupied molecular orbital (LUMO) or highest occupied molecular orbital (HOMO) of the organic material and the interface minimum of the conduction or the valence band in the inorganic material. The model developed for PTCDA, a hole conducting material, was applied also for the other p-type organic materials such as copper phthalocyanine (CuPc) and 3,4,9,10-perylene-tetracarboxylic-diimide (PTCDI) deposited on p-Si substrate [41], as well as for n-type DiMe-PTCDI deposited on both n- and p-type GaAs substrate [42]. Nevertheless a complimentary model for n-type organic material deposited on p-Si substrate was not reported.

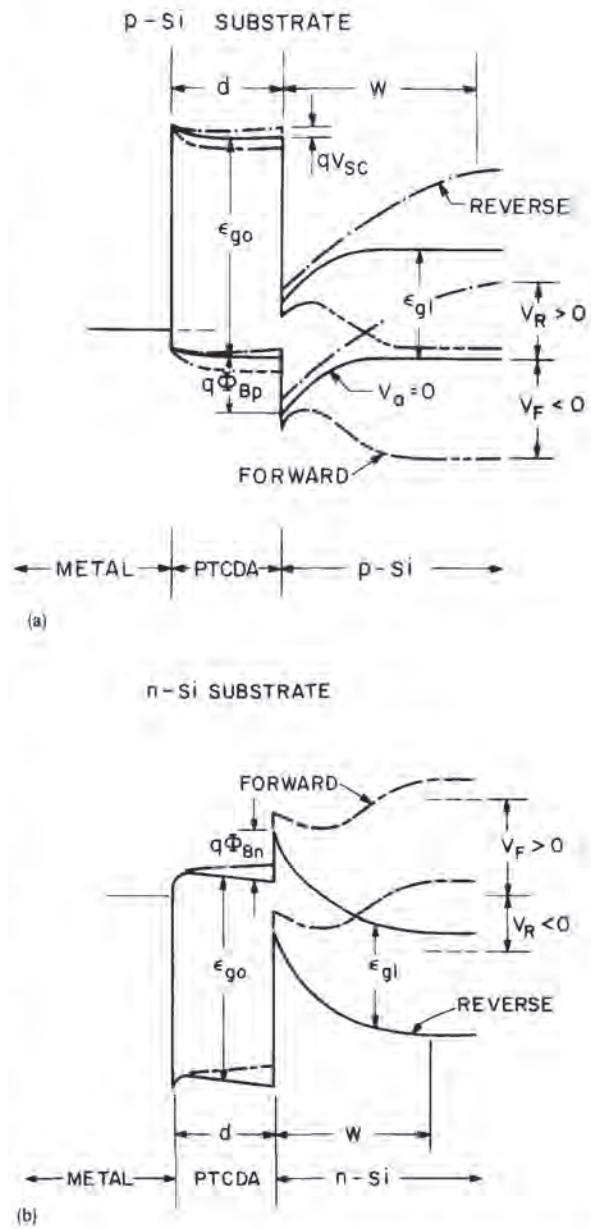


Figure 2.2: Band diagrams at thermal equilibrium and under voltage bias for diodes using ohmic metal/PTCDA deposited on (a) p-Si and (b) n-Si substrates. Figure taken from [40].

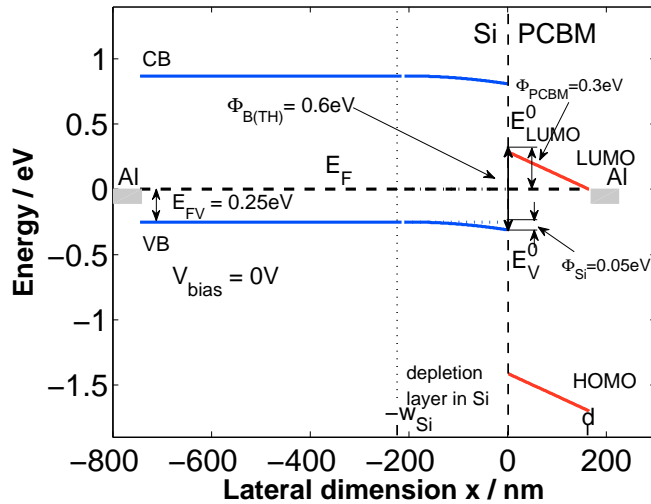


Figure 2.3: Band alignment at p-Si/PCBM interface. All values, except the Si wafer real thickness on the left side, are shown in scale and were calculated using the appropriate equations presented in Section 4.2.

The models sketched in Fig. 2.2 are not applicable for example to p-Si/fullerene devices, for which the band alignment is sketched in Fig. 2.3 (see details in Section 4.2). Contrary to the devices sketched in Fig. 2.2, for the p-Si/fullerene device the extended valence band states in Si do not overlay in energy with the conducting LUMO states in the fullerene layer. Therefore, injection of charge carriers from the inorganic to the organic layer is not possible via extended states aligned in energy.

In the case of silicon/fullerene hybrid heterojunctions the first devices were presented in the early 90's exhibiting rectification on both n- and p-type Si substrate [43, 44], probably due to non-perfect purity of the material in the early years of C<sub>60</sub> industrial production. Further attempts focused on p-Si/C<sub>60</sub> heterojunctions applied as a photovoltaic devices aiming at the extension of light harvesting spectra [45, 46].

However none of the cited publications presented a comprehensive model for the diode operation, adapting rather the classic diode equation in the form of Schottky formula (Eq. B.1).

## 2.3 Overview of photodetectors

Existing infrared detectors can be classified in two distinctive groups [47]:

- **thermal detectors** – the radiation increases the temperature of the active element, resulting in a change of the physical property that is measured and transformed into the output signal. Possible operation schemes feature:
  - bolometer - change of the electrical conductivity
  - pyroelectric - change of the internal electrical field
  - thermoelectric - change of the thermoelectric voltage



- golay cell - temperature induced gas expansion

Advantages: room temperature operation, linear spectral response, low cost

Disadvantages: low sensitivity, slow response

Application: IR spectrometry, thermography for various application, including medical, biological, firefighting, rescue service

- **photon detectors** – the incident photons interact with electrons of the lattice atoms (intrinsic detectors), impurity atoms (extrinsic detectors) or free electrons(photoemissive detectors), changing the energy distribution of the electrons. The photoexcited charges constitute the output signal. Possible operation schemes feature:
  - intrinsic photoconductive detectors: mercury cadmium telluride (MCT,  $\text{Hg}_{1-x}\text{Cd}_x\text{Te}$ ), broad spectral range 0.8-25  $\mu\text{m}$  due to simple bandgap tuning via stoichiometry ( $x$ ), lead sulfide (PbS) 1-3.2  $\mu\text{m}$ , lead selenide (PbSe) 1.5-5.2  $\mu\text{m}$ , indium antimonide (InSb) 1-6.7  $\mu\text{m}$
  - extrinsic photoconductive detectors: Si:In 3-5  $\mu\text{m}$ , Si:Ga 3-20  $\mu\text{m}$ , Ge:Ga 40-120  $\mu\text{m}$ . Extremely low temperature operation (few K) for astronomical applications
  - extrinsic photoconductive based on photoionization of impurities and localized charge traps [48, 49]: Mid-Bandgap Absorption (MBA) via ions implanted into Si ( $\text{H}^+$ ,  $\text{He}^+$ ,  $\text{Si}^+$ ), telecommunication range around 1.55  $\mu\text{m}$ , possibility of integration onto optoelectronic circuit on silicon-on-insulator (SOI) substrates. Expensive epitaxial methods of fabrication, Surface-State Absorption (SSA) via localized states at the Si/SiO<sub>2</sub> interface [50], possibility of integration with SOI based optoelectronic circuit (for example allowing for a photoresponse enhancing cavity design with micro-ring resonator [51]). Disadvantage high voltage operation required (>10 V)
  - photodiodes: Ge p-n and p-i-n homojunctions 1-1.6  $\mu\text{m}$ , disadvantage high dark current due to thermal generation of carriers, heterojunctions of ternary compound semiconductors: InP/In<sub>1-x</sub>Ga<sub>x</sub>As 0.7-2.6  $\mu\text{m}$ , GaSb/InAs<sub>1-x</sub>Sb<sub>x</sub> 1.7-4.2  $\mu\text{m}$ , InSb/InAs<sub>1-x</sub>Sb<sub>x</sub> 8-14  $\mu\text{m}$ . Advantages: high absorption coefficient due to direct bandgap, possibility of spectral range tuning by chemical composition and stoichiometry. Disadvantage: expensive epitaxial methods of fabrication
  - internal photo emission: Platinum silicide PtSi/Si: 1-5  $\mu\text{m}$ , IrSi/Si 2-10  $\mu\text{m}$ , Ge<sub>x</sub>Si<sub>1-x</sub> 2-25  $\mu\text{m}$ . Low-temperature operation, see details below
  - quantum well: GaAs/AlGaAs 8-20 $\mu\text{m}$ , InAs/InGaSb, InAs/GaSb 8-16  $\mu\text{m}$ . Straightforward spectral range tuning, sophisticated, costly design

Advantages of the whole group: very high sensitivity, low noise, possibility of integration into high resolution arrays, and integration with optoelectronic circuits.

Disadvantages of the whole group: highly spectrally dependent response, in most cases low temperature operation due to competing effect of thermal generation, high cost of materials and fabrication.

The presented list is not complete, summarizes however the most prominent concepts and devices. Since the interest of this work are silicon photodetectors sensitized by organic layer with the absorption process akin to internal photoemission, we will present a more detailed description of photoemissive detectors, as a directly comparable solutions, both from operation point of view and relatively easy similar processing.

The photoemissive detectors emerged in 1970s as a solution to reduce cost of infrared imaging for military applications. The first and most frequently used structure was p-Si/PtSi (platinum silicide) Schottky-barrier detector [52,53]. The operation of the detector bases on the photogeneration of hot hole in PtSi and subsequent emission over the barrier into the p-Si. Due to independence of performance to the doping level of silicon, minority carriers lifetime and the exact composition of an alloy, an outstanding spatial uniformity of the detector can be achieved, allowing for the fabrication of large area focal plane arrays. Different device architectures like IrSi/Si [54], or  $\text{Ge}_x\text{Si}_{1-x}$  [55] allowed for the extension of spectral range up to  $25\ \mu\text{m}$ , however the required operation temperature is even lower than for platinum silicide and the fabrication with MBE technology is by far more complicated and expensive.

The limitations of the technology discussed in the previous paragraph lie in the fact that the internal photoemission detectors suffer a great noise due to dark current of the Schottky diode originating from thermionic emission of majority charge carriers over the barrier. As a result a low temperature operation (40-80 K) is required to suppress the influence of dark current [47]. It will be shown in Appendix B that the hybrid diodes proposed in this work exhibit a dark current a few orders of magnitude lower, allowing for the room temperature operation.

# Chapter 3

## Sample preparation procedures and measurements techniques

### 3.1 Sample preparation procedures

Two major types of devices have been studied in this work. The solution processed p-Si/PCBM heterojunctions and physical vapor deposition processed p-Si/C<sub>60</sub> (p-Si/DiMePTCDI, p-Si/Indigo, p-Si/Tyrian Purple) heterojunctions. All devices were fabricated in the same geometry, shown in Fig. 3.1.

In both cases the initial step was the preparation of a substrate. For this purpose 15.15 mm<sup>2</sup> p-type Boron doped (100) silicon wafer-pieces (doping concentration  $N_A = 1.81 \cdot 10^{15} \text{ cm}^{-3}$ ) were used. One side polished wafers with 100 nm thermally grown oxide were purchased from Cemat Silicon. The substrate preparation steps involved:

- initial oxide strip with 5% HF solution removing a 100 nm oxide (optional strip of only 2/3 of sample surface to provide a buffer layer for contacting that prevents electrical shorts, in that case 1/3 of wafer is cover with annealed photoresist that masks it during HF etching).
- back contact formation - thermal evaporation of Al (70 nm), followed by annealing at 585 °C in 10:1 N<sub>2</sub>/H<sub>2</sub> reducing atmosphere to provide ohmic contact to p-Si [56, 57]. The temperature during annealing has to be higher than the eutectic temperature of both materials to prevent removal of contact during subsequent HF etching. Therefore an alloy of Si and Al is formed, what is generally not desired in semiconductor technology due to aluminium spikes in silicon that might appear during Si/Al alloy formation at such high temperature leading to electrical short [58]. However in our case the Al spikes are of no importance since the contact is spatially separated from active area of the device. Fig. 3.2 shows the I-V characteristics of the junction in which two Al/Si contacts were alloyed: Al(alloyed)/p-Si/Al(alloyed), resulting in ohmic behaviour in a wide range of temperatures with resistance slightly varying from 120 Ω to 100 Ω between 77 K and room temperature. On the other hand Fig. 3.3 shows the J-V characteristics at different temperatures of the junction in which only one Al/Si contact was alloyed: Al(alloyed)/p-Si/Al. It is clearly seen that the not-alloyed contact is not ohmic for the desire temperature range.

- sample cleaning using the RCA [59] cleaning procedure i.e. base bath (1:1:5 solution of  $\text{NH}_4\text{OH}/\text{H}_2\text{O}_2/\text{H}_2\text{O}$ ) - removal of organic contaminants, second oxide strip (HF) - removal of the native oxide, which grew during the last step. (The actual native oxide that grows on silicon wafer within hours in ambient conditions at room temperature was measured by ellipsometry to be around 1.2 nm.), acid bath (1:1:5 solution of  $\text{HCl}/\text{H}_2\text{O}_2/\text{H}_2\text{O}$ ) - removal of ionic contamination. Afterwards the sample was immediately transferred into inert atmosphere of glove box or into vacuum chamber of deposition system to avoid further oxidization of silicon surface.

in case of p-Si/PCBM sample:

- deposition of PCBM thin film by spin coating (1500 rpm for 40 s and 2000 rpm for 20 s resulting in  $\approx 165$  nm film for 3 weight percent PCBM solution in chlorobenzene).
- fabrication of top contacts by evaporation of appropriate metal electrodes. All steps done in inert atmosphere to prevent oxygen diffusion into the PCBM thin film.

in case of p-Si/C60 or p-Si/DiMe-PTCDI, p-Si/Indigo, p-Si/Tyrian Purple samples:

- silicon substrate in-situ baking at  $600^\circ\text{C}$  in high vacuum ( $10^{-7}$  mbar) for 15 min, for the removal of the hydrogen termination [60] that is known to be the result of HF dip [61] and other various contaminants resulting in a clean surface. It will be shown in Ch.6.1 that this step is crucial to achieve high performance of the photodetector.
- organic layer deposition by hot-wall-epitaxy (HWE) [62]. The HWE technique is a semi-closed epitaxy system which can be operated close to the thermodynamic equilibrium. As a consequence the weak Van der Waals interaction between the organic molecules can dominantly influence the growth dynamics [63] and hence support the formation of large crystalline domains [64] and highly ordered structures in general [65].
- immediate transfer of the sample into vacuum chamber of metal evaporator and fabrication of top metal contacts. Typically aluminum was used as a top metal contact, since it is known to form an ohmic contact with all studied organic materials. Additionally, different metal electrodes i.e. Ag and Au as well as LiF/Al electrode were fabricated as a top contact to PCBM layer. Typical electrode thickness was 70 nm, electrode area  $14\text{ mm}^2$ .

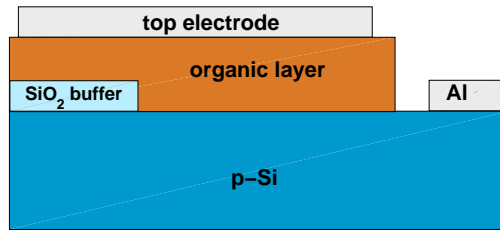


Figure 3.1: Schematic presentation of heterojunction structure.

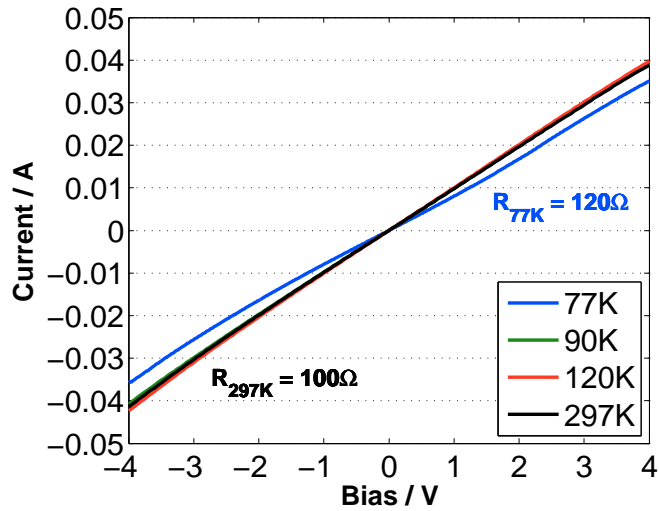


Figure 3.2: I-V characteristics of Al(alloyed)/Si/Al(alloyed) structure at different temperatures. Both contacts to Si were alloyed and are Ohmic.

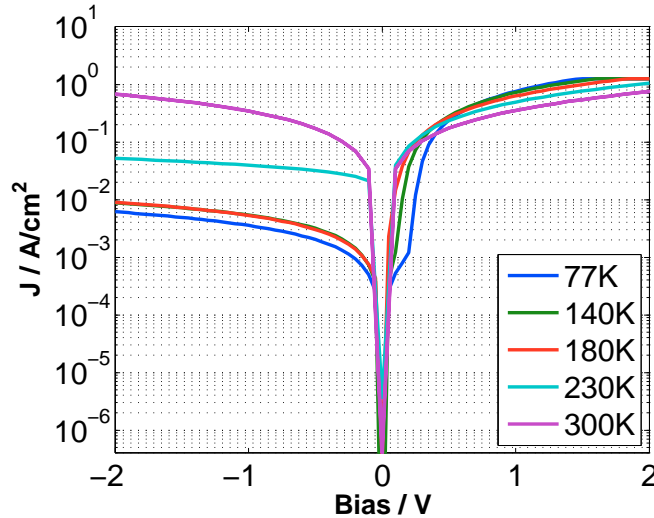


Figure 3.3: J-V characteristics of Al(alloyed)/Si/Al structure measured at different temperatures. The Al(alloyed)/Si contact is Ohmic and the other not-alloyed remains ohmic only close to room temperature.

## 3.2 Measurement techniques

In case of all measurements, except atomic force microscopy (AFM) and scanning electron microscopy (SEM), the sample was mounted in the sealed measurement containers and was not exposed to air during measurements. The mounting was performed under  $N_2$  atmosphere in a glove box system ( $O_2$  contents below 1ppm), to prevent the degradation of the device.

### 3.2.1 Electrical studies

The electrical studies involved current-voltage measurements at various temperatures and capacitance-voltage measurements. For the current-voltage characterizations a Keithley 236 Source-Measurement-Unit (SMU) was used. The temperature dependent measurements were done in Oxford Instruments liquid nitrogen cryostat system.

For the capacitance-voltage characterizations a Hewlett Packard 4284A LCR meter was used, with sample mounted in the sealed box connected directly to terminals of LCR meter without cables to minimize the possible influence of stray inductance.

### 3.2.2 Spectrally resolved photocurrent

Spectral photocurrent measurements were done with Bruker IFS66 Fourier-Transform Infra-Red (FTIR) spectrometer operating, depending on the sample, in fast scan mode or step scan mode (Fig. 3.4), with the sample itself working as an external photodetector of the spectrometer. The sample in the cryostat chamber was placed in the focal point of the spectrometer. The position of the sample was carefully tuned with XYZ translational stage to achieve the maximum short circuit current. In the step scan mode a mechanical modulator was introduced

in the beam path in front of the sample and the measured alternating current as well as mechanical modulator signal were fed into respectively signal and reference input of a lock-in amplifier (Stanford Research Systems SR830 DSP), the resultant amplified output voltage signal was fed into the spectrometer via DC external detector input. In the fast scan mode the alternating photocurrent was amplified by a J-V amplifier and fed into AC external detector input of the spectrometer.

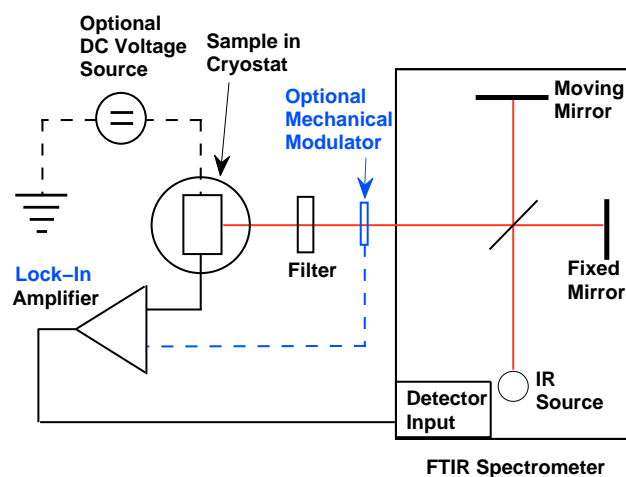


Figure 3.4: FTIR spectrometer setup for the measurements of spectrally resolved photocurrent of photodiodes. Fast-Scan configuration (black) and Step-Scan configuration (additional blue).

Typically a Tungsten near-infrared (NIR) lamp of the FTIR spectrometer and quartz beam splitter were used (optionally mid-infrared (MIR) globar with KBr beam splitter). The lamp spectra (Fig. 3.5) has been measured with pyroelectric detector(DLaTGS 301 with KBr window) of the FTIR spectrometer.

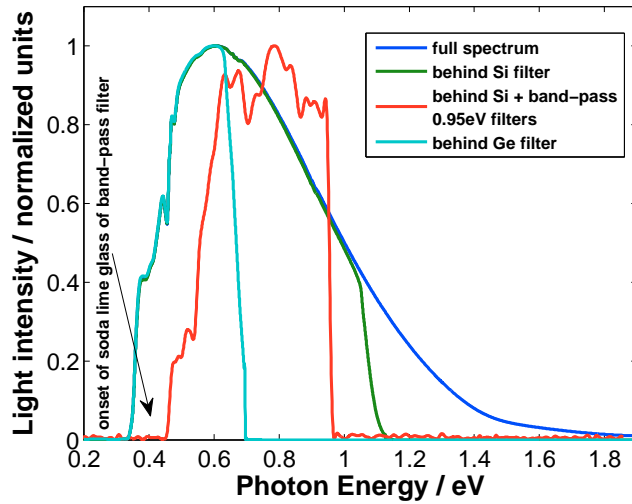


Figure 3.5: FTIR spectrometer NIR Tungsten lamp spectra behind different filters. The spectra were measured behind ZnSe window of the cryostat and normalized to the maximum intensity

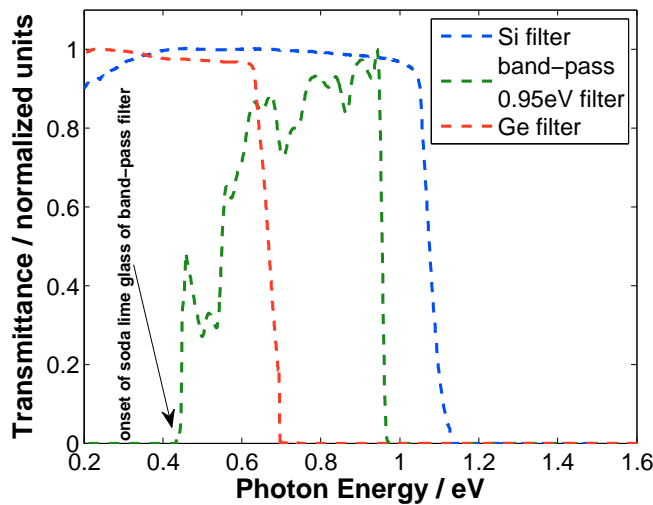


Figure 3.6: Transmittances of the used filters

The samples were illuminated from the Si side. In all cases a 5 mm thick silicon filter in combination with band-pass interference filter (cut-off at energies above 0.95 eV and below 0.44 eV due to absorption edge of soda lime glass of the filter) was placed in the beam path. Optionally germanium filter was used. The tungsten lamp spectra restricted by the used filters as well as the transmittance of the filters are shown in Fig. 3.5 and Fig. 3.6. Using of the band-pass filters enabled the measurement of the photocurrent at energies lower than silicon bandgap. Without the spectral restriction the dominant measured signal would come from the fundamental bandgap absorption of Si, and any potential infrared signal would be lower than the noise level, because of the limited dynamical range of the amplifier and analog-digital converter of the FTIR electronics.



Two optional scaling methods were applied in order to evaluate the actual responsivity of the photodetector  $R$ , defined for a given photon energy  $E$  as the ratio of the photocurrent  $I_S$  to the incident optical power  $P_I$  per detector area.

$$R(E) = \frac{I_S}{\text{area} \cdot P_I} \quad (3.1)$$

In both cases a commercial calibrated InGaAs photodiode (Thorlabs FGA21-CAL) was used to measure the optical power of the light source. Afterwards the investigated sample was placed in the identical position. For both the reference diode and the device under investigation the maximum intensity position was found with YZ translational stage. The responsivity of the calibrated photodiode is shown in Fig. 3.7. In the first method a broad band incandescent tungsten lamp was used. The lamp was operating at 1.75 A and 5 V, what corresponds to the radiator temperature 1900 K. The spectra of the lamp at given temperature  $T$  can be approximated as black body radiation, with spectral radiance  $U(\nu, T)$  following the Planck's law:

$$U(E, T) = \frac{2h\nu^3}{c^2} \frac{1}{\exp \frac{h\nu}{k_B T} - 1} \quad (3.2)$$

where  $\nu$  denotes the light frequency and  $h$ ,  $c$ , and  $k_B$  denote the Planck's constant, the speed of light and Boltzmann constant respectively. The measured photocurrent of the InGaAs detector under lamp illumination equals:

$$I_D = \int_{D_1}^{D_2} R_D(\nu) b U_N(\nu) d\nu \quad (3.3)$$

$$[A] = \int_{D_1}^{D_2} [A/W][W]$$

where  $R_D [A/W]$  is the responsivity of the InGaAs diode,  $D_1$  and  $D_2$  are the limits of  $R_D$ ,  $U_N$  is the normalized spectral radiance of the lamp and  $b[W]$  is the first scaling factor, which can be obtained from above equation after integration, leading to expression for the spectral radiance  $U$  in  $[W]$ :  $U[W] = b[W]U_N$ . Now the measured photocurrent of the investigated sample under lamp illumination equals:

$$I_S = \int_{S_1}^{S_2} a R_S^N(E) U(E) dE \quad (3.4)$$

$$[A] = \int_{S_1}^{S_2} [A/W][W]$$

where  $R_S^N$  is the normalized responsivity of the investigated sample measured with FTIR,  $a[A/W]$  is the second scaling factor, and  $S_1$ ,  $S_2$  are the limits of sample responsivity (from onset to filter cut off). Above equation yields the factor  $a$ , which gives finally the expression for the responsivity of the measured sample  $R_S[A/W]$ :

$$R_S[A/W] = a[A/W]R_S^N \quad (3.5)$$

Depending on the filter used in spectral measurement the same filter has to be used in calibration as well as in calculation and appropriate integral limits have to be chosen.

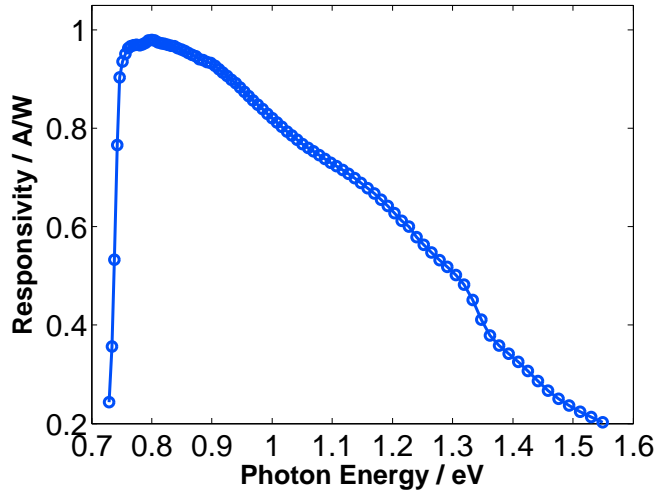


Figure 3.7: Responsivity of the calibrated commercial InGaAs photodiode (Thorlabs FGA21-CAL), used for calibration of the photodiodes investigated in this work.

The other simplified calibration method is based on a laser-diode emitting at  $1.55 \mu\text{m}$  (ROITHNER LASERTECHNIK RLT1550-30G). Light intensity of the laser-diode was measured with a commercial calibrated InGaAs photodiode placed in the position of the investigated sample. The exact position in the plane perpendicular to the beam for both reference diode and investigated sample, was determined using a X-Y translational stage by optimizing the measured photocurrent for each case. The area of the focused light spot (diameter  $\approx 1.7 \text{ mm}$ ), visualized by infrared indicating card, was smaller than both the reference diode area ( $0.03 \text{ cm}^2$ ) and the sample electrode area ( $0.08 \text{ cm}^2$ ). Therefore it was not necessary to know the exact area of the focused spot, in order to estimate the responsivity of the device under investigation. The light intensity was approximately  $200 \text{ mWcm}^{-2}$ . The spectrum was then scaled normalizing to the  $0.8 \text{ eV}$  energy ( $1.55 \mu\text{m}$ ).

# Chapter 4

## p-Si/fullerene heterojunction photodiodes

In this Chapter we will report on the electrical and photoelectrical studies of p-Si/fullerene heterojunctions. Starting from a short characteristics of the material itself and a brief report on similar structures reported in literature, we will continue with the development of a novel model for diode operation, basing on the results of C-V, J-V and J-V vs temperature characteristics. Afterwards the experimental results of sub-bandgap absorption observed in the studied devices are discussed. Additionally we will present the influence of a LiF/Al electrode instead of an Al one as a contact to the fullerene layer on photodiode operation. Finally a complementary study of p-Si/metal devices, fabricated in the same technological process, will be presented.

### 4.1 C<sub>60</sub> and PCBM material characteristics.

C<sub>60</sub> the most prominent of all fullerenes composes of 60 carbon atoms forming a so called 'Bucky Ball' with 20 hexagons and 12 pentagons, shown in Fig. 4.1. The name for the whole group of materials was given after Richard Buckminster Fuller an American author, engineer and designer, whose geodesic spheres or domes the C<sub>60</sub> molecule resembles. C<sub>60</sub> was discovered in 1985 by group of Prof Richard Smalley at Rice University in Houston. The discoverers Kroto, Curl and Smalley were awarded a Nobel Prize in Chemistry 1996. The closed cage nearly spherical molecule C<sub>60</sub> and related fullerene molecules have attracted a great deal of interest in recent years due to their unique structure and properties, leading to thousands of positions in literature. A detailed and comprehensive study of C<sub>60</sub> and fullerenes as a whole can be found in a classical text book by Dresselhaus [66].

From the physical point of view C<sub>60</sub> is a molecular n-type semiconductor capable of electron transport with electron mobility of 1 cm<sup>2</sup>/Vs [65,67], i.e. relatively high for organic materials and almost reduced hole transport mobility. Due to the large energy gap around 2.4 eV, estimated from photoemission and inverse photoemission studies [68] and defined as a difference between the lowest unoccupied molecular orbital (LUMO) and the highest occupied molecular orbital (HOMO), almost no free charge-carriers are available for transport at ambient temperatures. The optical bandgap is on the other hand close to 1.7 eV (see

Fig. 4.2 for  $C_{60}$  film absorption spectra). The onset energy of absorption is attributed to the generation of an electron-hole pair i.e. a Frenkel exciton in the material and the difference between optical and transport gap is attributed to the Frenkel exciton binding energy [68–70].  $C_{60}$  exhibits a typical for organic materials dielectric constant of around 3.9 [71]



Figure 4.1: Stereographic projection of  $C_{60}$  molecule and an example of a geodesic dome.

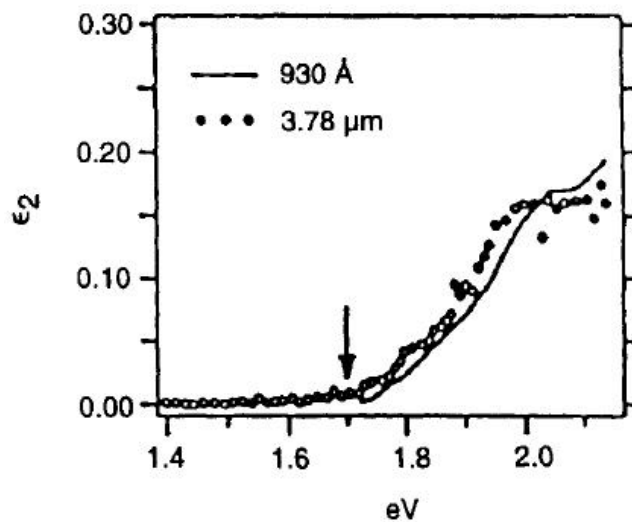


Figure 4.2: Spectral dependence imaginary part of dielectric function  $\epsilon_2(\omega)$  for two different thicknesses of  $C_{60}$  film deposited on quartz. The arrow marks the onset of absorption. Figure taken from [72].

Very important from the application point of view is a soluble derivative of  $C_{60}$ : methano-fullerene [6,6] phenyl-C61 butyric acid methyl ester (PCBM) (see Fig. 4.3), first synthesized in 1995 by J.C Hummelen et al. [73].

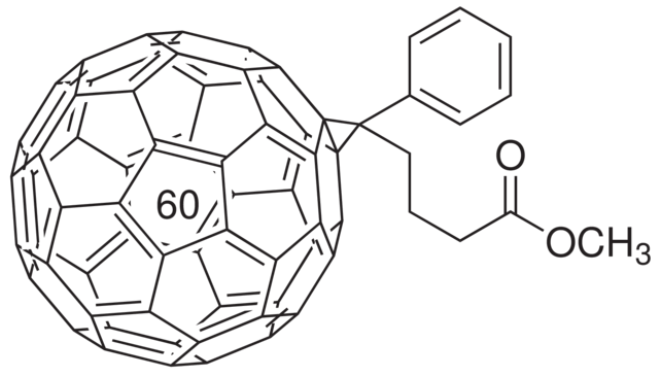


Figure 4.3: Chemical structure of PCBM.

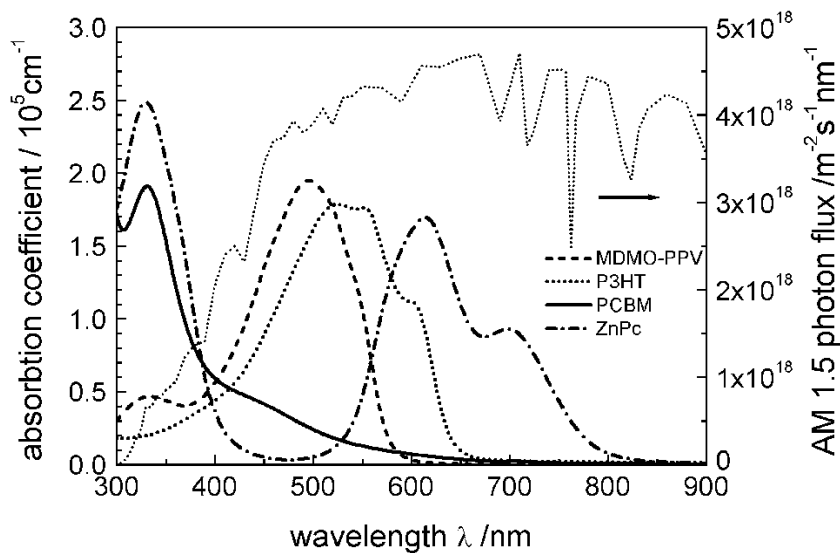


Figure 4.4: Absorption spectra of PCBM and other materials used in organic solar cells, in comparison with the standard AM 1.5 terrestrial solar spectrum. Figure taken from [74].

PCBM exhibits similar physical properties to  $C_{60}$  with an order of magnitude lower mobility [75] and the same absorption edge close to 1.76 eV (700 nm), shown in Fig. 4.4.

In contrast to pristine  $C_{60}$ , PCBM is soluble up to 5 weight percent in common organic solvents due to functionalization of the fullerene cage with a butyric acid methylester side-group [73]. Hence it can be deposited on a substrate in a wet processes like spin or dip coating, or doctor blading. This makes it a very interesting candidate for cheap, solution processed organic electronics.

The most important applications of derivatives of PCBM, already on commercial level are organic solar cells, which have strongly developed over the last decade, reaching the efficiency of 10% in 2012 [3]. PCBM, as a n-type semiconductor and a perfect electron acceptor is a component of so called bulk-heterojunction

solar cell which consist of a blend of PCBM and conjugated hole-conducting polymer [76].

Other interesting application of fullerenes in organic electronic is the Organic Field Effect Transistor where  $C_{60}$  acts as n-type semiconductor [65], such a device will be described in the details in Chapter 5.

## 4.2 p-Si/PCBM heterojunction photodiodes

### 4.2.1 Electrical studies of p-Si/PCBM heterojunction photodiodes

To understand the principles of operation of silicon/fullerene photodetector it is first essential to study the electrical properties of the heterojunction itself. A series of electrical measurements were done, including J-V, temperature dependence of J-V and C-V analysis. The rectifying behaviour of the diode is observed in J-V characteristics. The barrier height and band alignment at the interface were addressed in C-V measurements. The results of studies of temperature dependence of J-V characteristics will be used to explain the origin of reverse current of the diode. The model for the diode operation will be presented in details.

Fig. 4.5 shows the current density-voltage characteristics of an Al/p-Si/PCBM/Al device measured at room temperature and 77 K. The observed rectification ratio between -2 V to +2 V bias was  $2.6 \cdot 10^4$  at 300 K and  $5.7 \cdot 10^{10}$  at 77 K. The value at 300 K is almost an order of magnitude higher than the one for the p-Si/ $C_{60}$ /Ti device and in the same order as the values for the p-Si/ $C_{60}$ /Nb presented by Chen in [43] and in [77] or for the p-Si/ $C_{60}$ /Al with crystalline  $C_{60}$  film presented in [45], or even few orders of magnitude higher than the values reported in [46] for a p-Si/ $C_{60}$  (1  $\mu\text{m}$ )/Al device applied as solar cell.

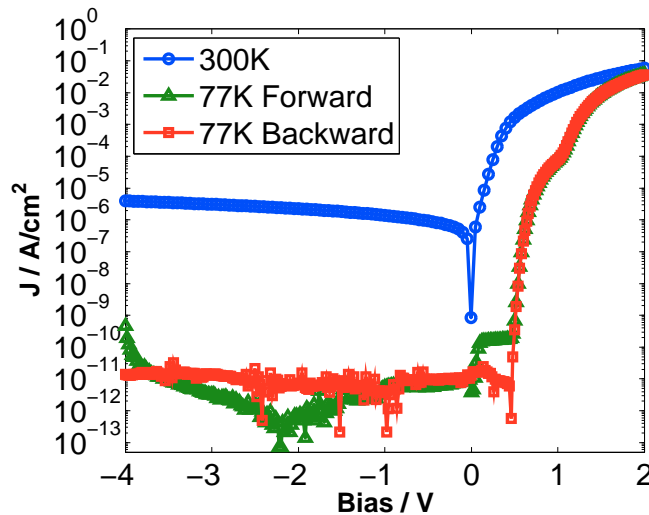


Figure 4.5: J-V characteristics of the Al/p-Si/PCBM/Al heterojunction measured at 300 K and 77 K. For 77 K the measurement from -2 V to +2 V i.e. forward direction and from from +2 V to -2 V i.e. backward direction is shown. For 300 K both directions yield the same result.

The rectifying behaviour seen in the J-V characteristics indicates directly the presence of a barrier for the charge carriers. Since the back Al/p-Si contact has been alloyed and is ohmic and Al is known to form an ohmic contact to PCBM [78, 79] the barrier has to be formed at the p-Si/PCBM interface.

To stress the significance of the silicon/fullerene interface for the rectifying behavior, an Al(alloyed)/p-Si/Al Schottky diode was fabricated in the same process as used for heterojunctions by omitting the PCBM spin-coating step. Fig. 4.6 shows that the p-Si/Al contact (as evaporated, without thermal treatment) is ohmic at room temperature. The linear fit yields the resistance of the Si wafer ( $35 \Omega$ ). Further details concerning the behaviour at lower temperatures and photocurrent measurement of p-Si/metal structures will be given in Section 4.4.

The ohmic character of the Al(alloyed)/p-Si/Al device at 300 K suggest also that the hybrid device Al(alloyed)/p-Si/PCBM/Al can not be treated as a modified Schottky diode with interfacial layer altering the barrier between metal and semiconductor. A simple analysis that is commonly applied to Schottky diodes, presented in Appendix B, reveals that the measured reverse dark current density and the Richardson constant  $A^*$  (a parameter describing the thermionic emission process governing the operation of a metal–semiconductor Schottky diode [5]) are much smaller than expected for the p-Si/Al diode at 300 K. The conclusion is that the thermionic emission is not the dominant mechanism describing the operation of investigated hybrid structures.

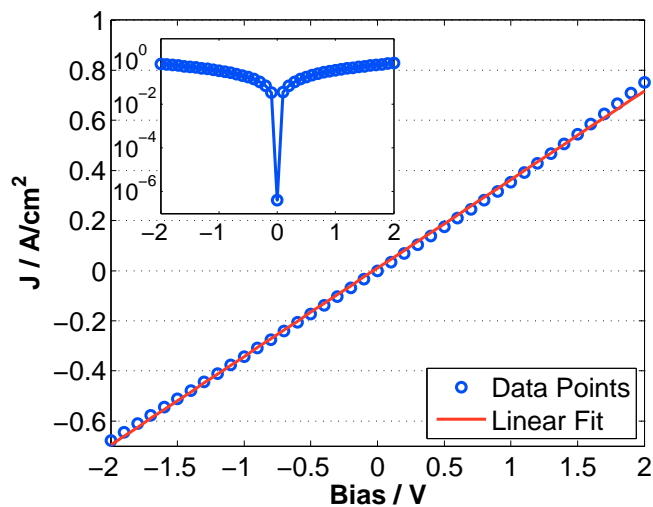


Figure 4.6: Current density-voltage characteristics Al(alloyed)/p-Si/Al metal–semiconductor junction measured at 300 K. Inset: semi-logarithmic plot.

#### 4.2.1.1 C-V measurements, theoretical model and results

In order to investigate the observed barrier a capacitance-voltage analysis has been applied. The capacitance has been recorded at frequency 1 kHz with 5 mV modulation voltage. To estimate the built-in potential and subsequently the barrier height of the investigated heterojunctions from C-V measurement using  $1/C^2$  plot we assume that at reverse bias the depletion layer and, thus, a space charge builds up in the Si and no localized charges are present in the PCBM

layer. The charge complementary to the one stored in the Si space charge region is thus exclusively located at the metal contact to the PCBM layer. To analyze the electric field and potential distribution and finally the capacitance of the space charge profile defined above we formulate Poisson's equation:

$$-\frac{\partial V^2(x)}{\partial x^2} = -\frac{|q| N_A}{\epsilon_0 \epsilon_{Si}} \quad (4.1)$$

where  $V(x)$  is the spatially varying electrical potential defined in the space charge region of Si and in PCBM layer,  $q$  is the elementary charge,  $N_A$  is the doping concentration in Si,  $\epsilon_0$  and  $\epsilon_{Si}$  denote vacuum dielectric permittivity and relative permittivity of Si respectively.

The electric field is obtained by integrating Poisson's equation:  $\vec{E}(x) = -\frac{\partial V(x)}{\partial x}$ . For  $x \in [-w_{Si}, 0]$ , where  $w_{Si}$  is the depletion layer width in p-Si and position  $x = 0$  corresponds to the p-Si/PCBM interface:

$$E_1(x) = \int_{-w_{Si}}^x \frac{-|q| N_A}{\epsilon_0 \epsilon_{Si}} dx'$$

$$E_1(x) = \frac{-|q| N_A (x + w_{Si})}{\epsilon_0 \epsilon_{Si}} \quad (4.2)$$

further integration gives the potential:

$$V_1(x) = - \int_{-w_{Si}}^x E_1(x') dx'$$

$$V_1(x) = - \int_{-w_{Si}}^x E_1(x') dx' = \frac{|q| N_A}{\epsilon_0 \epsilon_{Si}} \int_{-w_{Si}}^x (x' + w_{Si}) dx'$$

$$V_1(x) = \frac{|q| N_A}{\epsilon_0 \epsilon_{Si}} \frac{1}{2} (x + w_{Si})^2 \quad (4.3)$$

From Gauss's theorem the component of electric displacement field perpendicular to the interface  $\vec{D} = \epsilon_{Si} \epsilon_0 \vec{E}$  has to be continuous at  $x = 0$ :  $\epsilon_{Si} E_1(0) = \epsilon_{C60} E_2(0)$ , hence  $E_2(0) = \frac{-|q| N_A w_{Si}}{\epsilon_0 \epsilon_{C60}}$ .

For  $x \in [0, d]$ , where  $d$  is the thickness of PCBM layer, since there are not any unbalanced charges in the PCBM layer,  $E_2(x)$  is constant throughout the layer:

$$E_2(x) = E_2(0) = \frac{-|q| N_A w_{Si}}{\epsilon_0 \epsilon_{C60}} \quad (4.4)$$

$$V_2(x) = V_2(0) - \int_0^x E(x') dx' = V_2(0) + \frac{|q| N_A w_{Si}}{\epsilon_0 \epsilon_{C60}} x \quad (4.5)$$

where  $V_2(0) = V_1(0) = \frac{|q| N_A}{2 \epsilon_0 \epsilon_{Si}} w_{Si}^2$

$$V_2(x) = \frac{|q| N_A}{2 \epsilon_0 \epsilon_{Si}} w_{Si}^2 + \frac{|q| N_A w_{Si}}{\epsilon_0 \epsilon_{C60}} x \quad (4.6)$$



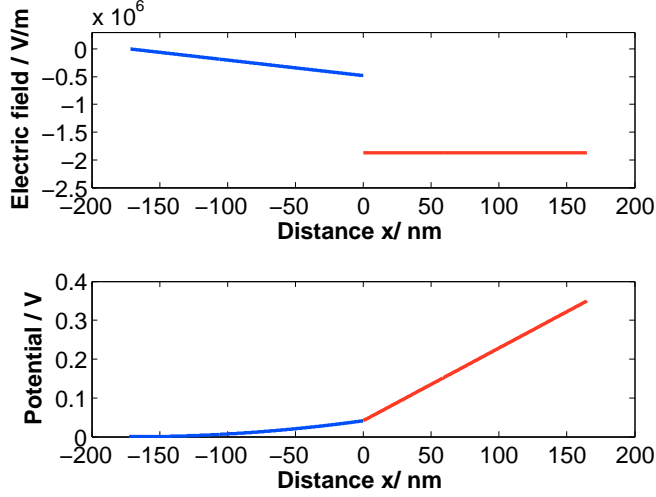


Figure 4.7: Electrical field and potential as a function of position in the device.  $x = 0$  denotes the interface, external bias  $V_{bias} = 0$ .

Fig. 4.7 shows the electric field and potential distribution based on above equations. The potential at the position of the metal contact to the PCBM layer  $V_2(d)$  is the total potential drop across the device, which at external bias  $V_{bias} = 0$  equals the built-in potential  $V_{bi}$  that results as a consequence of the equilibration of the electrochemical potential across the device:

$$V(d) = |V_{bi}| - V_{bias} \quad (4.7)$$

where  $V_{bias}$  is negative for biasing the diode in the reverse direction. Substituting Eq. 4.6 yields:

$$\frac{|q| N_A w_{Si}^2}{2\epsilon_0\epsilon_{Si}} + \frac{|q| N_A d w_{Si}}{\epsilon_0\epsilon_{C60}} = |V_{bi}| - V_{bias} \quad (4.8)$$

$$w_{Si}^2 + \frac{2d\epsilon_{Si}}{\epsilon_{C60}} w_{Si} - \frac{2\epsilon_0\epsilon_{Si}}{|q| N_A} (|V_{bi}| - V_{bias}) = 0 \quad (4.9)$$

$$w_{Si} = -\frac{d\epsilon_{Si}}{\epsilon_{C60}} \pm \sqrt{\left(\frac{d\epsilon_{Si}}{\epsilon_{C60}}\right)^2 + \frac{2\epsilon_0\epsilon_{Si}}{|q| N_A} (|V_{bi}| - V_{bias})} \quad (4.10)$$

The value of  $w_{Si}$  is a function of external voltage and has the following values depending on the external voltage:

$$w_{Si} = \begin{cases} w_{Si} > 0 & \text{if } V < |V_{bi}| \text{ reverse bias} \\ w_{Si} = 0 & \text{if } V = |V_{bi}| \text{ flat band condition} \\ w_{Si} \in Im & \text{if } V > |V_{bi}| \text{ injection} \end{cases} \quad (4.11)$$

The total capacitance of the structure equals:

$$C_T = \frac{dQ}{dV} = \frac{d(|q| N_A w_{Si})}{dV} = |q| N_A \frac{dw_{Si}}{dV} \quad (4.12)$$

$$C_T = |q| N_A \frac{2\epsilon_0\epsilon_{Si}}{|q| N_A} \frac{1}{2\sqrt{\left(\frac{d\epsilon_{Si}}{\epsilon_{C60}}\right)^2 + \frac{2\epsilon_0\epsilon_{Si}}{|q| N_A} (|V_{bi}| - V_{bias})}} \quad (4.13)$$

$$C_T = \frac{\epsilon_0 \epsilon_{Si}}{\sqrt{\left(\frac{d\epsilon_{Si}}{\epsilon_{C60}}\right)^2 + \frac{2\epsilon_0 \epsilon_{Si}}{|q|N_A}(|V_{bi}| - V_{bias})}} \quad (4.14)$$

hence the following expression for the inverse of capacitance square results:

$$\frac{1}{C_T^2} = \frac{1}{(\epsilon_0 \epsilon_{Si})^2} \left[ \left(\frac{d\epsilon_{Si}}{\epsilon_{C60}}\right)^2 + \frac{2\epsilon_0 \epsilon_{Si}}{|q|N_A}(|V_{bi}| - V_{bias}) \right] \quad (4.15)$$

The slope of  $1/C(V)^2$  line yields the acceptor doping concentration  $N_A$  and intersection with x-coordinate gives the  $V_{bias}^0$  which eventually gives the expression for  $V_{bi}$ .

$$\frac{1}{C_T^2} = 0 = \left(\frac{d\epsilon_{Si}}{\epsilon_{C60}}\right)^2 + \frac{2\epsilon_0 \epsilon_{Si}}{|q|N_A}(|V_{bi}| - V_{bias}^0) \quad (4.16)$$

finally

$$|V_{bi}| = V_{bias}^0 - \frac{|q|N_A}{2\epsilon_0 \epsilon_{Si}} \left(\frac{d\epsilon_{Si}}{\epsilon_{C60}}\right)^2 \quad (4.17)$$

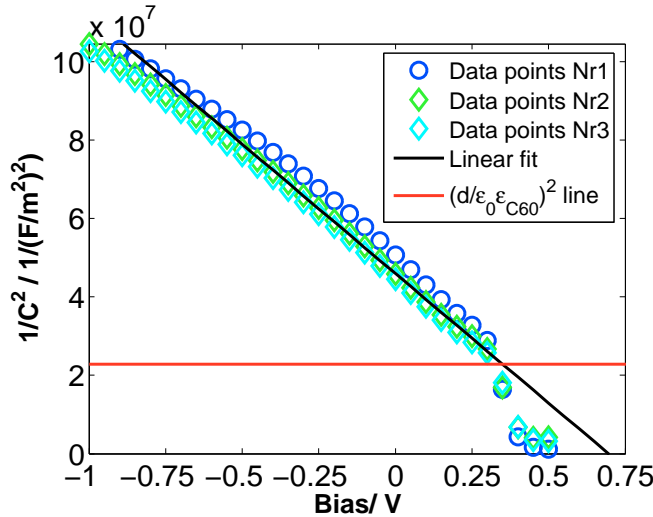


Figure 4.8:  $1/C^2$  vs  $V$  characteristics of Al/p-Si/PCBM/Al heterojunction for three different diodes fabricated in the same process. The intersection of orange line  $\left(\frac{d\epsilon_{Si}}{\epsilon_{C60}}\right)^2$  and data points is an alternative way to estimate  $V_{bi}$  from Eq.4.18.

Fig. 4.8 shows the  $1/C^2$  plot for three different samples fabricated in the same process, with the same thickness measured with AFM  $d = 165 \pm 12$  nm. The sharp decrease of  $1/C^2$  at voltages around 0.3V can be attributed to the additional charging at the interface at the onset of charge carrier injection. The small deviation from the linear behaviour at large negative bias (i.e. at small junction capacitance) is attributed to stray capacitances in parallel with the device.

Table 4.1: Values extracted from five different samples and average value of all parameters

Sample	$N_A / \cdot 10^{15} \text{ cm}^{-3}$	$V_{bi}/V$	$\Phi_{B(C-V)} / \text{ eV}$
Nr 1	1.74	0.39	0.64
Nr 2	1.81	0.35	0.60
Nr 3	1.85	0.33	0.58
Nr 4	1.82	0.42	0.67
Nr 5	1.8	0.35	0.6
Nr 6	2	0.41	0.66
Nr 7	1.4	0.35	0.6
Nr 8	1.8	0.41	0.66
Nr 9	2.2	0.41	0.66
<b>AVG</b>	<b>1.82</b>	<b>0.38</b>	<b>0.63±0.06</b>

Table.4.1 lists the parameters extracted from all measured samples (not all of them are shown on the plot for the sake of clarity), and calculated built-in potential and barrier height. The constant parameters were: dielectric constants of silicon and PCBM  $\epsilon_{Si} = 11.7$  and  $\epsilon_{C60} = 3.9$ , vacuum permittivity  $\epsilon_0 = 8.85 \cdot 10^{-12} \text{ F/m}$ , elementary charge  $q = 1.6 \cdot 10^{-19}$ . The discrepancies in slope and intersection values, which influence all other calculated parameters, are ascribed to samples variations due to non-uniformities of PCBM layer thickness and active electrode area, which are typical for spin-coated devices. The average value of doping concentration  $N_A = 1.82 \cdot 10^{15} \text{ cm}^{-3}$  is corresponding to a resistivity  $7.5 \Omega\text{cm}$  [5]. These value is in agreement with the resistivity values specified by the wafer supplier (5-10  $\Omega\text{cm}$ ) and those measured with four-point probe (6.3  $\Omega\text{cm}$ ).

The average value of built-in potential, from Eq. 4.17, is  $V_{bi} = 0.38 \pm 0.06 \text{ V}$ . The estimated uncertainty mainly results from the uncertainty of the PCBM layer thickness ( $\pm 12 \text{ nm}$ ).

An alternative way to evaluate  $V_{bi}$  comes directly from Eq. 4.15 for  $V_{bias} = V_{bi}$ :

$$\frac{1}{C_T^2} = \frac{1}{(\epsilon_0 \epsilon_{Si})^2} \left[ \left( \frac{d \epsilon_{Si}}{\epsilon_{C60}} \right)^2 + 0 \right] \quad (4.18)$$

The intersection of the  $\left( \frac{d}{\epsilon_0 \epsilon_{C60}} \right)^2$  line with the measurement data points (shown in orange line in Fig. 4.8) yields  $V_{bi}$ . The drawback of this approach is that only one measurement point is used in the evaluation. Nevertheless the obtained  $V_{bi} = 0.35 \text{ V}$  is equal within uncertainty to the one obtained from Eq. 4.17 using all measurement points in linear range. The fact that the intersection is at the knee of  $1/C^2$  means that beyond this voltage (the flat band condition) Eq. 4.15 is no longer valid and for higher voltages the injection starts and accumulation of charges at the interface occurs resulting in an increase of total capacitance.

The built-in potential  $V_{bi}$  is the sum of the potential drop in the depletion layer of Si  $V_{Si}^0$  and in the PCBM film  $V_{PCBM}^0$  at 0V external bias:

$$V_{bi} = V_{Si}^0 + V_{PCBM}^0 \quad (4.19)$$

Those two components of potential drop can be calculated from the expression for the potential vs  $x$  (Eq. 4.3 and Eq. 4.6), with  $V_{Si}^0 = V_1^0(0)$  (the integral of

potential from  $-w_{Si}$  to 0) and  $V_{PCBM}^0 = V_2^0(d) - V_2(0)$  (the integral from 0 to  $d$ ). If we apply external bias the total potential drop in the device equals  $V_{bi} - V_{bias}$ . Fig. 4.9 shows how does the total potential drop and the external voltage itself divide between the two layers, where the  $V_{Si}^V$  and  $V_{PCBM}^V$  were calculated as well from above equations with appropriate value of  $w_{Si}(V)$ . At 0 V external bias most of the built-in potential corresponds to  $V_{PCBM}^0 = 0.3$  eV with  $V_{Si}^0 = 0.05$  eV only. With increasing reverse bias the contribution of  $V_{Si}$  grows and finally at  $-2.3$  V the potential drop is equally shared between two sides of the interface.

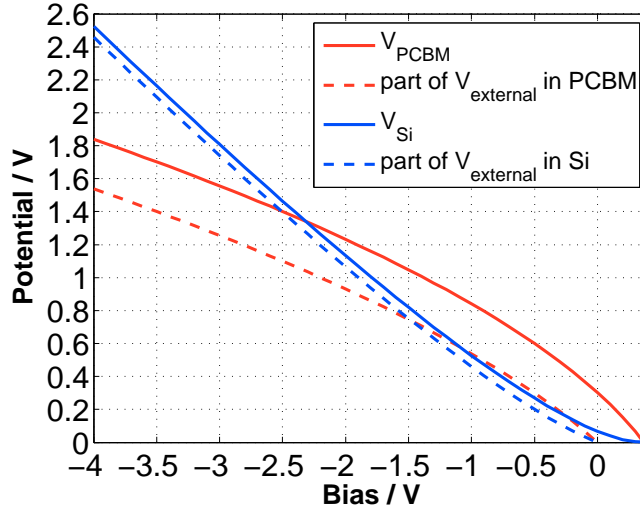


Figure 4.9: 1) Solid lines: Distribution of total voltage drop ( $V(d) = V_{bi} - V_{bias}$ ) in the device between depletion layer in Si and PCBM layer. 2) Dashed lines: Distribution of external voltage drop  $V_{bias}$  in the device between two layers.

In the following the band alignment at the interface is discussed. The exact positions of energy levels at any inorganic–organic interface is a subject of an intensive studies. The ideal model of interface band alignment presented for the first time by Mott in 1938 [80] and Schottky in 1939 [81] for metal-inorganic semiconductor interfaces known as the Schottky-Mott limit predicts the vacuum level alignment defining the barrier height by the values of ionization potential, electron affinity and the work function of the materials. The work function of Si is about  $-4.8$  V [82] and the reported LUMO level of PCBM measured electrochemically differs from  $-3.7$  eV [83] to  $-4.3$  eV [84], depending on the electrochemical setup used and a reference electrode in particular. In this work we performed an electrochemical measurement using cyclic voltammetry where glass-ITO covered with the studied material was used as working electrode, Ag/AgCl calibrated with ferrocene/ferrocenium redox couple as quasi-reference electrode and Pt as a counter electrode. For calculations of LUMO levels the value of half-peak ( $E_{1/2}$ ) of ferrocene/ferrocenium redox couple was referred to vacuum level using the values reported in [85]. For the LUMO energy level of PCBM the value of  $-4.2$  eV was obtained. The same setup was also used to study other investigated materials i.e. DiMe-PTCDI and Indigoids. Table 7.2 summaries values of LUMO level for all studied materials. Although the exact absolute values of organic material LUMO level and work function of p-Si can not be obtained

from comparison of various literature data, it can be concluded that the Fermi level ( $E_F$ ) of the p-Si is energetically below the LUMO of PCBM.

On the other hand the present studies predict the existence of a dipole at the interface that is defining the relative position between the vacuum level on both sides of the interface [86, 87], therefore the values of LUMO energy of pristine organic material and the work function of Si are not sufficient to identify the exact alignment of energy levels at the interface.

However, the built-in potential  $V_{bi}$  could be obtained experimentally from C-V measurement. We will use the expressions for the potential as a function of  $x$  throughout the device obtained from Poisson's equation to calculate the energy levels as a function of  $x$ . Those expressions depend on  $V_{bi}$  through the value of  $w_{Si}$  (Eq. 4.10). At thermal equilibrium and 0V external bias the  $E_F$  is constant throughout the whole device. Other known parameters are the bandgap of Si at room temperature 1.12 eV [5], the bandgap of PCBM 2.4 eV [76] and the location of  $E_F$  in p-Si relative to the valence band, which can be calculated for a given doping concentration from:

$$E_{FV} = kT \ln\left(\frac{N_V}{N_A}\right) \quad (4.20)$$

where  $N_V = 2.66 \cdot 10^{19} \text{cm}^{-3}$  is the effective density of states in the valence band, for silicon at 300 K [58], resulting in  $E_{FV} = 0.25 \text{ eV}$ . In the following  $E_F$  in the Si substrate far away from the interface with PCBM is assumed as 0 eV position. The position of the silicon valence band throughout the depletion layer, relative to  $E_F$ , is:

$$E_V(x, V_{bias}) = -|q| V_1(x, V_{bias}) - E_{FV} = -\frac{q^2 N_A}{\epsilon_0 \epsilon_{Si}} \frac{1}{2} (x + w_{Si}(V_{bias}))^2 - E_{FV} \quad (4.21)$$

where the negative sign reflects the fact that the bands are bent downwards. Similarly the position of PCBM-LUMO level throughout the PCBM layer, relative to  $E_F$ , is calculated from the electrical potential  $V_2$  (Eq. 4.6) in the PCBM layer at given  $x$  and  $V$  according to:

$$E_{LUMO}(x, V_{bias}) = -|q| V_2(x, V_{bias}) + E_0 \quad (4.22)$$

The integration constant  $E_0$  is determined assuming that the Fermi energy of the PCBM is pinned to the Al Fermi level [76] and the externally applied bias determines the difference between the quasi-Fermi energy of both contacts  $E_F^{Si} - E_F^{PCBM} = -V_{bias}$  (where negative  $V_{bias}$  is defined in reverse bias direction). Thus,  $E_{LUMO}(d, V_{bias}) = |q| V_{bias}$ , where we have used that  $E_F^{Si} = 0$  for  $x < -w_{Si}$ . With this boundary condition we obtain:

$$E_{LUMO}(d, V_{bias}) = |q| V = -|q| V_2(d, V_{bias}) + E_0 \quad (4.23)$$

hence

$$E_0 = |q| V_{bias} + |q| V_2(d, V_{bias}) \quad (4.24)$$

Finally:

$$E_{LUMO}(x, V_{bias}) = -|q| V_2(x, V_{bias}) + |q| V_2(d, V_{bias}) + |q| V_{bias} \quad (4.25)$$

For the barrier height  $\Phi_B$ , defined as the difference between the position of valence band in Si at the interface and the position of PCBM LUMO at the interface, we get:

$$\Phi_B = E_{LUMO}(0, V_{bias}) - E_V(0, V_{bias}) = |q| \left[ \frac{|q| N_A w_{Si}}{\epsilon_0 \epsilon_{C60}} d + V_{bias} + \frac{|q| N_A}{2\epsilon_0 \epsilon_{Si}} (w_{Si})^2 + \frac{E_{FV}}{|q|} \right] \quad (4.26)$$

using Eq. 4.8 we get:

$$\begin{aligned} \Phi_B &= |q| \left[ |V_{bi}| - V_{bias} + V_{bias} + \frac{E_{FV}}{|q|} \right] \\ &= |q| V_{bi} + E_{FV} \end{aligned} \quad (4.27)$$

Thus in the presented model the barrier height is independent of the external voltage. Finally the average value of barrier height obtained from  $1/C^2$  plot  $\Phi_{B(C-V)} = 0.63 \pm 0.05 \text{ eV}$  (see Table 4.1).

Fig. 4.10 and Fig. 4.11 show the band alignment and components of built-in potential obtained from C-V analysis for short circuit condition and reverse bias respectively.

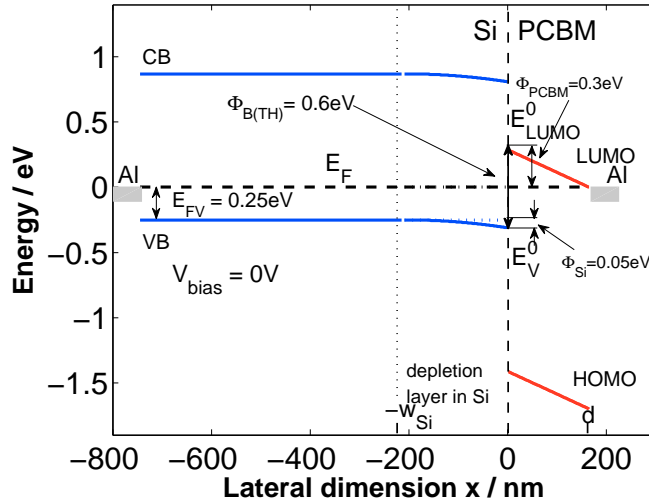


Figure 4.10: Band alignment at p-Si/PCBM interface. All values, except the Si wafer real thickness on the left side, are shown in scale and were calculated using the appropriate equations presented above.

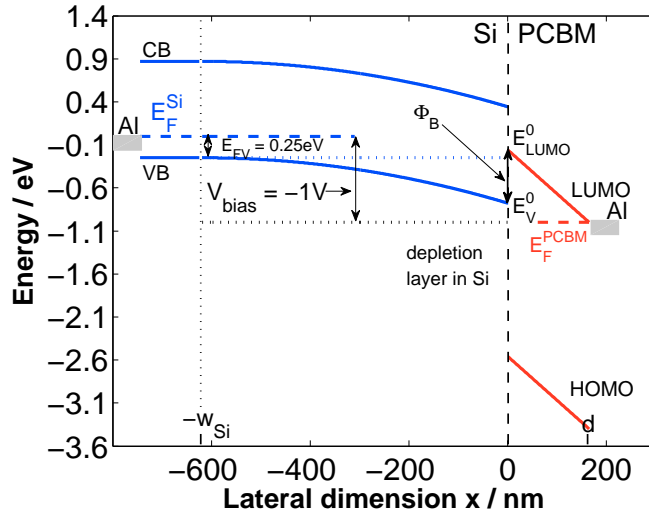


Figure 4.11: Band alignment at p-Si/PCBM interface. All values, except the Si wafer real thickness on the left side, are shown in scale and were calculated using the appropriate equations presented above. The exact dependence of quasi-Fermi levels close to interface is not known.

#### 4.2.1.2 J-V characteristics. Theoretical model for the diode operation

To analyze the J-V characteristics we have to look at the schematic picture of band alignment at the interface, presented in Fig. 4.10 and Fig. 4.11. The relative position of those levels implies the character of the current flow through the device. Under forward bias condition i.e. a positive bias voltage applied to the Al/p-Si back contact, electrons are efficiently injected from the Al top-contact into the PCBM layer. However, due to the barrier between the PCBM LUMO level and the Si conduction band (CB) the further electron injection from the PCBM LUMO into the Si conduction band is energetically unfavorable and the current has to traverse the organic-inorganic interface as a recombination current between electrons in the PCBM and holes in the p-Si.

On the other hand under reverse bias condition i.e. the negative voltage applied to the Al/p-Si back contact, holes are extracted from the p-Si valence band (VB) into the Al back-contact. However, no efficient direct injection of holes into the p-Si from the PCBM-HOMO is possible due the very low intrinsic PCBM hole concentration and the injection barrier for holes from the Al top-contact into the PCBM-HOMO. Thus, in the absence of radiation, only thermally excited carriers can maintain the dark current expected under reverse bias. We assume that in the ideal case the reverse dark current would result from direct thermal excitation of electrons (generation) from the p-Si valence band VB into the PCBM-LUMO. To describe the balance between those two competing processes of recombination and generation that defines the net current flowing through the device we will apply the theory of trap assisted recombination of charge carriers given by Shockley and Read [88], where we assume that the LUMO level of PCBM can be treated as a trap level of energy  $E_{LUMO}$ , capable of capturing and emitting holes (recombination and generation respectively).

The considered processes are governed by Fermi-Dirac statistics, thus the distribution functions are defined as:

$f_e(E)$  - the distribution function for electrons i.e. the probability that a state with energy  $E$  is occupied by electrons (empty of holes):

$$f_e(E) = \frac{1}{1 + \exp\left(\frac{E-E_F}{k_B T}\right)} \quad (4.28)$$

$f_h(E)$  - the distribution function for holes i.e. the probability that a state with energy  $E$  is occupied by hole (empty of electrons)

$$f_h(E) = 1 - f_e(E) = 1 - \frac{1}{1 + \exp\left(\frac{E-E_F}{k_B T}\right)} = \frac{1}{1 + \exp\left(\frac{E_F-E}{k_B T}\right)} \quad (4.29)$$

$f_{LUMO}(E_{LUMO}^{x=0})$  - probability that the trap i.e. LUMO state at the interface is occupied by electrons, which in thermal equilibrium is given by:

$$f_{LUMO}(E_{LUMO}^{x=0}) = \frac{1}{1 + \exp\left(\frac{E_{LUMO}^{x=0}-F}{k_B T}\right)} \quad (4.30)$$

$1 - f_{LUMO}(E_{LUMO}^{x=0})$  - probability that the LUMO state is empty of electron:

$$1 - f_{LUMO}(E_{LUMO}^{x=0}) = f_{LUMO}(E_{LUMO}^{x=0}) \exp\left(\frac{E_{LUMO}^{x=0} - F}{k_B T}\right) \quad (4.31)$$

In the above equations  $E_F$  stands for Fermi level, however in the further calculation for a biased junction quasi-Fermi levels will be used to describe the carrier distribution in Si and PCBM separately.

The hole emission rate  $dv_{he}$  from the LUMO level into the Si valence band is proportional to the concentration of empty LUMO states and to the probability that states in the VB in the range  $dE$  are occupied with electrons:

$$dv_{he} = e_p(E) \cdot (1 - f_{LUMO}(E_{LUMO}^{x=0}, E_F^{PCBM})) N_{LUMO} \cdot f(E, E_F^{Si}) N(E) dE \quad (4.32)$$

where  $N_{LUMO}$  is the total number of states at LUMO level per  $\text{cm}^3$ ,  $N(E)$  is the density of states in the Si VB and  $e_p(E)$  is the average probability, per unit time that a hole in the range  $dE$  be emitted by an empty LUMO state,  $E_F^{PCBM}$  and  $E_F^{Si}$  denote the quasi-Fermi levels on both sides of the interface associated with top Al/PCBM contact and with bottom Al/Si contact respectively. At short circuit conditions those levels are equal, however, as shown in Fig. 4.11, under an external bias they split by the value equal to the external bias. Similarly the hole capture rate  $dv_{hc}$  is proportional to the concentration of occupied LUMO states and to the probability that states in the VB in the range  $dE$  are empty (occupied by holes):

$$dv_{hc} = c_p(E) \cdot f_{LUMO}(E_{LUMO}^{x=0}, E_F^{PCBM}) N_{LUMO} \cdot (1 - f_e(E, E_F^{Si})) N(E) dE \quad (4.33)$$

where  $c_p$  is the average probability per unit time that a hole in the range  $dE$  be captured by an occupied LUMO state.

The net rate of hole recombination (capture - emission):

$$dU_{cp} = dv_{hc} - dv_{he}$$



$$\begin{aligned}
&= \left[ f_{LUMO}(1 - f_e(E)) - (1 - f_{LUMO})f_e(E) \frac{e_p(E)}{c_p(E)} \right] N_{LUMO}c_p(E)N(E)dE \\
&= \left[ 1 - \frac{(1 - f_{LUMO})}{f_{LUMO}} \frac{f_e(E)}{(1 - f_e(E))} \frac{e_p(E)}{c_p(E)} \right] f_{LUMO}N_{LUMO}c_p(E)(1 - f_e(E))N(E)dE
\end{aligned} \tag{4.34}$$

where the appropriate parameter values of the distribution functions i.e. the value of energy of LUMO states at the interface  $E_{LUMO}^{x=0}$  and a suitable quasi-Fermi levels have been omitted for the sake of clarity. If the system is in equilibrium the net hole recombination rate is zero, the relation  $E_F^{PCBM} = E_F^{Si}$  holds (which is not the case otherwise), and the value in square brackets in Eq. 4.34 must be zero, leading to:

$$\begin{aligned}
\frac{e_p(E)}{c_p(E)} &= \frac{f_{LUMO}(1 - f_e(E))}{(1 - f_{LUMO})f_e(E)} = \frac{f_{LUMO}}{f_{LUMO} \exp\left(\frac{E_{LUMO}^{x=0} - E_F^{PCBM}}{k_B T}\right)} \frac{f_e(E) \exp\left(\frac{E - E_F^{Si}}{k_B T}\right)}{f_e(E)} \\
&= \exp\left(\frac{E - E_F^{Si} - E_{LUMO}^{x=0} + E_F^{PCBM}}{k_B T}\right) = \exp\left(\frac{E - E_{LUMO}^{x=0}}{k_B T}\right)
\end{aligned} \tag{4.35}$$

Substituting Eq. 4.35 into Eq. 4.34 yields:

$$\begin{aligned}
dU_{cp} &= \left[ 1 - \exp\left(\frac{E_{LUMO}^{x=0} - E_F^{PCBM}}{k_B T}\right) \exp\left(\frac{-(E - E_F^{Si})}{k_B T}\right) \exp\left(\frac{E - E_{LUMO}^{x=0}}{k_B T}\right) \right] \\
&\quad \times f_{LUMO}N_{LUMO}c_p(E)(1 - f_e(E))N(E)dE
\end{aligned} \tag{4.36}$$

$$= \left[ 1 - \exp\left(\frac{E_F^{Si} - E_F^{PCBM}}{k_B T}\right) \right] f_{LUMO}N_{LUMO}c_p(E)(1 - f_e(E))N(E)dE \tag{4.37}$$

Integrating over all possible hole energies gives the total hole recombination rate:

$$U_{cp} = \left[ 1 - \exp\left(\frac{E_F^{Si} - E_F^{PCBM}}{k_B T}\right) \right] f_{LUMO}N_{LUMO} \int_{E_v}^{-\infty} c_p(E)(1 - f_e(E))N(E)dE \tag{4.38}$$

We point out here that in the described case we are dealing with a non-degenerate semiconductor since, as was shown above,  $E_F^{Si} - E_V = 0.25 \text{ eV} > 3k_B T$ . Thus a Maxwell-Boltzmann distribution can be assumed for the holes distribution function in Si:

$$(1 - f_e(E)) \cong \exp\left(\frac{E - E_F^{Si}}{k_B T}\right) \tag{4.39}$$

Substituting expression Eq. 4.39 and rewriting Eq. 4.38 gives:

$$\begin{aligned}
U_{cp} &= \left[ 1 - \exp\left(\frac{E_F^{Si} - E_F^{PCBM}}{k_B T}\right) \right] f_{LUMO}N_{LUMO} \\
&\quad \times \int_{E_v^{x=0}}^{-\infty} c_p(E) \exp\left(\frac{E - E_V^{x=0} + E_V^{x=0} - E_F^{Si}}{k_B T}\right) N(E)dE \\
&= \left[ 1 - \exp\left(\frac{E_F^{Si} - E_F^{PCBM}}{k_B T}\right) \right] f_{LUMO}N_{LUMO} \cdot N_V \exp\left(\frac{E_V^{x=0} - E_F^{Si}}{k_B T}\right)
\end{aligned} \tag{4.40}$$

$$\int_{E_V^{x=0}}^{-\infty} c_p(E) \exp\left(\frac{E-E_V^{x=0}}{k_B T}\right) N(E) dE$$

$$\times \frac{1}{N_V} \quad (4.41)$$

where  $N_V$  is the effective density of states in the valence band,  $E_V^{x=0}$  is the VB energy. Introducing  $p$  = total amount of holes in valence band

$$p = N_V \exp\left(\frac{E_V^{x=0} - E_F^{Si}}{k_B T}\right) \quad (4.42)$$

and  $\langle c_p \rangle$  = the average probability over states in valence band, per unit time that a hole in the range  $dE$  be captured by an occupied LUMO state:

$$\langle c_p \rangle = \frac{\int_{E_V^{x=0}}^{\infty} c_p(E) \exp\left(\frac{E-E_V^{x=0}}{k_B T}\right) N(E) dE}{N_V} \quad (4.43)$$

where  $C_p$  = the probability per unit time that a hole will be captured if the LUMO states are fill with electrons so that they are in a condition to capture holes.

$$C_p = N_{LUMO} \langle c_p \rangle \quad (4.44)$$

the expression for  $U_{cp}$  becomes:

$$U_{cp} = \left[ 1 - \exp\left(\frac{E_F^{Si} - E_F^{PCBM}}{k_B T}\right) \right] f_{LUMO} C_p$$

$$= [p f_{LUMO} - N_V \exp\left(\frac{E_V^{x=0} - E_F^{Si}}{k_B T}\right) \exp\left(\frac{E_F^{Si} - E_F^{PCBM}}{k_B T}\right)]$$

$$\times \exp\left(\frac{E_F^{PCBM} - E_{LUMO}^{x=0}}{k_B T}\right) (1 - f_{LUMO}) C_p \quad (4.45)$$

where

$$f_{LUMO} = 1 - f_{LUMO} \exp\left(\frac{E_F^{PCBM} - E_{LUMO}^{x=0}}{k_B T}\right) \quad (4.46)$$

was substituted.

Thus finally:

$$U_{cp} = \left[ p f_{LUMO} - N_V \exp\left(\frac{E_V^{x=0} - E_{LUMO}^{x=0}}{k_B T}\right) (1 - f_{LUMO}) \right] C_p \quad (4.47)$$

results. By introducing  $p_1$  as the number of holes in the Si valence band for the case in which the Fermi level falls at  $E_{LUMO}^{x=0}$ :

$$p_1 = N_V \exp\left(\frac{E_V^{x=0} - E_{LUMO}^{x=0}}{k_B T}\right) = N_V \exp\left(\frac{-\Phi_B}{k_B T}\right), \quad (4.48)$$

finally we obtain for the total net recombination rate:

$$U_{cp} \propto [p f_{LUMO} - p_1 (1 - f_{LUMO})] \quad (4.49)$$

The interface generation-recombination (G-R) current density flowing through the device ( $J_d$ ), is proportional to  $U_{cp}$ , allowing us to model the current density-voltage characteristics. Depending on the value of external bias  $V_{bias}$ , either

recombination ( $p \cdot f_{LUMO}$ ) or generation ( $p_1 \cdot (1 - f_{LUMO})$ ) current density is dominating and the sign of the net current density changes. Fig. 4.12 shows the voltage dependence of distribution functions  $f_{LUMO}$  and  $(1 - f_{LUMO})$ , which is the probability that the LUMO state is occupied by electron or empty, respectively. For evaluating  $f_{LUMO}$ , the difference  $E_{LUMO}^{x=0} - E_F^{PCBM}$  as a function of the external bias was calculated using Eq. 4.23 and assuming that the quasi-Fermi level in PCBM  $E_F^{PCBM}$  is constant throughout the complete PCBM layer at the level of  $+ |q| V_{bias}$ . As we can see under reverse bias the LUMO state is empty, reaching 50% probability of occupation at  $V = 0.35$  eV i.e. at the flat band condition for which  $w_{Si} = 0$ . Similarly for evaluating the total amount of holes  $p$  the value of  $E_V^{x=0}$  as a function of external bias is calculated from Eq. 4.21 and assuming that the quasi-Fermi level in Si  $E_F^{Si}$  is zero throughout the whole Si substrate.

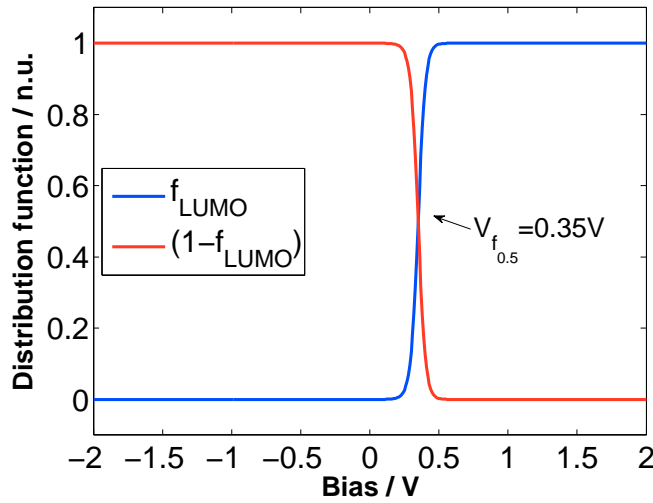


Figure 4.12: The external bias dependence of distribution functions for electron in LUMO state  $f_{LUMO}$  and for hole in LUMO state  $(1 - f_{LUMO})$

Basing on Eq. 4.49, the  $J_d$  can be expressed as:

$$J_d = J_0 [p f_{LUMO} - p_1 (1 - f_{LUMO})] \quad (4.50)$$

Since the relevant energy levels,  $E_V^{x=0}$  and  $E_{LUMO}^{x=0}$ , required for evaluating Eq. 4.50 are obtained from our C-V experiments through the solution of Poisson's equation given in Eq. 4.21 for  $E_V^{x=0}$  and in Eq. 4.23 for  $E_{LUMO}^{x=0}$  and the difference between  $E_F^{Si} - E_F^{PCBM} = |q| V_{bias}$  is given by the external voltage,  $J_0$  is the only free parameter available for scaling the ideal generation-recombination current to the experimental data.

For forward bias voltage higher than  $V_{bi}$  additional charging at the interface occurs due to injection, resulting in an enhancement of the capacitance of organic layer. The total charge density is:

$$p(V) = p_{bi} + \Delta p(V) \quad (4.51)$$

where  $p_{bi}$  is the value of  $p$  at  $V = V_{bi}$  and  $\Delta p(V)$  is voltage dependent additional charge density. Knowing the capacitance of organic layer  $C_{PCBM} = \epsilon_{C60} \epsilon_0 / d$

and the voltage drop over organic layer for forward bias direction  $V - V_{bi}$  we can calculate the surface charge density. In order to calculate the bias dependent accumulated charge density per volume  $\Delta p(V)$  we use the characteristic length  $L$  corresponding to Debye screening length, which describes the distance over which a small unbalanced charge decays [5]:

$$L_D = \sqrt{\frac{\epsilon_{Si}\epsilon_0 k_B T}{q^2 N_A}} \quad (4.52)$$

Finally the expression for additional charge density is:

$$\Delta p(V) = \frac{C_{PCBM}(V - V_{bi})}{|q| L_D} \quad (4.53)$$

For  $J_0 = 1 \cdot 10^{-17}$  A/cm<sup>2</sup> the ideal generation-recombination current density as calculated from Eq. 4.50 (including the total charge concentration expressed in Eq. 4.51 for forward bias higher than  $V_{bi}$ ) is shown by the green line in Fig. 4.13. In order to account for the non-ideal properties of the junction, a series resistance  $R_s$  accounting for all contact resistances is included in our simulations. The total current density across the device in the forward direction can be calculated by:

$$J_T(V) = J_d(V_d) \quad (4.54)$$

where  $V$  is the external voltage,  $J_d(V_d)$  is the ideal G-R diode current density as a function of the voltage drop  $V_d$  across the rectifying interface as calculated from Eq. 4.50.

The total external voltage is expressed as:

$$V = J_d(V_d)R_s + V_d \quad (4.55)$$

The corrected theoretical curve is compared with measurement points (red line in Fig. 4.13) assuming  $R_s = 33 \Omega \text{cm}^2$  (for given electrode area  $14 \text{cm}^2$  the value of  $R_s$  is corresponding to  $236 \Omega$ ). With this parameter we obtain a reasonable agreement between experiment and simulation in forward direction.

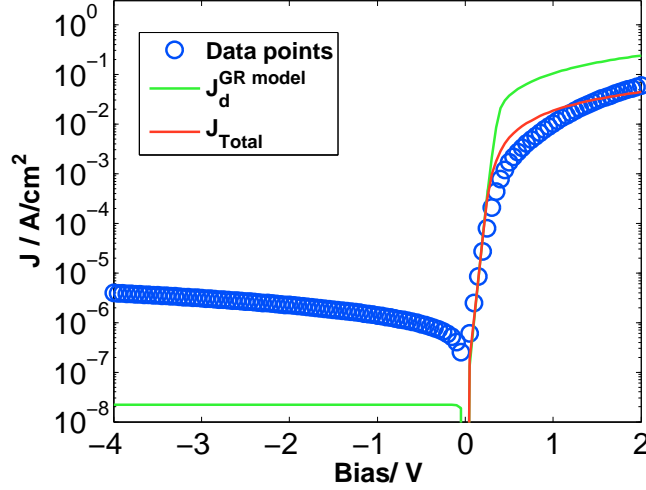


Figure 4.13: J-V characteristics of Al/p-Si/PCBM/Al structure. The results of the modeling using the ideal interface generation-recombination model at 300 K (Eq. 4.50) are shown by the green line. Including parasitic series resistance, the red line results as fit to the experimental J-V curve in forward direction.

For reverse bias we conclude from Fig. 4.13 that the measured J-V characteristics is dominated by a charge transport via a parallel channel, since a 100 times larger reverse current density is measured than expected from the ideal interface G-R current model (Eq. 4.50).

The trivial explanations for this parallel channel are ohmic shunts  $R_p$  due to pin-holes in the PCBM layer through that the Al directly contacts the p-Si layer and defects in the Al-PCBM contact via that holes are injected into the HOMO of PCBM. While such technological defects are definitely present in some of our samples, their dominance in the presented data can be virtually ruled out, since from any batch of processed samples only those with the largest rectification, i.e. with the largest  $R_p$  were chosen for further characterization. These samples show reproducible J-V characteristics, making uncontrolled technical defects as reason for a shunt extremely unlikely. In addition the voltage dependence of the measured current density deviates from the linear one expected for an ohmic shunt, as shown by the green line in Fig. 4.17. Moreover, the observed activation of the reverse current with temperature, which will be discussed below, can not be understood based on this trivial model.

For investigating the conduction mechanism via this channel, which is believed to be intrinsic to the device structure, the dependence of the reverse current on the temperature was determined. Although the ideal reverse current density described by Eq. 4.50 is also temperature dependent any observed dependence of the reverse current density on temperature is due to transport via the parallel channel, since in the temperature range from 250 K to 300 K the ideal interface G-R current density at -1.1 V is two orders of magnitude lower than the measured value at the same temperature (see Fig. 4.14).

The J-V vs T measurements were done for a set of samples fabricated in different processes. The samples were mounted in the cryostat, cooled to liquid nitrogen temperature and left for self heating, or optionally heated to 340 K and

left for self cooling with heating/cooling rate lower than 0.01 K/s, what provided a thermal equilibrium. Typically a constant reverse bias (-1.1 V) was applied and the current and temperature have been automatically recorded every 1 s via the LabView controlled computer. The results of two measurements are presented in Fig. 4.14 and Fig. 4.15 in a form of an Arrhenius plot. The experimentally measured current density follows the equation:

$$J = A \cdot \exp\left(\frac{-E_a}{k_B T}\right) \quad (4.56)$$

$$\ln(J) = \ln(A) + \left(\frac{-E_a}{k_B T}\right) \quad (4.57)$$

where  $A$  is the proportionality constant. The slope of the linear fit yields the activation energy  $E_a$ . Table 4.2 summarized the values obtained for all measured samples with average value of the thermal activation energy of dark reverse current equal to  $0.54 \pm 0.02$  eV.

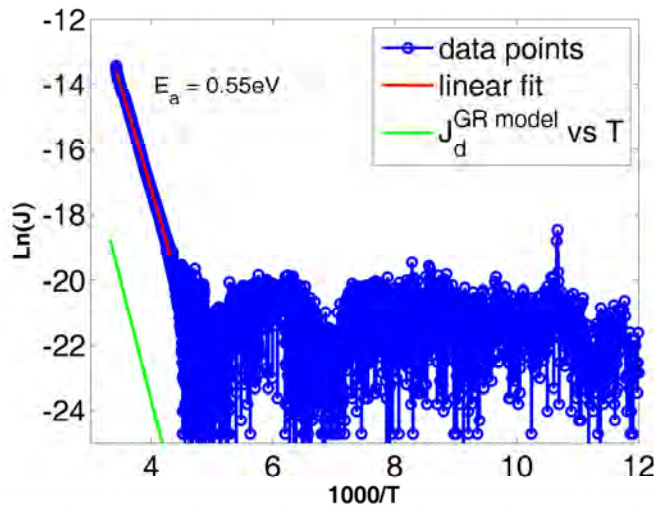


Figure 4.14: Arrhenius plot of dark current at reverse bias -1.1 V, sample Nr 1. The green line shows the theoretical temperature dependence of ideal interface G-R current density as calculated from Eq. 4.50.

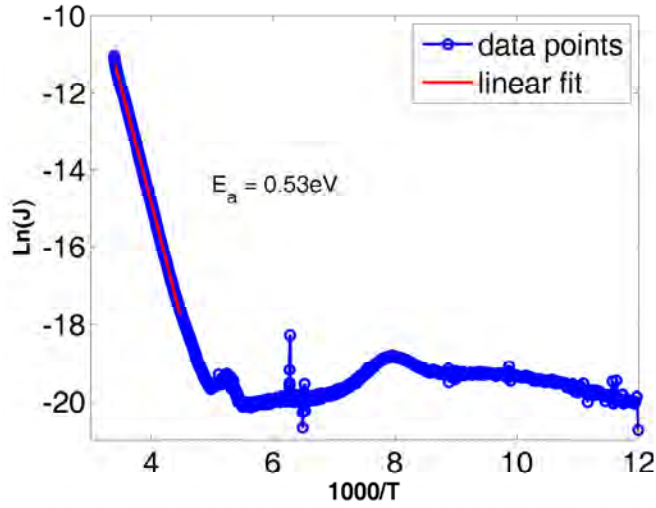


Figure 4.15: Arrhenius plot of dark current at reverse bias -1.1 V, sample Nr 2

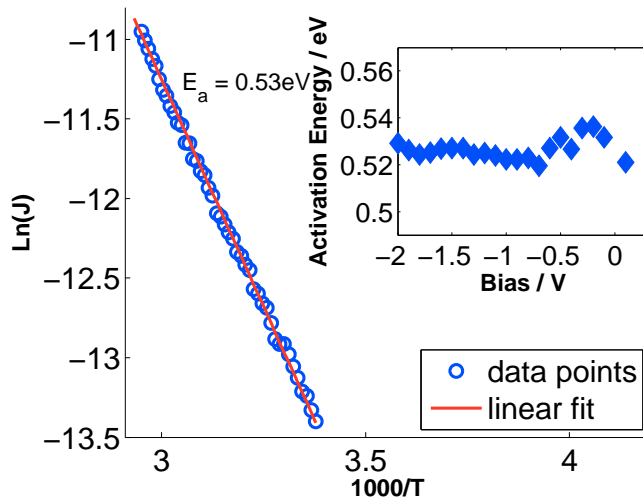


Figure 4.16: Arrhenius plot of dark current at reverse bias -1.1 V, sample Nr 3. Inset: bias dependence of activation energy

Table 4.2: Activation energy values extracted from four different samples measured at -1.1 V

Sample	$E_a$ / eV
Nr 1	0.55
Nr 2	0.53
Nr 3	0.53
Nr 4	0.55
<b>AVG</b>	<b>0.54</b>

To study the bias dependence of the activation energy the J-V sweep has been recorded every 1 K during self cooling of the sample from 340 K to room

temperature with rate of cooling lower than 0.01 K/s. The inset of Fig. 4.16 shows that the value of activation energy is virtually independent of the external bias, ranging from 0.52 eV to 0.54 eV at -0.25 V. It is therefore reasonable to assume the uncertainty of activation energy measurement on the order of 0.02 V.

We want to point out that due to the dominance of the parallel transport channel, the activation energy can not be attributed to the height of the p-Si/PCBM interface barrier defined directly as difference between the interface position of Si VB and LUMO of PCBM.

A possible explanation of the origin of observed thermally activated parallel channel might be the generation-recombination mechanism in the depletion region in p-Si substrate. It is well known that in Si p-n junctions the net generation-recombination current, which is thermally excited over the Si bandgap throughout the depletion zone, is dominating the reverse current by several orders of magnitude as compared to the saturation diffusion current [5, 89, 90]. The same mechanism has been suggested for organic-inorganic diodes on n-GaAs substrate [42] and p-Si substrate [41].

According to Ref. [5], the generation current depends on the width of the depletion zone  $w_{Si}$  and the intrinsic carrier density  $n_i = 1.45 \cdot 10^{10} \text{ cm}^{-3}$  at 300 K of the substrate semiconductor. For large enough reverse biases for which  $p < n_i$  in the dominant part of the depletion region in a p-type Si, the space charge region generation current density can be approximated by:

$$J_{gen}^{rev} = |q| n_i w_{Si} / \tau_e \quad (4.58)$$

where  $\tau_e$  is the effective lifetime of the thermally generated minority carriers in the substrate semiconductor.

Due to the proportionality of  $J_{gen}^{rev}$  to  $n_i$ , its thermal activation depends exponentially on  $E_g/2k_B T$ , where  $E_g$  is the bandgap of the substrate semiconductor. The experimentally obtained activation energy ( $0.54 \pm 0.02 \text{ eV}$ ) is in excellent agreement with the value that one would expect based on the bandgap of the Si substrate. Using  $\tau_e \approx 0.1 \mu\text{s}$  as typical value for Si [89], the black line in Fig. 4.17 is calculated for  $J_{gen}^{rev}$  using Eq. 4.58. Fig. 4.17 shows that the space charge region generation current density as calculated according to Eq. 4.58 is in good agreement with the measured reverse current density. Therefore, we conclude that the heterojunction diode current in reverse direction is dominated by the space charge region generation current, which exceeds the interface generation current calculated using Eq. 4.54 by the same amount as observed in the experiment.

Since  $w_{Si}$  is proportional to the square root of the external voltage, the same dependence is expected for the space charge region generation current. The deviation from the square root dependence of  $J_{gen}^{rev}$  shown in Fig. 4.17 for  $V > -2 \text{ V}$  remains unclear up to now. Tunneling of the electrons through triangular barrier (Fowler-Nordheim tunneling [56]) can be ruled out, since this process results in an exponential increase of the current, dominating the J-V above a certain threshold voltage.



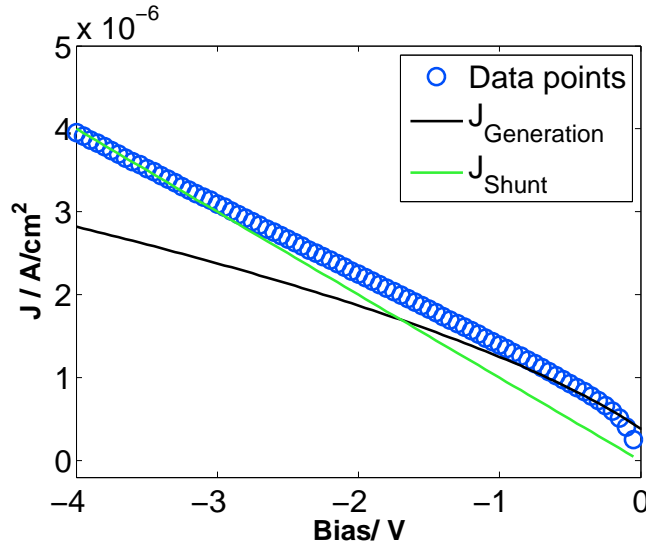


Figure 4.17: J-V characteristics of Al/p-Si/PCBM/Al structure in reverse bias direction. The results of modeling using space charge region generation is shown by the black line, additionally a pure ohmic shunt current characterized by parallel resistance value  $R_P = 1 \text{ M}\Omega\text{cm}^2$  is shown for comparison by green line.

The other explanation of the parallel conduction mechanism could be the presence of deep trap states in PCBM located at  $\simeq 0.55 \text{ eV}$  below LUMO level, facilitating a hopping transport, with possible thermal activation of electrons into the delocalized LUMO band. The difference in the energetic positions of LUMO and trap level would correspond to the measured activation energy. Based on such a model, the trap energy level providing the small hopping mobility would show up in the band diagram shown in Fig. 4.10  $0.53 \pm 0.02 \text{ eV}$  below the PCBM LUMO level, i.e. lined up at the interface with the Si VB energy level ( $0.6 \pm 0.05 \text{ eV}$  below PCBM LUMO) within experimental uncertainties. In this model a direct injection of electrons from the silicon valence band into the localized sub-bandgap states of PCBM and a subsequent transport via localized states to the Al contact might represent the parallel conduction channel characterized by  $R_p$ , dominating the current in the reverse direction. From Fig. 4.17 a parallel resistance  $R_P = 1 \text{ M}\Omega\text{cm}^2$  can be estimated. As upper concentration limit for electrons injected into the trap level  $n_{lim} = 8 \cdot 10^{13} \text{ cm}^{-3}$  is estimated. A larger injected electron concentration would result in a band bending of  $\sim 10 \text{ meV}$ , which would be observable in the C-V measurement as reported in Section 4.2.1.1. From these estimated values, a minimum mobility of  $\mu_t^{PCBM} = 1 \cdot 10^{-6} \text{ cm}^2/\text{Vs}$  for the transport via the trap states is required. This required mobility appears to be unlikely large for the assumed deep traps  $\simeq 0.55 \text{ eV}$  below the PCBM LUMO, and would imply an unusual high density of states at a very narrow level which was not reported in literature [91].

In addition, the observed deviation from the linear J-V characteristics, which would be a consequence of this interpretation, can not be explained in this model.

From the currently available data set, most likely the space charge region generation current is the reason for the large observed reverse current. However, for ruling out the mechanism discussed in the previous paragraph, further studies

would be required.

## 4.2.2 Photoresponse - spectrally resolved photocurrent

Fig. 4.18 and Fig. 4.20 show a J-V characteristics of studied Al/p-Si/PCBM/Al devices measured at room temperature and 77 K respectively, under the broadband illumination of a NIR tungsten lamp of FTIR spectrometer, spectrally restricted by a band-pass filter (cut-off above 0.95 eV and below 0.44 eV). The light intensity was measured with calibrated InGaAs detector as described in Chapter 3.2, where the integral limits were chosen as indicated in Fig. 3.5, resulting in the value of  $3.4 \text{ mW/cm}^2$ . At room temperature, the dark J-V characteristic and the J-V under IR illumination are almost identical. However, a high resolution J-V scan around zero bias, shown in Fig. 4.19 verifies that also at room temperature a  $V_{OC}$  of 1 mV and a short circuit current of  $7.2 \text{ nA/cm}^2$  is measured. At 77 K a typical photo-voltaic behaviour is seen, a short circuit current ( $J_{SC}$ ) of  $52 \text{ nA/cm}^2$  and an open circuit voltage  $V_{OC}$  of 0.46 V is measured (Fig. 4.20). The linear plot presented in Fig. 4.21 reveals that for forward bias higher than  $V_{OC}$  a slightly higher current is observed under illumination, reaching the relative increase of 8% as compared to dark current. A possible origin this observed photoconductivity will be given later.

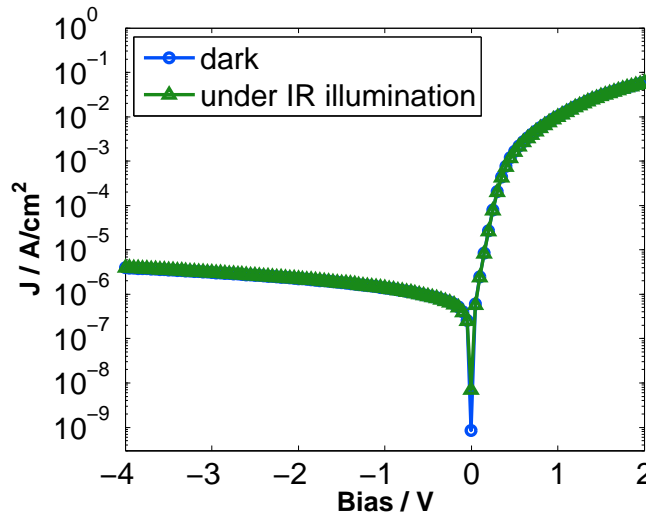


Figure 4.18: The comparison of J-V characteristics measured at 300 K in dark and under illumination with a tungsten lamp of a FTIR spectrometer spectrally restricted by a 0.95 eV band-pass filter. Light intensity was  $3.4 \text{ mW/cm}^2$

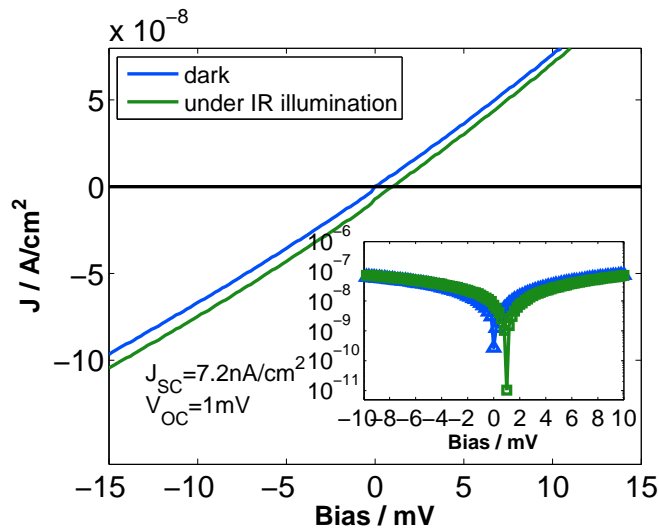


Figure 4.19: The comparison of J-V characteristics measured with high resolution around 0 V, at 300 K in dark and under illumination with a tungsten lamp spectrally restricted with 0.95 eV band-pass filter. Inset: semi-logarithmic plot.

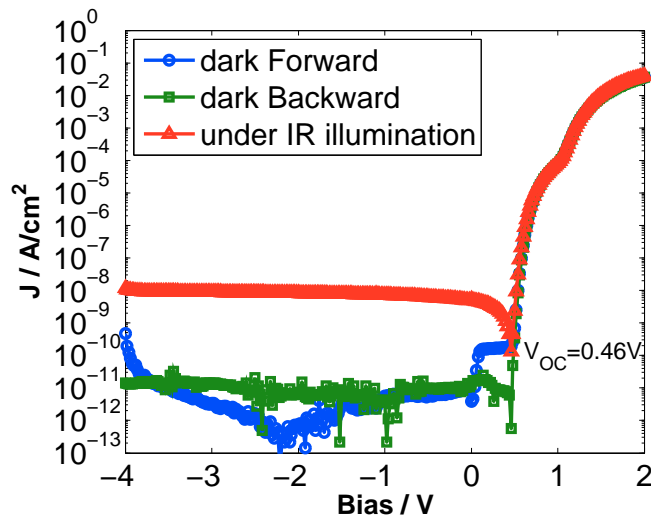


Figure 4.20: The comparison of J-V characteristics measured at 77 K in dark and under illumination of a tungsten lamp of FTIR spectrometer restricted with 0.95 eV band-pass filter. Light intensity was  $3.4 \text{ mW/cm}^2$

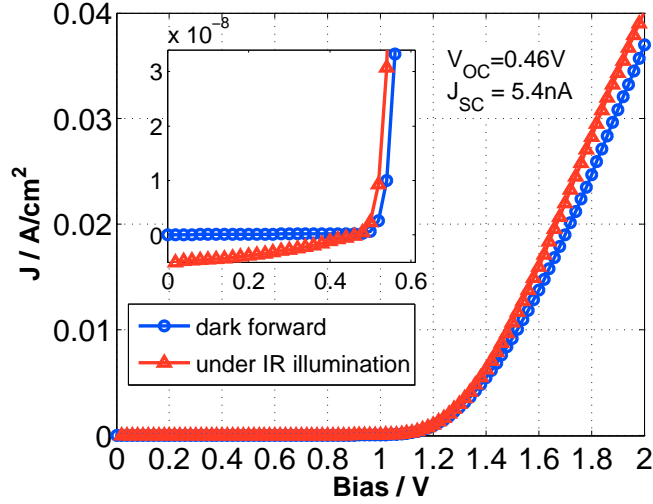


Figure 4.21: The comparison of J-V characteristics presented in linear plot and at forward bias, measured at 77 K in dark and under illumination of a tungsten lamp of FTIR spectrometer restricted with 0.95 eV band-pass filter. Inset: plot for low voltages.

The photocurrent (PC) has been spectrally resolved using a FTIR setup described in Section 3.2.2. Due to relatively low short circuit current (in the range of few nA under full illumination of FTIR NIR tungsten lamp spectrally restricted with Si filter and a 0.95 eV band-pass filter) and corresponding low AC signal reaching the electronics of the spectrometer, the fast scan measurement could not have been applied in any case of p-Si/PCBM samples. Instead the step-scan measurement has been applied with a chopper frequency of 69 Hz. The modulation frequency is far below the roll-off frequency that for PCBM devices has been roughly estimated from the time resolved response to be in kHz range, however, the photodiode response time was probably limited by the electronic setup that was applied in the case of p-Si/PCBM samples. Depending on the signal level, different, integration times have been used, varying from 30 ms to 3 s. Usual spectral resolution was  $32 \text{ cm}^{-1}$ .

To understand the mechanism governing the light absorption and charge excitation it is important to estimate the onset of the infrared response. Typically in case of well studied phenomena such as internal photoemission in metal-semiconductor junctions a physical model is assumed leading to the spectral dependence of the photoemission quantum yield in a form [92]:

$$Y = A(h\nu - \Phi)^p \quad (4.59)$$

where  $\Phi$  is the barrier height at the interface,  $h\nu$  the photon energy, and  $A$  a constant. The value of power exponent  $p$  given by different authors varies depending on the system parameters but is usually close to 2 for electronic transitions between metal and semiconductors with three-dimensional electron and hole density of states. Hence most often the linearized form of spectral curves is used a so called Fowler plot in  $Y^{1/2}$  vs  $h\nu$  co-ordinates, based on the pioneer paper by Fowler from 1931 [93]. The value of the barrier height is then estimated from the intersection of the linear fit extrapolation with x-axis.

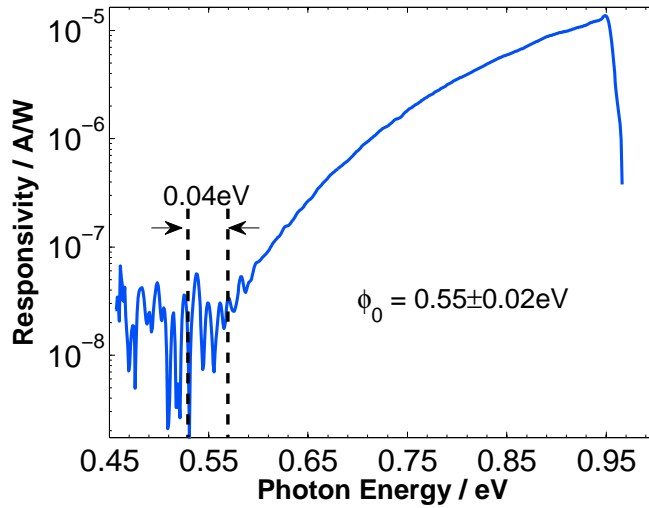


Figure 4.22: Example of photocurrent spectra measured at 77K showing the method of estimation of onset energy value and uncertainty.

The uncertainty of the estimation depends strongly on the power exponent  $p$  of Eq. 4.59 which requires a correct detailed model of the internal photoemission process for a given interface. In case of the studied p-Si/PCBM interface a detailed valid model is not known and accurate linear fit can not be found. It is therefore reasonable to estimate the onset of the photocurrent from the semi-logarithmic plot, assuming that the onset corresponds to the photon energies at which the noise of the signal ceases, see Fig. 4.22 for an example. The uncertainty of the estimation (marked on figure with dashed lines) is assumed to be  $\pm 0.03$  eV at 300 K ( $kT = 26$  meV at 300 K) and  $\pm 0.02$  eV at 77 K ( $kT = 7$  meV at 77 K but in the case of the above analysis it is reasonable to assume higher uncertainty) (Fig. 4.22). The method of the analysis of photocurrent onset described above will be used for all measurements presented in this work.

In the following subsections, the results of the photo current measurements at different temperature will be shown with general remarks concerning the spectral shape obtained for various temperatures, followed by a discussion of the photocurrent generation mechanism. In order to further validate the presented model, the influence of the external bias, the material used as top metal electrode and the chemical structure of the PCBM derivative will be shown.

#### 4.2.2.1 Temperature dependence of PC

Fig. 4.23 shows the temperature dependence of the spectrally resolved photocurrent measured behind a silicon filter (photon energies lower than Si bandgap of 1.12 eV). Since the transmission edge of Si is not a step function [5], (shown in Fig. 4.23 by the black dashed line), substantial amount of light with photon energies close to the Si absorption edge reaches the sample despite the 5 mm thick filter. As a result, at room temperature the dominating contribution to the measured photocurrent is the peak close to 1.1 eV (see Inset of Fig. 4.23), which is assigned to band to band absorption in the p-Si substrate of the device. As the temperature decreases, the bandgap of silicon expands [5] shifting the absorption edge of the p-Si substrate of the device above the absorption edge of the Si filter

that is kept at room temperature. Hence the main peak at 1.1 eV abates and finally nearly disappears at 77 K. The observed remaining signal below 1.1 eV is monotonically increasing from its onset energy (close to 0.55 eV) to the Si filter cutoff.

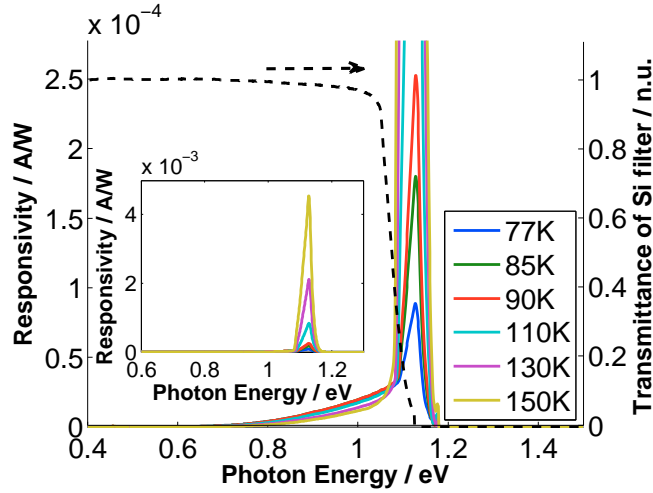


Figure 4.23: Temperature dependence of responsivity spectra of Al/p-Si/PCBM/Al heterojunction, measured behind Si filter. Inset: Full y-scale plot of the responsivity spectra.

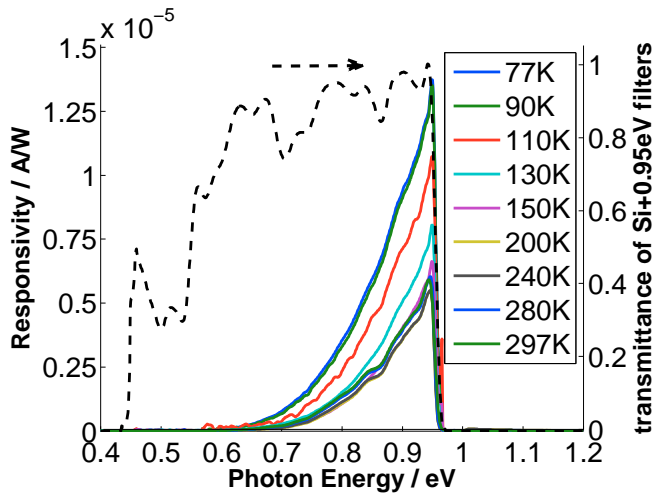


Figure 4.24: Temperature dependence of responsivity spectra of Al/p-Si/PCBM/Al heterojunction, measured behind a 0.95 eV band-pass filter.

In order to examine the infrared part of the measured spectra a band-pass filter with cutoff energy at 0.95 eV is used. The filter is mounted together with the Si filter, since the band-pass filter transmittance is not 0% for the whole spectral range above 0.95 eV and the light with  $\hbar\omega > 0.95$  eV coming through the filter has to be cut off by the Si filter to avoid the PC signal from absorption in p-Si substrate. Fig. 4.24 shows that the shape of the spectral dependence of PC does not change with the temperature and the responsivity at 300 K drops to 40% of the value at 77K for 0.8eV ( $1.55 \mu\text{m}$ )(see Fig. 4.25).

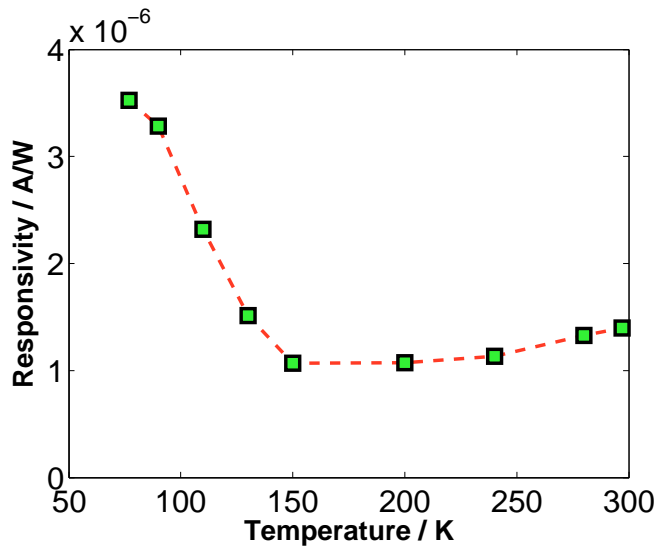


Figure 4.25: Temperature dependence of responsivity at photon energy 0.8 eV (1.55  $\mu\text{m}$ ).

As stated in the beginning of this section, the onset of photocurrent can be estimated from the semi-log plot (Fig. 4.26). For clarity only, few temperatures are shown in the plot. The onset is independent of temperature and is consistently estimated to be  $0.55 \pm 0.02$  eV.

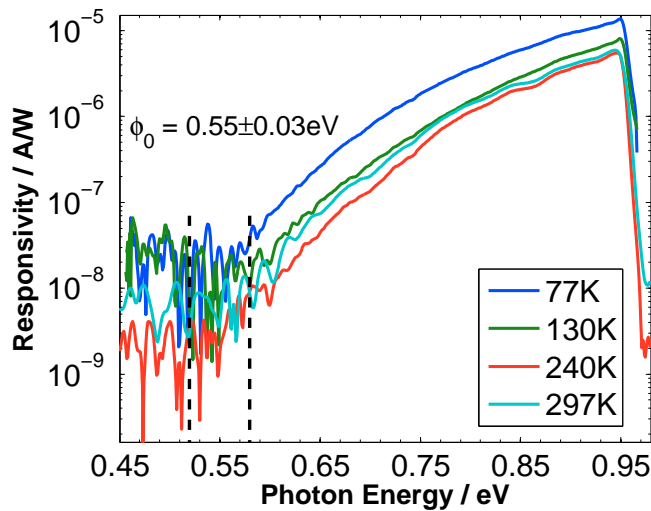


Figure 4.26: Semi-log plot, temperature dependence of responsivity spectra of Al/p-Si/PCBM/Al heterojunction, measured behind 0.95 eV band-pass filter. The uncertainty of the onset estimation is shown by the dashed vertical lines.

In order to get a better insight into the low energy part of the spectra and to eliminate the possibility of any secondary electron photoexcitation, that might be possible in case of broad spectrum illumination in FTIR method, measurements using a germanium filter with cut-off energy of around 0.7 eV have been done. In case of PCBM samples the value of the photocurrent behind the germanium

filter did not exceed 0.1 nA. Therefore, step-scan measurement with long integration time had to be done in order to get a satisfactory results. Nevertheless the achieved signal-to-noise-ratio (SNR) was just 18 for room temperature measurement with 3 s integration time and only 12 for 77 K measurement where 1 s integration time was used, because it was not possible to maintain the constant temperature for 12 h required for 3 s integration time measurement.

Fig. 4.27 and Fig. 4.28 show the comparison of PC spectra behind germanium and 0.95 eV filter for 300 K and 77 K respectively. Since the shape of the spectra is the same for both filters used, the important conclusion is that the complex photoexcitation of secondary species can be excluded. Due to very low PC and SNR it is even more difficult to estimate the onset energy from semi-logarithmic plot, especially for the 77 K experiment. Nevertheless, Fig. 4.27 gives  $\Phi_0 = 0.51 \pm 0.03$  eV for 300 K and Fig. 4.28  $\Phi_0 = 0.55 \pm 0.02$  eV, consistent with the results presented above. The onset energy is considered as temperature independent at least within the assumed uncertainty level. Due to the extremely low photocurrent level and low SNR no better estimation was achieved.

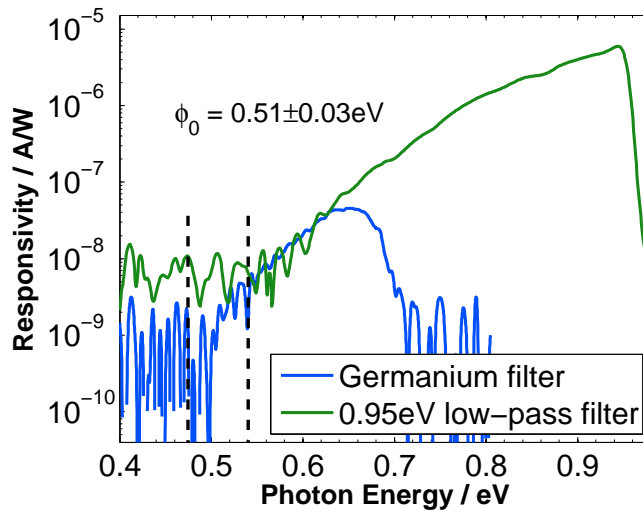


Figure 4.27: Semi-logarithmic plot, responsivity spectra of Al/p-Si/PCBM/Al heterojunction, measured at 300 K behind germanium filter and 0.95 eV band-pass filter. The uncertainty of the onset estimation is shown.



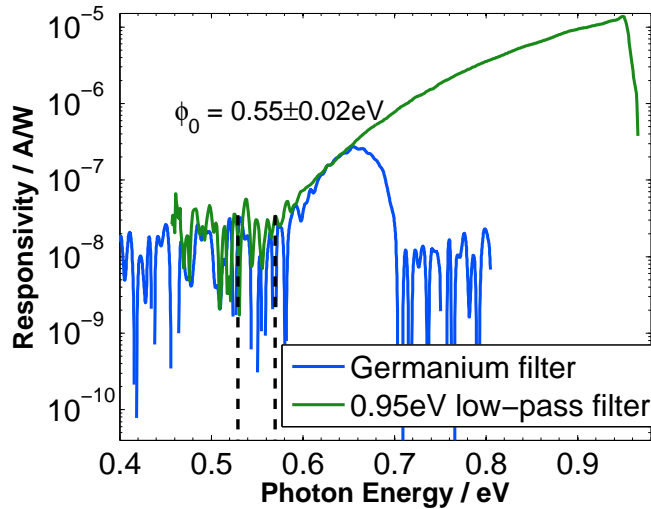


Figure 4.28: Semi-logarithmic plot, responsivity spectra of Al/p-Si/PCBM/Al heterojunction, measured at 77 K behind germanium filter and 0.95 eV band-pass filter. The uncertainty of the onset estimation is shown.

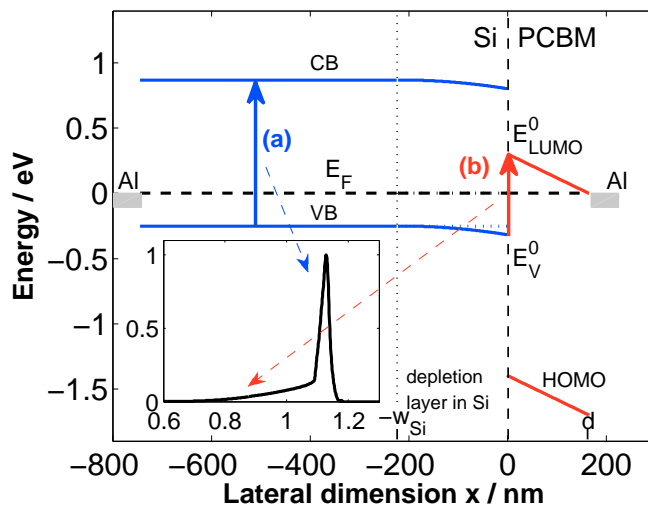


Figure 4.29: Scheme of the two processes responsible for photocurrent generation.

Two separate processes have to be considered in order to analyze the observed photocurrent spectra. They are schematically denoted as process (a) and (b) in Fig. 4.29. The process (a) i.e. the peak at 1.12 eV is assigned to the absorption in Si substrate and is explained as the photoexcitation of electron from the valence band into the conduction band with subsequent interface crossing, electron injection into the LUMO of PCBM and extraction via the top electrode. Simultaneously the hole generated in the Si VB is extracted via the bottom electrode, resulting in a short circuit photocurrent that is measured in the external circuit. The validation of this explanation has been shown in temperature dependence of photocurrent spectra, where the 1.12 eV peak abates upon shifting of the absorption edge of the p-Si substrate energetically above the absorption

edge of the Si filter by cooling. On the other hand process (b), giving rise to the IR tail measured behind the 0.95 eV filter remains independent of temperature. Due to the transparency in the near infrared range of both heterojunction materials (see Fig. 4.23 for silicon and Fig. 4.4 for PCBM), process (b) can not be trivially assigned to absorption in either of them. The sub-bandgap photocurrent is assigned to the generation of an electron-hole pair and separation due to the built-in field at the interface, featuring a photoexcitation of electrons from the Si VB at the interface into the LUMO of PCBM. In that sense it should be understood as an enhancement of the hole capture rate of the PCBM LUMO level, i.e. as an enhancement of the thermal excitation of electrons over the interface under reverse bias and short circuit condition, as described in details in Section 4.2 for absent illumination. The estimated onset energy of photocurrent  $\Phi_0 = 0.55 \pm 0.02$  eV corresponds, within the experimental uncertainties, to the difference between valence band position and the PCBM LUMO energy at the interface  $\phi_0 = E_V^{x=0} - E_{LUMO}^{x=0}$  i.e. to the barrier height estimated in C-V experiment ( $\Phi_{B(C-V)} = 0.6 \pm 0.05$  eV).

With respect to the space charge region generation model for the reverse current, the contribution of an analogous generation mechanism to the photocurrent for photon energies in the range of  $1.1 \text{ eV} \geq \hbar\omega \geq 0.55 \text{ eV}$  can be ruled out by the fact that such an effect is not observed for classic Si p-n junctions where the reverse current is known to be dominated by space-charge region carriers generation [5]. Moreover the observed voltage dependence of photoresponse does not follow the square root dependence expected for space-charge region generation. It also does not follow the observed voltage dependence of the dark current shown in Fig. 4.17, which is, as discussed in Section 4.2.1.2, most likely dominated by space-charge region carrier generation.

Instead, Fig. 4.33 shows that the photocurrent is proportional to  $V^{1/p}$ , where  $\frac{2}{7} < p < \frac{2}{5}$  is obtained, depending on photon energy.

Other possible explanation of the photoresponse mechanism might be a process of an optical excitation of near-interface bandgap states in the PCBM, which has been described in the book by Afanas'ev on Internal Photoemission(IPE) Spectroscopy [92] and referred to as a pseudo-IPE process (see Fig. 4.30). The localized interface states in the PCBM gap are being re-filled by the electrons tunneling from the Si VB across the interface providing a steady photocurrent. The excited states, resulting from the photoexcitation of electrons from the sub-bandgap localized states, are characterized by relatively long lifetimes due to the fact that their relaxation mechanism is limited to low-efficient interactions with phonons only. Typically for IPE process the excited electrons in metals or narrow-bandgap semiconductors exhibit an inelastic electron-electron scattering before they reach the interface. In case of pseudo-IPE process the energy of excited electrons is lower than the bandgap of the material in which the photoexcitation occurs, as a result the relaxation by inelastic electron-electron scattering is not present. Due to relatively long lifetimes of the excited states, the quantum yield of the pseudo-IPE may be large, even if the density of contributing initial sub-bandgap states is low. The spectral dependencies of the quantum yield of the pseudo-IPE are expected to be determined by the energy distribution of the gap states involved in the photoexcitation.

This mechanism has been assumed to explain the photocurrent excitation in the GaAs Schottky contacts modified by a molecular interlayer [94, 95]. A

characteristic mark of the pseudo-IPE process is the lack of dependence of PC spectra on the Density-of-States (DOS) of emitter and its Fermi level, in our case on the p-doping concentration of the silicon substrate. Such an approach was used to identify the photon-stimulated tunneling (PST) current in Si/SiO<sub>2</sub> structures [96], the effect of photoemission itself allowed to analyze the defect states in the oxide layer. Thus a systematic proof of the independence of the photocurrent onset on  $N_A$  should allow to clarify whether or not the pseudo-IPE process occurs in our devices.

The presence of localized sub-bandgap state i.e. a polaron(anion)  $C_{60}^-$  was predicted theoretically [97, 98] and reported experimentally [99], see Chapter 5 for details. Moreover it was also seen in the photoconductivity of  $C_{60}$  OFET presented in this work. The transistor contains no Si/fullerene interface, yields however a photoresponse, which can be attributed to anion absorption with onset energy virtually equal to the PC onset of the diode investigated here (see Fig. 5.15). Additionally the same onset is seen in the photo induced absorption (PIA) experiment done on  $C_{60}$ /CuPC blend where the excitation of an anion state is clearly visible (see Fig. 5.13).

Thus, in such a model, the observed photoresponse would be a photoconductive one (for  $V_{bias} \neq 0$ ), what could explain the slight increase of forward bias current under illumination shown in Fig. 4.21.

However, it has to be pointed out that based on the obtained results of photocurrent spectra for short circuit conditions and reverse bias, we are not able to distinguish between the two proposed models namely the interface photoexcitation from Si VB directly into LUMO of PCBM or a process with an intermediate step featuring a photoexcitation of localized state in organic layer and tunneling of holes into the Si (pseudo-IPE). Similarly, the interface generation-recombination of charge carriers without illumination, which ideally should be responsible for the reverse current density (but is obscured by a parallel process) and is believed to be enhanced by photon absorption under illumination, can not be distinguished as two-states process or a process with and intermediate step. In the model for interface generation-recombination without illumination, presented in Section 4.2.1.2, the potential role of an intermediate step should be reflected in the corresponding probabilities of hole capture  $c_p$  and emission  $e_p$ , without resulting in changes to the described formalism.

The question arises, if a potentially present localized state involved in PC generation is an interface state or a bulk one with possibility to facilitate the hopping transport, discussed in Section 4.2.1.2 as an alternative transport model under the reverse bias. Based on the available data, a final conclusion with respect to the carrier excitation path (direct excitation across the interface or via an intermediate localized state) can not be made at this stage.

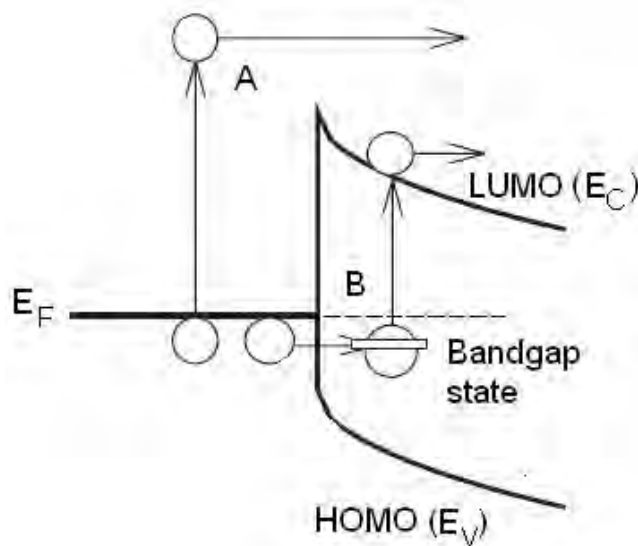


Figure 4.30: Graphical representation of Internal Photoemission process (A) and pseudo-IPE process (B), featuring photoexcitation of electron from near-interface defect level filled by electron tunneling from conducting electrode. Figure taken from [92].

#### 4.2.2.2 Bias dependence of PC

The influence of the applied external bias has been measured at 100 K to provide the insight to possible changes of both IR part and the Si peak of the PC spectrum. Fig. 4.31 shows that no obvious changes of the spectral shape are induced by applying either negative or positive bias. Generally an increase of responsivity with increasing reverse bias is observed and a decrease with increasing positive bias. Finally at +0.5 V, when the injection starts, the PC signal disappears. A detailed spectral analysis of photocurrent at higher forward bias, corresponding to photoconductivity seen in Fig. 4.21 was not performed.

The rates of the bias induced changes are different for different photon energies in the IR part and for Si peak (see Fig. 4.32). The PC associated with band to band transition in Si increases at -4 V only 1.3 times respective to its value at 0 V, whereas a two fold increase is observed for PC at 0.8 eV. The bias dependence varies also for different energies in the IR tail. Fig. 4.33 reveals a dependence  $PC \propto V^{2/5}$  for 0.6 eV and  $PC \propto V^{2/7}$  for 0.8 eV.

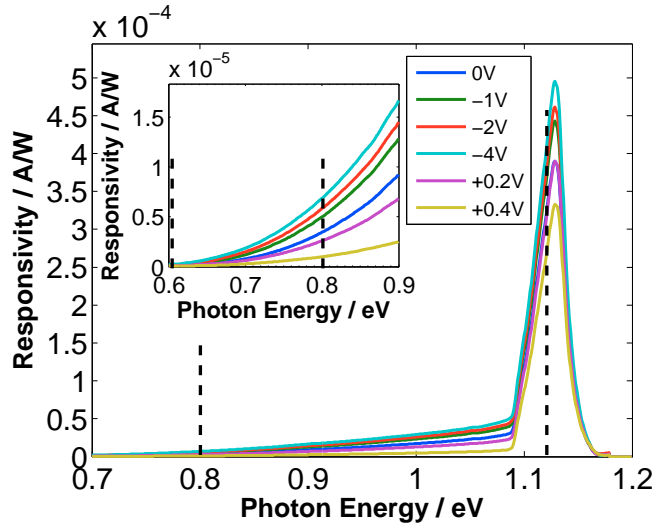


Figure 4.31: Bias dependence of responsivity spectra of Al/p-Si/PCBM/Al heterojunction, measured behind Si band-pass filter at temperature 100 K. The guide lines at 0.6 eV, 0.8 eV and 1.12 eV mark the energies at which the PC vs bias is shown in Fig. 4.32 Inset: lower energies view.

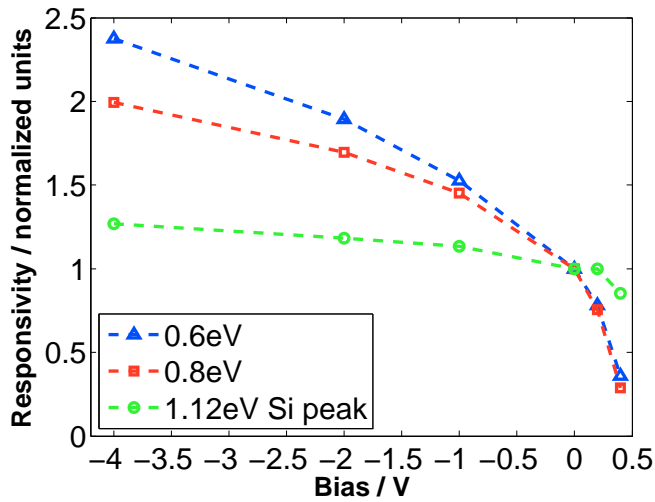


Figure 4.32: Relative responsivity vs bias. The values for each energies (0.6 eV, 0.8 eV and 1.12 eV) are normalized to the value at 0 V of each energy. Measured at temperature 100 K.

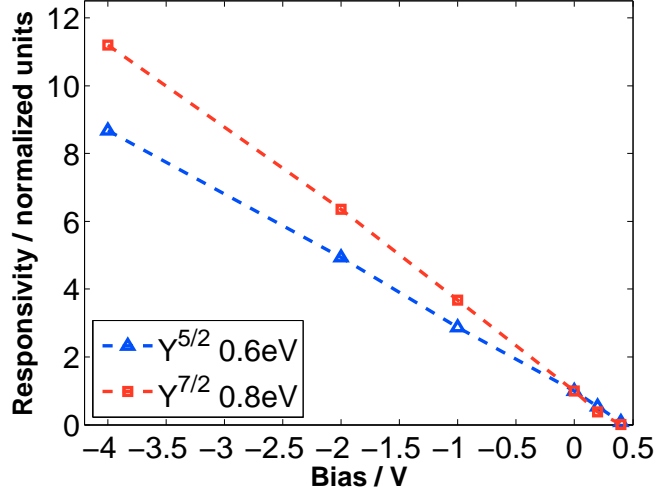


Figure 4.33: Relative responsivity vs bias for 0.6 eV, 0.8 eV plotted with a corresponding power resulting in linear dependence.

Important to notice is also the fact that the onset of the photocurrent (Fig. 4.34) remains the same for all bias voltages investigated, at least within the resolution of onset estimation. This finding is in agreement with the main result that the onset energy for the photo excitation is given by the difference between the position of  $E_{LUMO}$  and  $E_V$ , which is independent of external bias.

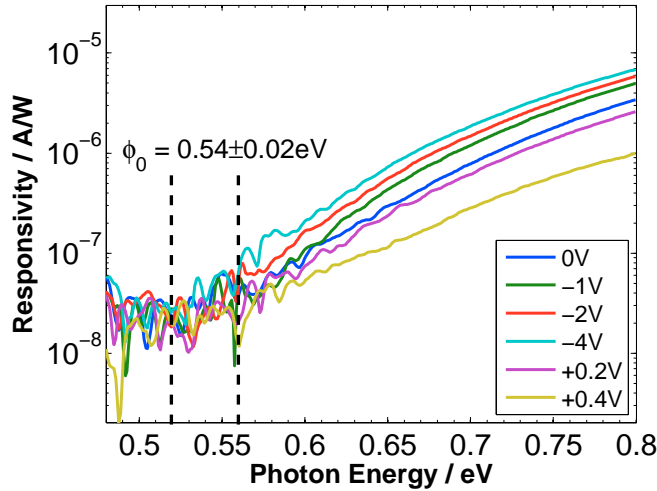


Figure 4.34: Semi-log plot, Bias dependence of responsivity spectra of Al/p-Si/PCBM/Al heterojunction measured at 100 K. The uncertainty of the onset estimation is shown.

#### 4.2.2.3 Top Metal electrode dependence of PC

In order to further validate the presented model for sub-bandgap absorption different metals have been used as the top electrode. The ohmic Al contact has been replaced with Au that is known to form a non-ohmic electron contact to

PCBM [78]. Both devices were fabricated on the same silicon 15·15 mm<sup>2</sup> substrate in order to provide identical fabrication conditions, the only difference was the final metal evaporation step.

Additionally a sample with both Al and Ag contacts have been studied. Silver is known to form an ohmic contact with PCBM and is widely used in bulk-heterojunction solar cells [78]. The J-V characteristics shown in Fig. 4.35 confirms that the difference between Al and Ag electrode is marginal, whereas the PCBM/Au device exhibits a much lower rectification ratio and the total current might be influenced by combined effect of two diodes in series. The discussed characteristics as compared with the clearly ohmic room temperature J-V characteristics of the p-Si/metal (Al,Ag,Au) device shown in Fig. 4.53, Fig. 4.54 and Fig. 4.55 proves that the rectifying behaviour of the discussed hybrid device should be ascribed to the inorganic–organic interface.

The existence of a barrier at PCBM/Au electrode could lead to photocurrents in sub-bandgap energy range induced by internal photoemission at PCBM/metal interface [92]. Therefore, if the IR response was influenced by PCBM/metal contact, a change to non-ohmic contact could lead to enhancement of the PC and/or a change of the onset energy. The PC at 0.8 eV for the device with Au contact was in the same order as the one with Al contact (see Fig. 4.36), and the onset energy remained unchanged.

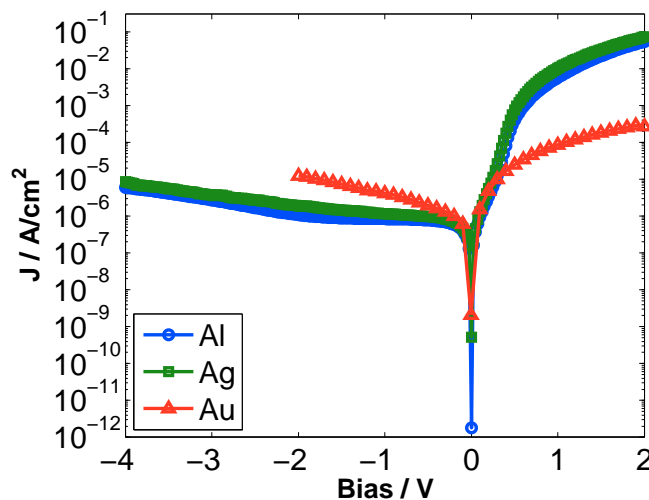


Figure 4.35: J-V characteristics of Al/p-Si/PCBM/metal devices with different metal used as top electrode, measured at 300 K.

Similarly the measurement of PCBM/Ag device proved that substitution of Al with Ag has no effect on the onset of energy of PC (see Fig. 4.37). The device with Ag exhibited a responsivity higher by factor 1.25, but such small changes might as well stem from different PCBM layer thicknesses of two different devices fabricated on a single p-Si substrate due to non-uniformity of organic layer thickness deposited by spin coating.

It can be concluded that the PCBM/metal contact is not influencing the onset and/or the shape of the IR response. Hence internal photoemission from metal to the PCBM is not present and photoexcitation process originates from p-Si/PCBM interface and/or bulk of PCBM.

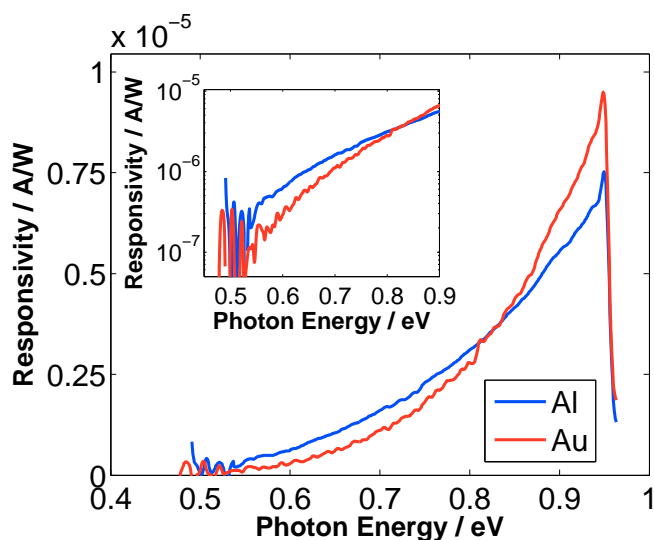


Figure 4.36: Top metal electrode dependence of responsivity spectra of Al/p-Si/PCBM/metal heterojunction at 77 K. Both devices were fabricated on the same substrate.

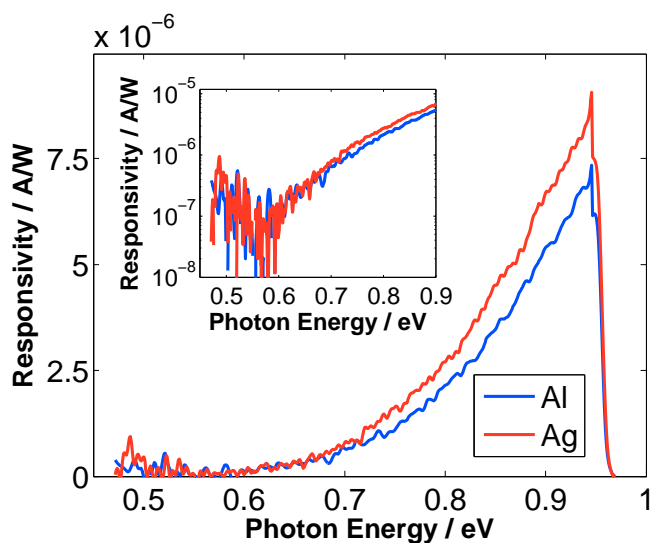


Figure 4.37: Top metal electrode dependence of responsivity spectra of Al/p-Si/bisPCBM/metal heterojunction at 77 K. Both devices were fabricated on the same substrate.

#### 4.2.2.4 PCBM derivative dependence of PC

Devices with different PCBM derivatives have been fabricated and measured in order to examine the possible influence of position of LUMO level measured for pristine material on the onset energy of the photocurrent. The used derivatives were reported in [83, 100, 101] to exhibit the following difference in position of LUMO levels as compared to [60]PCBM, regardless of actual reported absolute values, which are known to depend strongly on the electrochemical setup: [70]PCBM:  $\Delta = 0$  eV, bisPCBM:  $\Delta = +0.1$  eV, [84]PCBM:  $\Delta = -0.35$  eV.



Fig. 4.40 shows the normalized photocurrent spectra for all studied derivatives. The fact that shape of spectral dependence for [60]PCBM is slightly different and the onset is sharper than for the other derivatives can be ascribed to the fact that the presented spectral curves were normalized to the maximum value of each one. Thus, the curve of the sample with generally higher signal to noise ratio and better rectifying properties i.e. the [60]PCBM will exhibit the highest dynamical range. See Fig. 4.38 for the comparison of J-V curves for different derivatives.

Under the proposed assumption that the interface band alignment defines the onset energy and if the position of the LUMO level at the interface equals to the value in the bulk of pristine material one should expect a shift of the onset energy by +100 meV and -350 meV for the bisPCBM and [84]PCBM devices with respect to the onset of the [60]PCBM device, respectively. Such a shift is by far larger than the assumed uncertainty and would be easily recognized even for a measurement using a 0.95 eV band-pass filter with low signal to noise ratio in the onset range. In the case of bisPCBM a shift by around +40 meV is observed whereas for [84]PCBM no shift is present. The small difference in onset energy for bisPCBM and the invariance of the onset for [84]PCBM suggests that with respect to the presented model of photoexcitations of electrons from the valence band of Si to the LUMO of fullerene, the energetic position of the LUMO level at the interface is not related to the difference of LUMO levels measured for pristine PCBM derivatives, i.e. the difference does not follow the Schottky-Mott limit [80, 81]. Such an observation might be a hint that the photocurrent mechanism is governed by the excitation of electrons from deep trap states in PCBM into delocalized states with higher mobility. Such deep trap states could be interface states or PCBM bulk states. In the former case, the pseudo-IPE process as discussed in Section 4.2.2.1 would be an adequate model for the PC generation mechanism, in the latter case, the PC response would be photoconduction. The energetical position of such an assumed localized state would be required to be independent of the PCBM derivative. Such an independence of the trap energy from the PCBM modification might be the property of a polaron state of the fullerene cage, which is locally (i.e. on the scale of the diameter of the carbon rings) similar in all PCBM modifications. Experimentally, no data exist on the polaron energies for [60]PCBM, [70]PCBM, bisPCBM and [84]PCBM, only for C<sub>60</sub> a polaron state energy was theoretically calculated [97, 98] and observed [99] at  $\simeq 0.7$  eV below the C<sub>60</sub> LUMO level, see Chapter 5 for details.

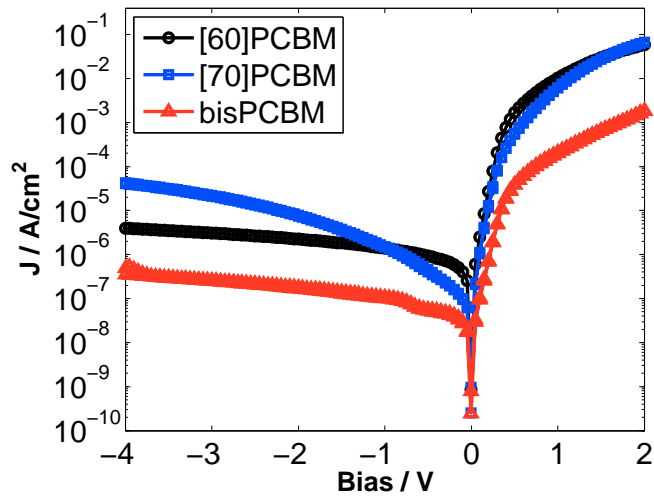


Figure 4.38: J-V characteristics of Al/p-Si/PCBM/Al devices with different fullerene derivative, measured at 300 K.

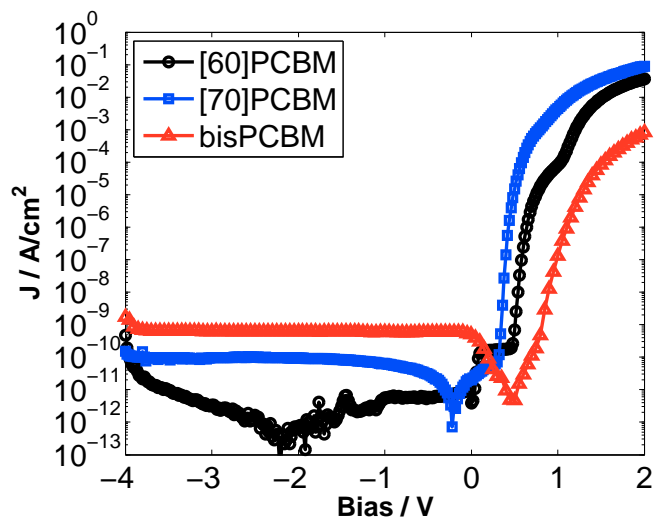


Figure 4.39: J-V characteristics of Al/p-Si/PCBM/Al devices with different fullerene derivative, measured at 77 K.

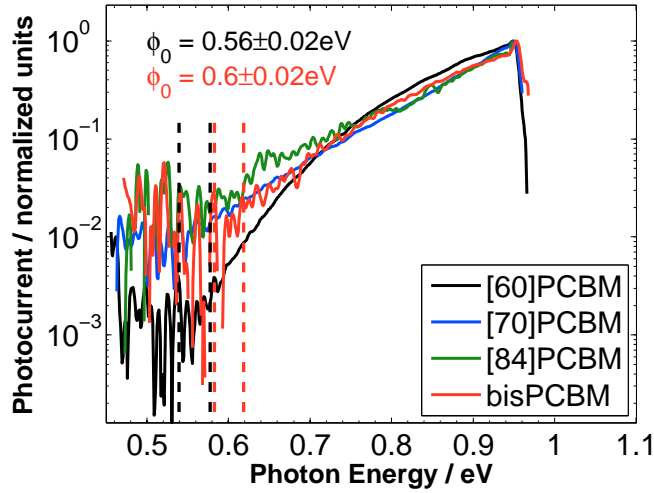


Figure 4.40: PCBM derivative dependence of photocurrent spectra of Al/p-Si/PCBM/Al heterojunction. Measured at 77 K. The uncertainty of measurement for [60]PCBM is shown.

### 4.2.3 Device improvement by adding LiF current enhancement layer to the top contact

In this section the influence of LiF/Al contact as top electrode and comparison of electrical properties and photoresponse of Al/p-Si/PCBM/Al and Al/p-Si/PCBM/LiF/Al will be presented.

It has been shown in literature that thermal deposition of Al on thin film of LiF evaporated on the organic semiconductor layer such as Alq<sub>3</sub> or C<sub>60</sub> induces the dissociation of LiF [102–105] and as a result dopes locally the organic material and enhances the electron injection into organic semiconductors, reducing the barrier height between organic material and metal electrode [104, 106–108]. The use of LiF/Al has become a standard in the fabrication of organic light emitting diodes (OLED).

In order to ensure the same fabrication condition, both Al/p-Si/PCBM/Al and Al/p-Si/PCBM/LiF/Al heterojunctions have been fabricated with the previously described procedure on one 15·15 mm<sup>2</sup> p-type Boron doped [100] silicon substrate. The top contact to fullerene has been fabricated by either single thermal evaporation of Al or evaporation of LiF(1-2 nm) followed by evaporation of Al. The electrodes area was 14 mm<sup>2</sup> for all devices.

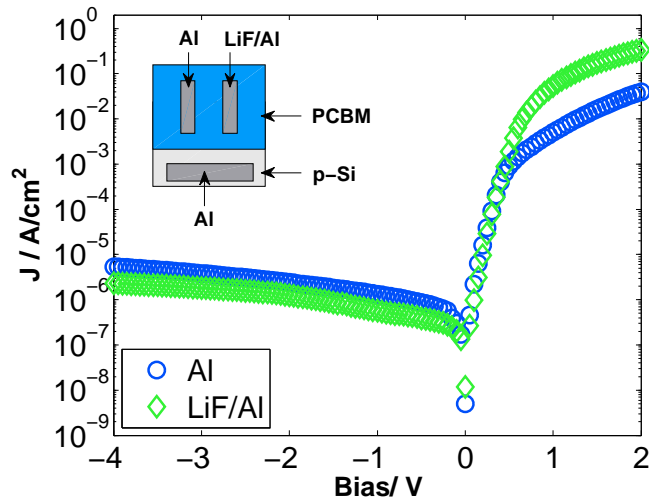


Figure 4.41: J-V characteristics of Al/p-Si/PCBM/electrode devices with two different top electrodes.

Fig. 4.41 shows the J-V characteristics of both investigated device structures at 300K. For a bias variation from -1 to +1 V current rectification ratio of  $1.7 \cdot 10^4$  and  $2.7 \cdot 10^5$  is observed for Al and LiF/Al top electrodes respectively. The higher forward bias current observed for LiF/Al electrode can be assigned to enhanced injection due to organic material/metal barrier lowering effect of LiF/Al [104, 106–108].

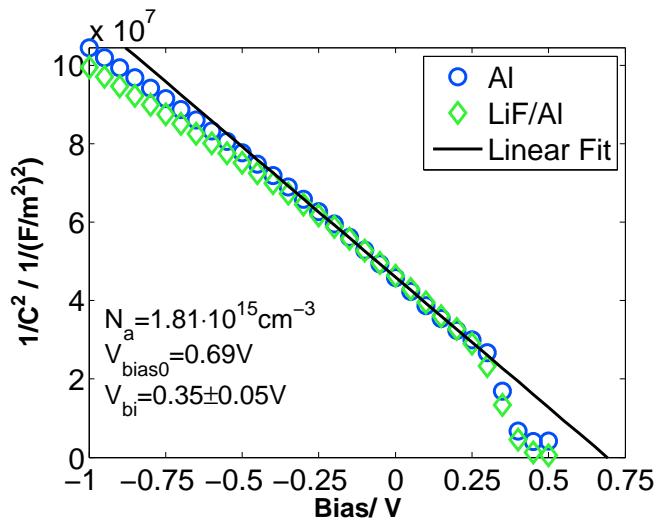


Figure 4.42:  $1/C^2$  vs V characteristics of Al/p-Si/PCBM/Al and Al/p-Si/PCBM/LiF/Al heterojunctions.

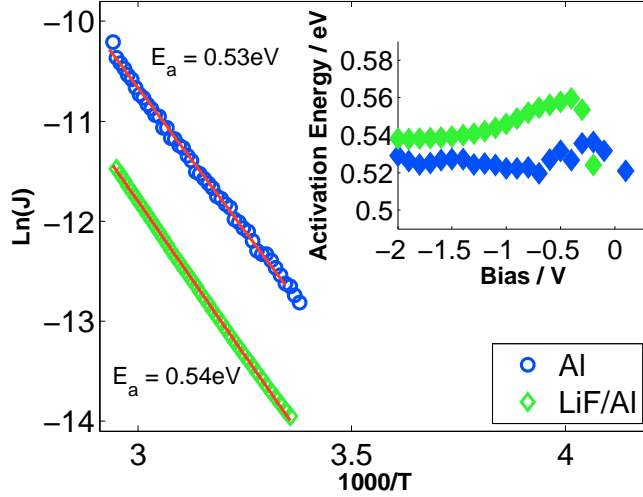


Figure 4.43: Arrhenius plot of dark current at reverse bias  $-1.5\text{ V}$  for two electrodes. Inset: Bias dependence of activation energy.

The result of C-V measurement presented in Fig. 4.42 reveals no difference between both electrodes suggesting that the assumption of absent localized charges in the PCBM layer is valid for LiF/Al device as well. This observation suggests that  $C_{60}^-$  anions that might diffuse into the PCBM layer upon LiF dissociation as described in [105] for a  $35\text{ nm}$  layer of  $C_{60}$ , either do not diffuse through a  $165\text{ nm}$  layer of PCBM or their concentration is too low to be seen in C-V measurement or their emission-time constant is too high as compared with used  $1\text{ kHz}$  frequency. Also, the observed barrier is independent of top electrode. The same analysis as in Section 4.2.1.1 yields for both electrodes the following parameters values:  $N_A = 1.81 \cdot 10^{15}\text{ cm}^{-3}$ ,  $V_{bi} = 0.35 \pm 0.06\text{ V}$  and  $\Phi_{B(C-V)} = 0.6 \pm 0.06\text{ eV}$ .

In order to investigate the possible influence of LiF/Al electrode on the reverse current addressed previously for Al electrode a thermal activation energy is estimated from the Arrhenius plot of dark current at reverse bias  $-1.5\text{ V}$  for both types of electrodes (Fig. 4.43). The J-V sweep has been recorded every  $1\text{ K}$  during self cooling of the sample from  $340\text{ K}$  to room temperature. At  $-1.5\text{ V}$  the activation energy  $E_a = 0.53\text{ eV}$  and  $0.54\text{ eV}$  is found for Al and LiF/Al top electrode respectively. The activation energy exhibits a slight voltage dependence (inset of Fig. 4.43). The virtually equal values of activation energy suggest that the same ambiguous mechanism described above is responsible for the reverse dark current in both studied devices.

No further conclusions on the nature of the reverse current generation-mechanism as discussed in Section 4.2.1.2 can be made based on the additional data for the devices with LiF/Al as top contact.

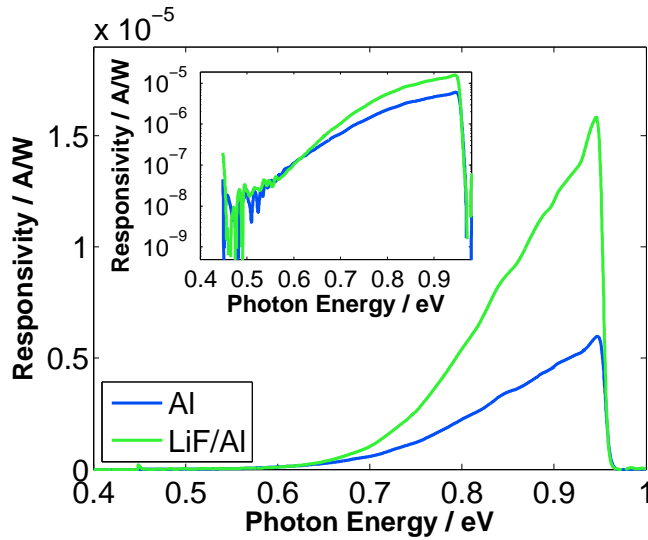


Figure 4.44: Responsivity spectra of Al/p-Si/PCBM/Al and Al/p-Si/PCBM/LiF/Al heterojunctions. Inset: semi-logarithmic scale plot.

The influence of LiF/Al electrode on photocurrent is shown in Fig. 4.44. As stated before the dissociation of LiF upon Al evaporation lowers the barrier height at PCBM/electrode interface which results in a 2.4 fold increase of PC value at 0.8 eV ( $1.55 \mu m$ ). Virtually equal onset energy  $\simeq 0.52$  eV (inset of Fig. 4.44) suggests that the photocurrent generation mechanism described in Section 4.2.2 remains independent of top electrode. Presented enhancement of forward bias current and photocurrent, as well as the invariance of the barrier height with respect to the top electrode seen in C-V characteristics and the invariance of thermal activation energy of dark reverse current prove the well established concept that the main role of lithium fluoride is the decrease of barrier height at the organic/metal interface.

### 4.3 p-Si/C<sub>60</sub> heterojunction photodiodes

In this section the current density-voltage characteristics and the spectrally resolved photocurrent of the Al/p-Si/C<sub>60</sub>/Al heterojunction diodes will be presented. The C<sub>60</sub> layers were deposited with the hot-wall-epitaxy technique described at the beginning, with the same substrate preparation and contact deposition method as p-Si/PCBM diodes. The HWE itself as a vacuum method provides much cleaner conditions than spin-casting in an inert atmosphere, and, thus, should result in less contaminated and better performing devices. Moreover, the C<sub>60</sub> exhibits a much higher electron mobility than its soluble derivative. Mobilities for the polycrystalline C<sub>60</sub> films in range of 1 cm<sup>2</sup>/Vs measured in Organic Field Effect Transistor (OFET) configuration were reported in [65, 67], whereas values for spin-casted PCBM films, reported in [75], were in the range of 0.05 – 0.2 cm<sup>2</sup>/Vs. However, it was found out that the deposition of C<sub>60</sub> in vacuum alone on a substrate cleaned in the same way as for PCBM devices does not provide a sufficient cleanness level and results in devices of inferior quality, exhibiting a much lower photocurrent than the PCBM samples and a rectification ratio on the order of only 10. The possible explanation might be the role of a self-cleaning effect in case of spin-coating method. Therefore, before the HWE growth it is crucial to perform an in-situ substrate annealing at 600 °C in high vacuum (10<sup>-7</sup> mbar) for 15 min for the removal of the hydrogen termination and various contaminants resulting in a clean surface.

An important advantage of HWE technique is the possibility to control the thickness of the organic layer during deposition, which is not so easily and reproducibly achieved in case of spin coating. Due to the lack of thickness control in the spin-coating process in a straightforward way, the dependence of thickness on diode characteristics and detector performance has not been studied. It will be shown theoretically in Appendix A that the thickness of the organic layer defines the spatial distribution of light in the device and when correctly tuned might theoretically improve the performance.

The comparison of J-V characteristics for different C<sub>60</sub> and PCBM devices is presented in Fig. 4.45, showing a superior quality of the 25 nm annealed C<sub>60</sub> device. Based on the similarity of J-V characteristics and assuming similar properties of PCBM and C<sub>60</sub> we can conclude that the J-V of C<sub>60</sub> device can be modeled with the same recombination-generation equation as previously described for PCBM device. Due to the lack of corresponding C-V data, the barrier height and built-in field were taken from data for PCBM, in agreement with the observed photocurrent onset (associated with the barrier height), which is equal for both PCBM and C<sub>60</sub> based devices.

For  $J_0 = 9 \cdot 10^{-17}$  A/cm<sup>2</sup> the ideal generation-recombination current density as calculated from Eq. 4.50 is shown by the green line in Fig. 4.46, and the total current density including a series resistance  $R_s = 4$  kΩcm<sup>2</sup> is shown by the red line.

The 100 nm annealed device exhibits a huge series resistance and a reasonable fit can not be obtained suggesting that different unknown effects dominate the electronic transport.

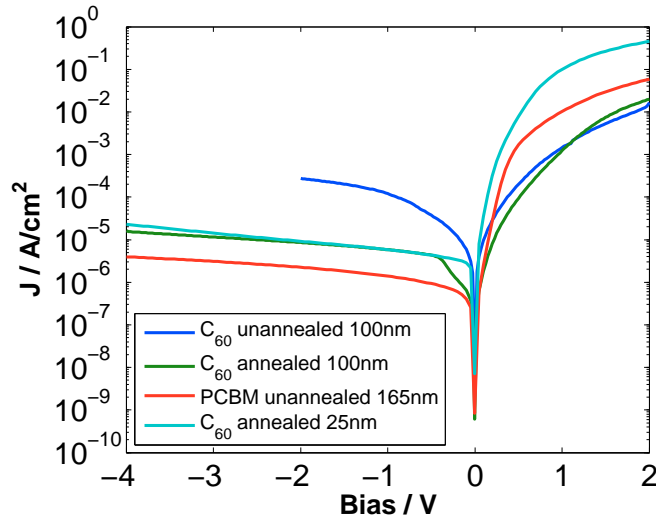


Figure 4.45: Comparison of current density-voltage characteristics Al/p-Si/C<sub>60</sub>/Al heterojunctions with and without annealing step before C<sub>60</sub> deposition and of Al/p-Si/PCBM/Al. Measured at 300 K. In each case the thickness of fullerene layer has been marked.

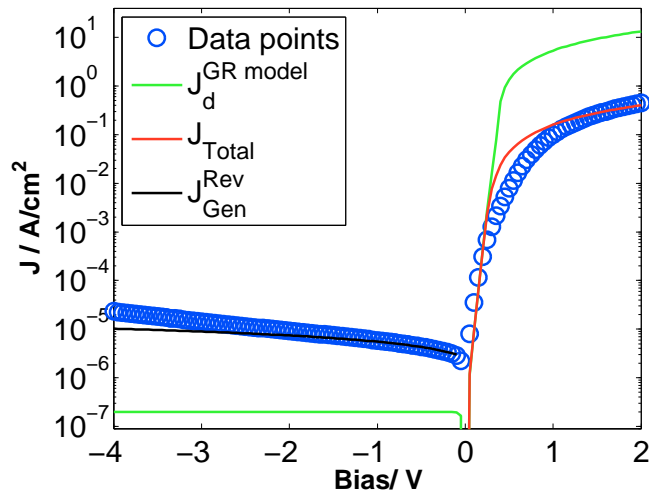


Figure 4.46: J-V characteristics of Al/p-Si/C<sub>60</sub>/Al structure. The results of the modeling using the ideal generation-recombination model (Eq. 4.50) are shown by the green line. Including parasitic series resistance, the red line results as fit to the experimental J-V curve in forward direction. For reverse bias the results of modeling using Si space charge region generation current is shown.



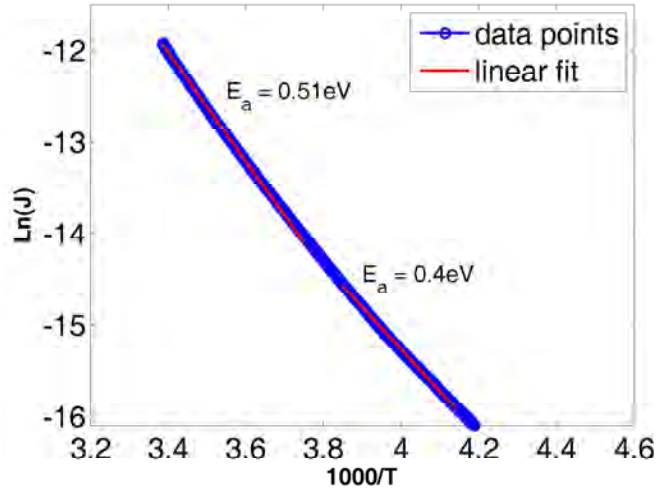


Figure 4.47: Arrhenius plot of dark current at reverse bias -1.1 V. Al/p-Si/C<sub>60</sub>/Al annealed sample, C<sub>60</sub> thickness = 25 nm.

Fig. 4.47 shows the temperature dependence of the dark current under reverse bias for the annealed 25 nm C<sub>60</sub> device. The activation energy can not be unambiguously obtained from the linear fit of the data in the whole measurement range. Possible explanation might be the presence of the phase transition of C<sub>60</sub> in the crystalline phase at 261 K (1000/3.83). Above this temperature the crystalline structure is fcc (face centred cubic) whereas below it is sc (simple cubic) structure [109]. It has been shown in literature that close to phase transition temperature many physical properties of C<sub>60</sub> exhibit anomalies [66]. However a detailed x-ray diffraction study proving the crystallinity in the case of discussed films was not performed.

The value of activation energy obtained from the fit between room temperature and 276 K (1000/3.75) is 0.51 eV ± 0.02 eV what is close to the value obtained for Si/PCBM, however the origin of dark reverse current remains similarly to previous case ambiguous within the models presented in Section 4.2.2.1.

Fig. 4.48 shows the comparison of detector performance between the studied devices. For photons energy 0.8 eV the responsivity of the annealed 100 nm thick C<sub>60</sub> device matches the responsivity of the PCBM device (with 165 nm layer), and is 3 times higher than for the unannealed 100 nm C<sub>60</sub> device. The thinner 25 nm C<sub>60</sub> device exhibits the highest responsivity, what might be related to the enhanced injection and better rectification ratio. However, the theoretical analysis of light intensity distribution in the device given in details Section A shows that the thicker sample should result in an increased photocurrent through increased absorption. The opposite obtained result suggests that photocurrent is transport limited and despite the higher amount of generated charges in case of thicker sample they are extracted and do not contribute to the observed photocurrent. More details will be given in Section 6.1.4 for the analogous case of p-Si/DiMe-PTCDI device.

The onset energy for the unannealed C<sub>60</sub> sample, and the annealed 25 nm C<sub>60</sub> sample remains the same as for the PCBM device. The apparent shift of the onset energy for the annealed 100 nm C<sub>60</sub> diode lays towards larger energies is most likely due to the fact that this particular spectra has been recorded with

30 ms integration time and is relatively noisy, therefore the correct shape of the responsivity spectra in the range close to onset value is not seen. The more detailed measurement behind germanium filter for 25 nm  $C_{60}$  device at 300 K (see Fig. 4.49), which was similarly to PCBM case difficult to record and suffered a low SNR, revealed an onset value of  $0.55\pm 0.03$  eV. i.e. in same range as for PCBM.

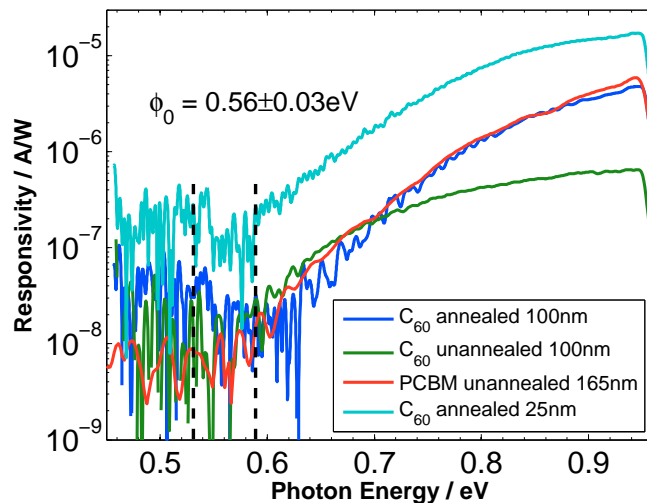


Figure 4.48: Comparison of responsivity spectra of Al/p-Si/ $C_{60}$ /Al heterojunctions with and without annealing step before  $C_{60}$  deposition and of Al/p-Si/PCBM/Al. Measured at 300 K. In each case the thickness of fullerene layer has been marked.

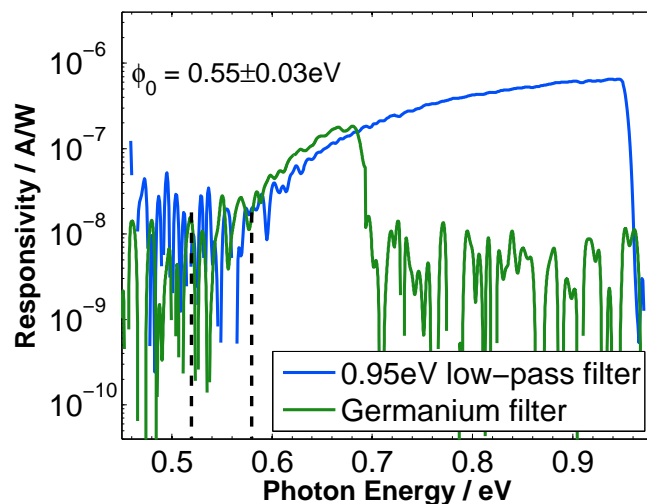


Figure 4.49: Semi-logarithmic plot, responsivity spectra of Al/p-Si/ $C_{60}$ /Al heterojunction, measured at 300 K behind germanium filter and 0.95 eV band-pass filter. The uncertainty of the onset estimation is shown. Samples fabricated without annealing step before  $C_{60}$  deposition.

The most evident difference between evaporated and annealed  $C_{60}$  devices and spin-casted PCBM was seen in the temperature dependence of responsivity spectra. In case of  $C_{60}$  devices, the signals at 300 K and 77 K were virtually the same resulting in equal responsivity spectra (see Fig. 4.50 and Fig. 4.51), whereas for the spincoated PCBM devices a significant temperature dependence is shown in Fig. 4.24.

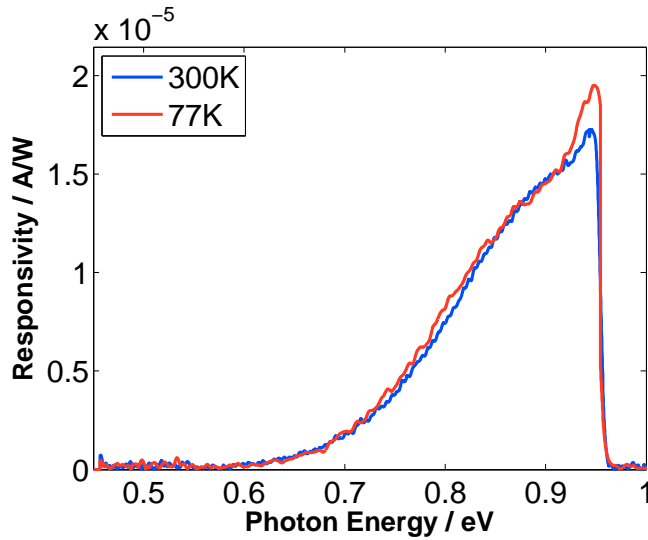


Figure 4.50: Responsivity spectra of Al/p-Si/ $C_{60}$ /Al heterojunction measured at 300 K and 77 K. Thickness of  $C_{60}$  layer was 25 nm. The sample was annealed at 600 K in vacuum right before  $C_{60}$  deposition.

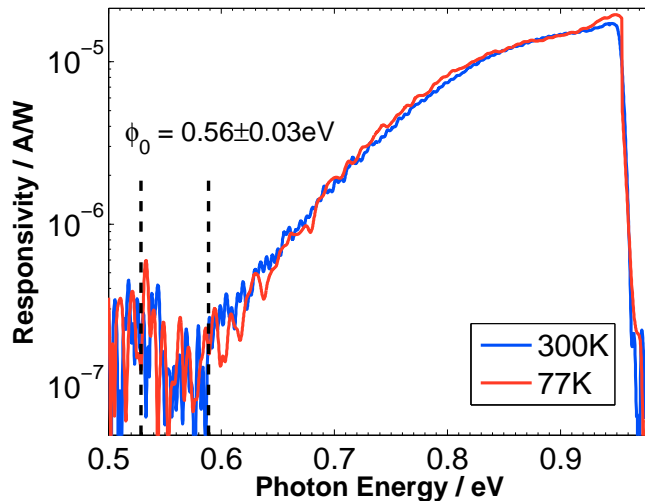


Figure 4.51: Semi-logarithmic plot. Responsivity spectra of Al/p-Si/ $C_{60}$ /Al heterojunction measured at 300 K and 77 K. The onset estimation uncertainty is shown. The sample was annealed at 600 K in vacuum right before  $C_{60}$  deposition.

Additionally the influence of metal used as a top electrode has been studied. The comparison of responsivity spectra for Al, Ag and Au top contacts

(Fig. 4.52) shows even more pronouncedly than for the PCBM devices that the spectral shape, the onset energy and responsivity value are independent of the top electrode metal.

All presented results lead to the conclusion that the sub-bandgap absorption mechanism, via which the PC is generated, and which was described in details in previous sections, is the same for all studied types of p-Si/fullerene devices.

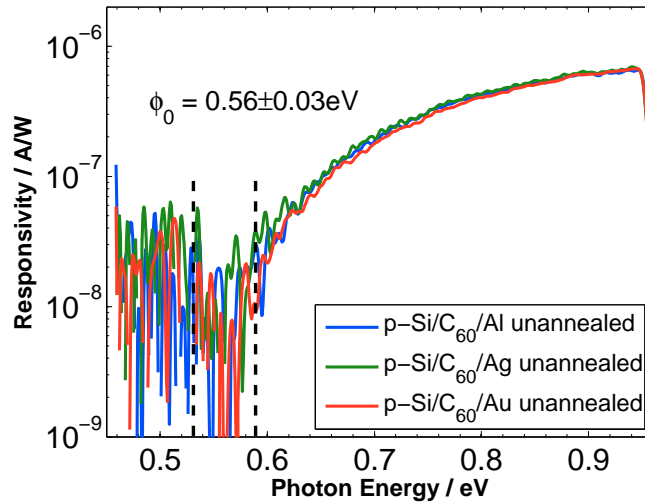


Figure 4.52: Comparison of responsivity spectra of Al/p-Si/C<sub>60</sub>/metal heterojunctions with different top electrode. Samples fabricated without annealing step before C<sub>60</sub> deposition. Measured at 300 K.

## 4.4 Reference Schottky diodes

In order to stress the significance of the invariance of the onset energy with respect to the metal used as top electrode (see Fig. 4.36), which indicates the dominant role of the p-Si/fullerene interface in the photoemission process, the electrical and the photoelectrical characteristics of p-Si/metal (Schottky diode) will be presented in the following.

As mentioned in the beginning of Section 4.2.2, typically for a rectifying metal–semiconductor contact, a photocurrent in the sub-bandgap range can be measured due to the internal photoemission phenomenon [92].

The set of Al(alloyed)/p-Si/metal samples has been prepared under the same conditions as the heterojunction diodes omitting the organic layer deposition step. Fig. 4.53, Fig. 4.54, Fig. 4.55, show the J-V characteristics for Schottky diodes with Al, Ag, and Au, fabricated on one 15·15 mm<sup>2</sup> Si substrate. None of the measured devices exhibit a rectifying behaviour at room temperature, therefore no photocurrent due to internal photoemission can be measured at this temperature (see Fig. 4.56).

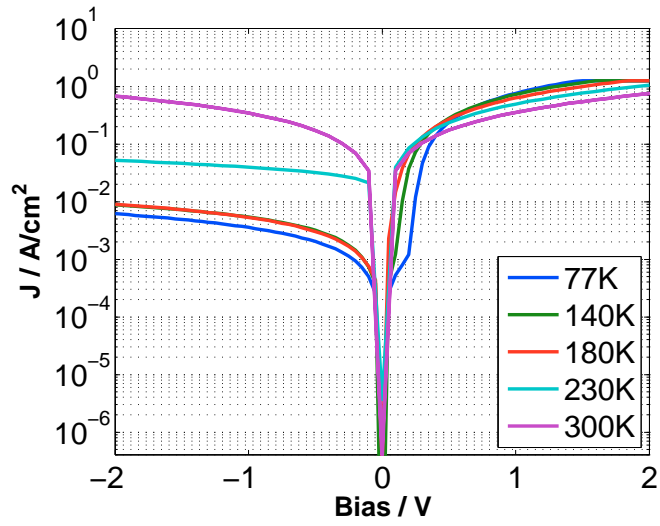


Figure 4.53: J-V characteristics of Al(alloyed)/Si/Al structure at different temperatures.

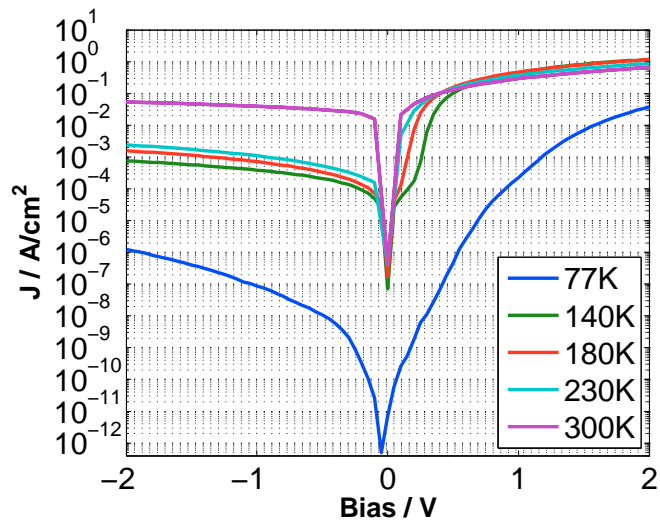


Figure 4.54: J-V characteristics of Al(alloyed)/Si/Ag structure at different temperatures.

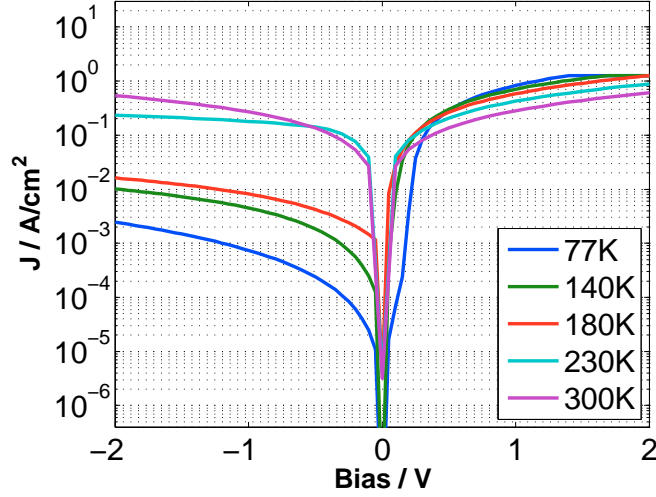


Figure 4.55: J-V characteristics of Al(alloyed)/Si/Au structure at different temperatures.

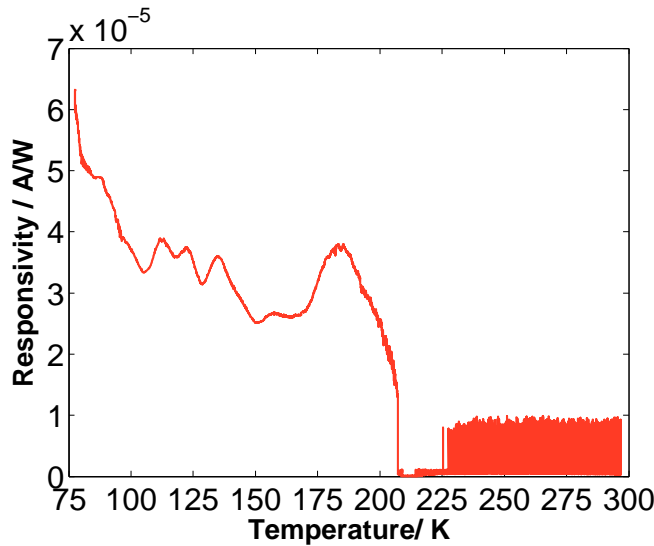


Figure 4.56: Temperature dependence of the responsivity of an Al(alloyed)/p-Si/Al Schottky diode under illumination with a  $1.55\mu\text{m}$  laser diode. Measured at short circuit condition. Above 210 K, the contact is ohmic, no barrier exist, thus no internal photoemission occurs and the measured current is the noise.

For  $T=77\text{K}$  the spectral dependence of the photocurrent shown in Fig. 4.57 and in semi-logarithmic scale in Fig. 4.58 is different for each electrode. The classic Fowler plot  $Y^{1/2}$  vs  $h\nu$  [92,93] (Fig. 4.59) yields the linear dependence only for Au and Al electrode, with small deviations suggesting that the actual exponent of Eq. 4.59 is slightly different from 2. For the device with the Ag top electrode an even higher exponent like 3 should be used. The onset energy differs between electrodes as expected from the theory and literature data. The value of the PC onset identified using the simple Fowler plot equals for Al  $\Phi_{Al} = 0.39\text{eV}$  and for Au  $\Phi_{Au} = 0.36\text{eV}$ , however, as it is seen at semi-logarithmic Fig. 4.58, in case

of gold the actual extends the lower energies and is limited by the cut-off energy 0.33 eV of the FTIR spectrometer beamsplitter spectra (see Fig. 3.5). Applying the previously introduced method for onset estimation from semi-logarithmic plot we get for Ag  $\Phi_{Ag} = 0.42$  eV.

The absolute value for the photoemission onset energy i.e. of the barrier height of a metal–semiconductor interface is strongly influenced by the existence of surface states due to surface treatment, contamination of the surface and the possible presence of few nm thick interlayers [110]. Table 4.3 shows the comparison of the values measured in this work and reported in literature.

Table 4.3: Barrier height of the Al(alloyed)/Si/metal Schottky diodes.

Metal	Barrier height measured in this work	Barrier height reported in literature
Al	0.39 eV	0.58 eV [56]
Ag	0.42 eV	0.54 eV [56]
Au	0.36 eV	0.34 eV [5]

In general literature values differ depending on the surface treatment procedures, this could explain the discrepancies between obtained onset values and the barrier height values found in literature.

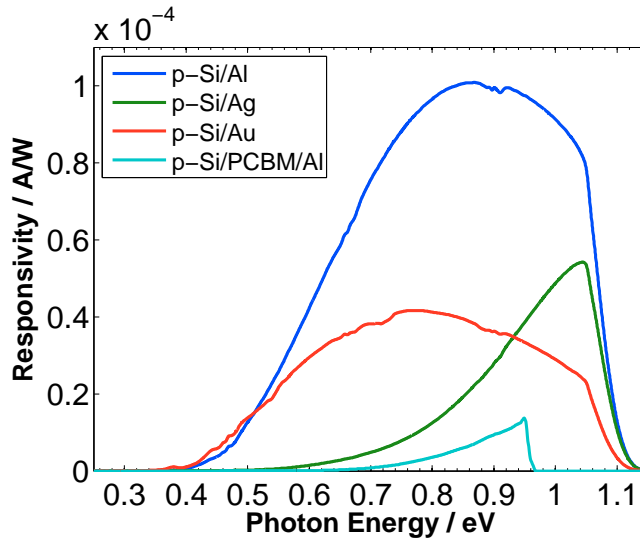


Figure 4.57: Comparison of spectral dependence of responsivity of Schottky diodes with different metals and p-Si/PCBM heterojunction. In all cases the back contact to p-Si is ohmic (alloyed Al). Measurement done at 77 K.

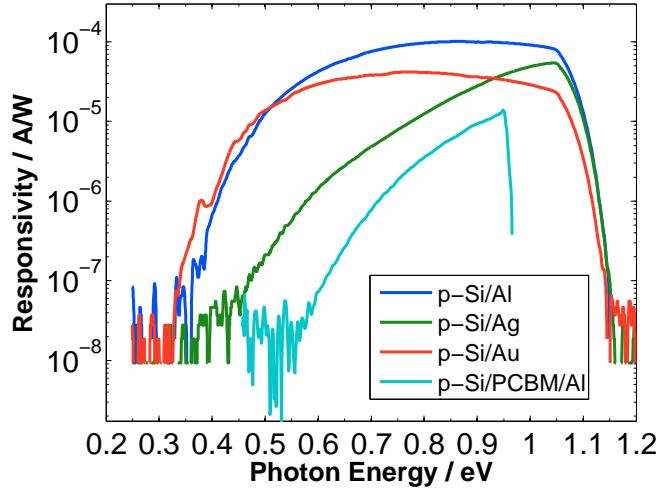


Figure 4.58: Semi-logarithmic plot. Comparison of spectral dependence of responsivity of Schottky diodes with different metals and p-Si/PCBM heterojunction measured at  $T=77$  K. In all cases the back contact to p-Si is ohmic (alloyed Al).

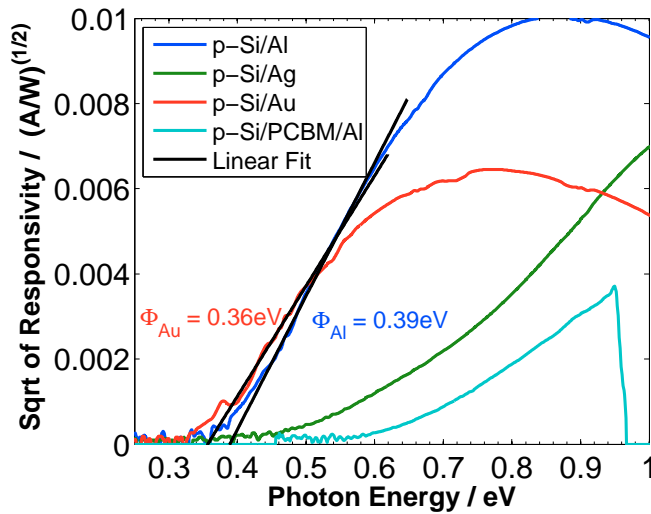


Figure 4.59: Plot in Fowler coordinates. Comparison of spectral dependence of responsivity of Schottky diodes with different metals and p-Si/PCBM heterojunction measured at  $T=77$  K.

Moreover, Fig. 4.58 shows that the onset energy for each electrode metal is different than the one measured for p-Si/PCBM/metal heterojunction diode, indicating that the sub-bandgap absorption in the IR spectral range originates from either the silicon-organic interface or the bulk of organic layer. It is important to stress that although at lower temperatures the Schottky diodes fabricated in the same procedures as silicon/PCBM heterojunctions exhibit higher responsivity (by factor 27 for 0.8 eV) they do not exhibit any photocurrent for temperatures above 207 K (see Fig. 4.56) and as such they do not present equally interesting alternative for applications as infrared sensor working at room tem-



peratures and have been presented here just for a comparative scientific reasons. The drawback of Schottky diodes as infrared sensors lies thus in the mentioned before difficulty to achieve a reproducible device with reproducible absorption spectra using low cost methods that can be easily applied in case of organic semiconductors.

# Chapter 5

## Spectrally resolved photocurrent of C<sub>60</sub> Organic Field Effect Transistors

### 5.1 Fabrication and characteristics of C<sub>60</sub> OFETS

The fabrication of the studied organic field effect transistor (OFET) has been described in [111]. The geometric structure of the device is shown in Fig. 5.4. To summarize, the device was fabricated on a glass substrate, in the first step the gate electrode was formed by evaporation of Al, followed by anodization of Al in order to form an Al<sub>2</sub>O<sub>3</sub> dielectric layer, the thickness of oxide was controlled by the bias applied during the anodization. Afterwards the alumina layer was passivated by spin coating with divinylsiloxane bisbenzocyclobutene (BCB crosslinkable resin, Dow Chemicals, brand name "Cyclotene") for improving the performance [112]. Finally a C<sub>60</sub> layer was thermally evaporated, followed by thermal evaporation of LiF/Al electrodes providing ohmic contacts to fullerene. Similar devices were reported before in [65], and showed a satisfying performance with mobilities in range of 1 cm<sup>2</sup>/Vs.

Two devices with different thickness of C<sub>60</sub> layer were studied: 100 nm and 300 nm. Fig. 5.1 and Fig. 5.2 show the output characteristics and transfer characteristics of the 100 nm device.

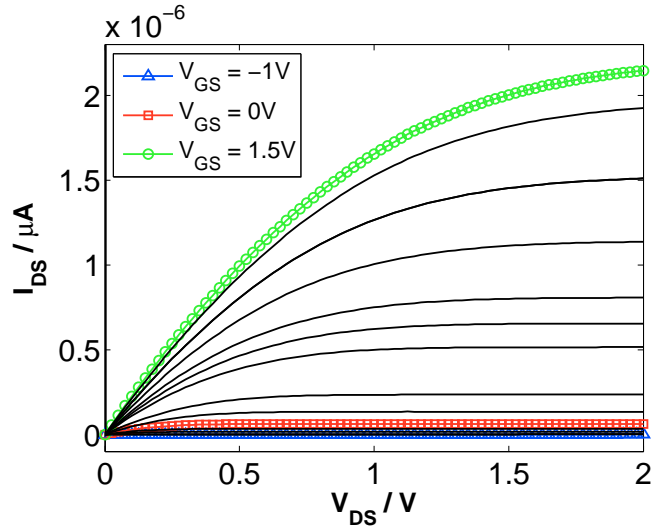


Figure 5.1: Output characteristics of studied transistor with 100 nm  $C_{60}$  layer.

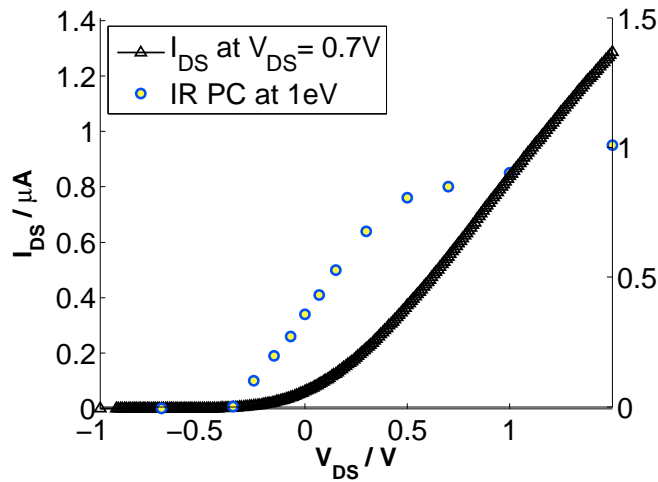


Figure 5.2: Transfer characteristics of studied transistor with 100 nm  $C_{60}$  layer. Relation of photocurrent at 1 eV vs gate voltage is shown.

## 5.2 Measurement setup of spectrally resolved drain-source photocurrent

The drain-source photocurrent of  $C_{60}$  OFET was spectrally resolved using the FTIR spectrometer setup pictured in Fig. 5.3. The main measurement regime was the same as in previously described diodes measurements, with the investigated transistor working as an external detector of the spectrometer. Due to the low signal the measurement was performed in step-scan mode allowing a long time averaging. The transistor was mounted in the measurement compartment of the spectrometer and illuminated with mechanically modulated probe beam of the spectrometer. A constant bias  $V_{DS}$  was applied between drain and source electrodes of the transistor (see Fig. 5.4). The drain-source current composing

of a constant DC component and additional light induced AC component that was fed into the signal input of lock-in amplifier. The chopper modulation signal served as reference input. The amplified in-phase signal was used as an external detector input of the spectrometer. At the same time a constant bias  $V_{GS}$  was applied to the gate electrode. The setup allowed for the variation of both applied voltages.

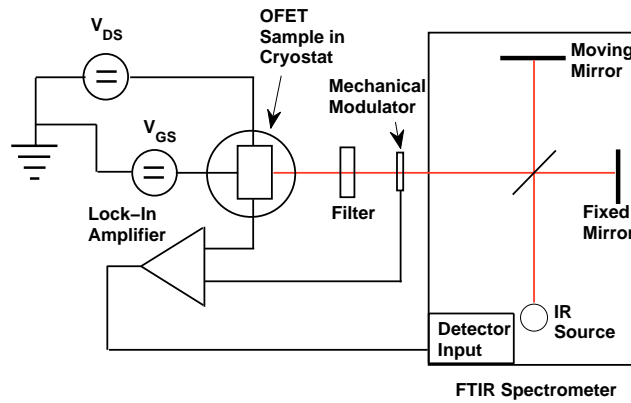


Figure 5.3: FTIR setup - measurement of spectrally resolved drain-source photocurrent of OFET

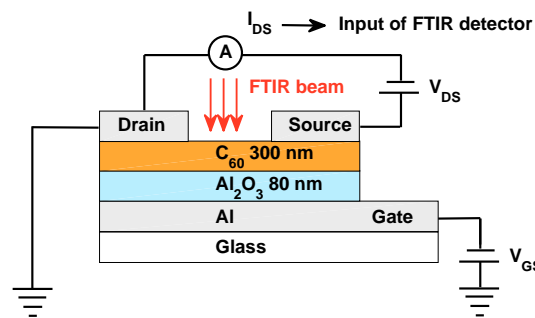


Figure 5.4: Schematic structure of studied transistor with electrical connections

### 5.3 Results, discussion and comparison with fullerene diodes

The results of the spectrally resolved drain-source photocurrent are shown for the OFET with 100 nm  $C_{60}$  layer thickness in Fig. 5.5 and Fig. 5.6 and for the OFET with 300 nm  $C_{60}$  layer thickness in Fig. 5.7, Fig. 5.8 and Fig. 5.9. These figures show that the photocurrent is activated by increasing gate voltage. The peak

around 2 eV (Fig. 5.7) is associated with band to band absorption in  $C_{60}$  with the onset energy of 1.7 eV (see Fig. 4.2 for comparison with absorption spectra). On the other hand, the low energy feature with onset in the range of  $0.52 \pm 0.03$  eV for 300 nm sample (Fig. 5.9) and  $0.51 \pm 0.03$  eV for 100 nm sample (Fig. 5.6) is not a typical absorption feature of  $C_{60}$ , and rises linearly with increasing gate voltage (Fig. 5.2). Similar behavior was seen at lower temperatures (Fig. 5.10) with a slight decrease of signal but constant photoresponse onset down to 77 K. The possible origin of the observed photocurrent is the photoexcitation of  $C_{60}^-$  anions (or negatively charged polarons), which are induced in the transistor channel by increasing gate voltage. The excitation of electron from the polaron level into the  $C_{60}$  LUMO results in a drain-source current enhancement (see Fig. 5.11 for a schematic representation of the proposed process). The fact that even at  $V_{GS} = 0$  V the photocurrent at sub-bandgap energies is measured is associated with the nature of the transistor itself. Due to its architecture, even at  $V_{GS} = 0$  V the transistor is in "on state" with current flowing (see Fig. 5.2). The photocurrent in the IR almost disappears close to -0.4 V (Fig. 5.6), around the onset of the drain-source current seen in the transfer curve.

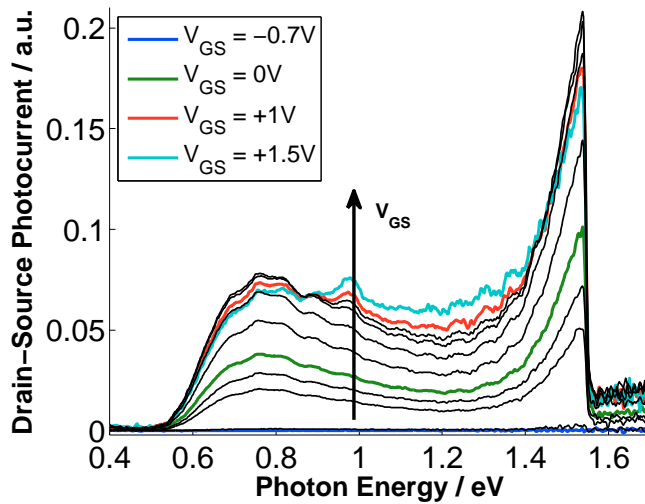


Figure 5.5: Spectrally resolved drain-source photocurrent of OFET with 100 nm  $C_{60}$  layer. Measured behind 800 nm low-pass filter, with varying gate voltage  $V_{GS}$  and constant drain-source voltage  $V_{DS} = 0.7$  V.

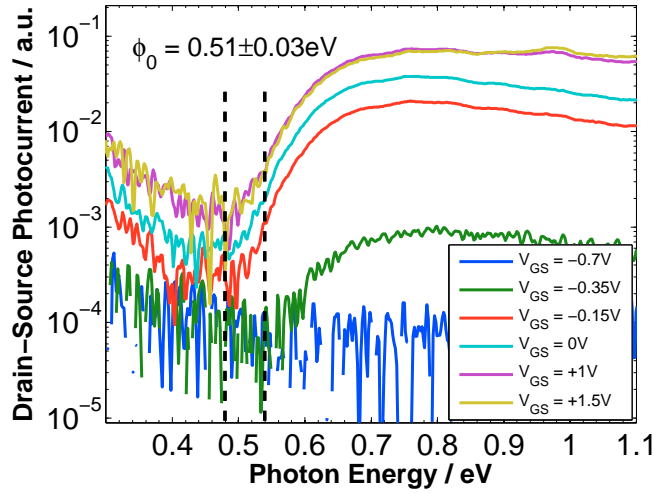


Figure 5.6: Semi-logarithmic plot, spectrally resolved drain-source photocurrent of OFET with 100 nm  $C_{60}$  layer. Measured behind 800 nm low-pass filter, with varying  $V_{GS}$  and constant  $V_{DS} = 0.7V$ .

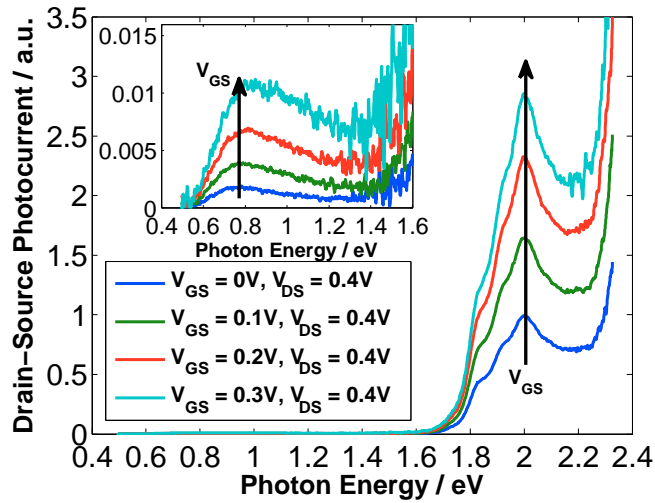


Figure 5.7: Spectrally resolved drain-source photocurrent of OFET with 300 nm  $C_{60}$  layer. Measured under full spectrum illumination of FTIR NIR lamp, with varying  $V_{GS}$  and constant  $V_{DS} = 0.4V$ . The structure at 2 eV corresponds to the HOMO-LUMO transition of  $C_{60}$ . Inset: Zoom into low energy region.

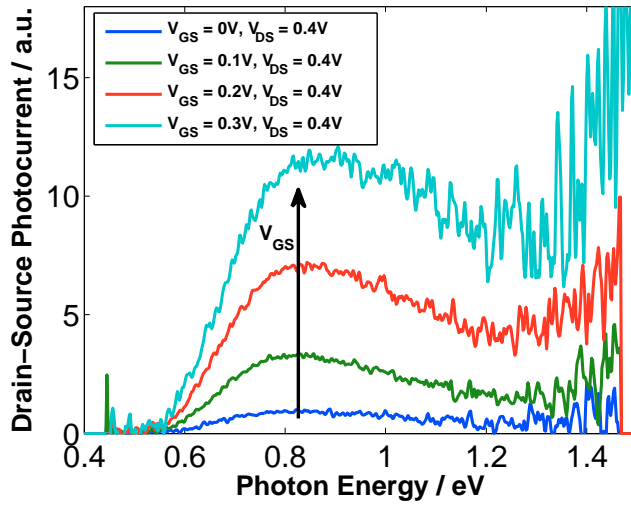


Figure 5.8: Spectrally resolved drain-source photocurrent of OFET with 300 nm  $C_{60}$  layer. Measured behind 800 nm low-pass filter, with varying  $V_{GS}$  and constant  $V_{DS} = 0.4$  V.

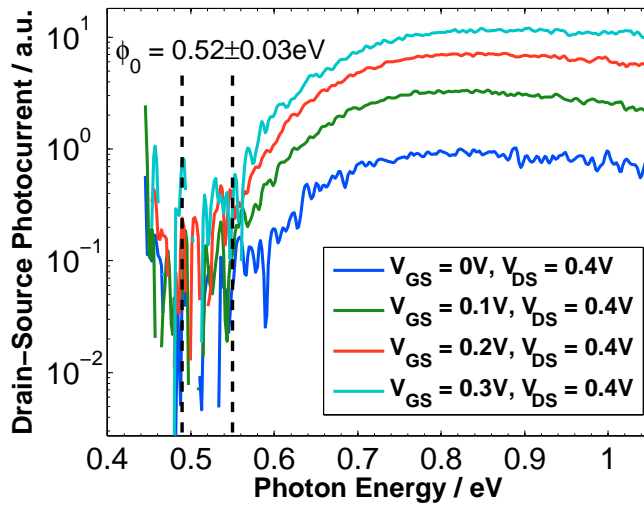


Figure 5.9: Semi-logarithmic plot, spectrally resolved drain-source photocurrent of OFET with 300 nm  $C_{60}$  layer. Measured behind 800 nm low-pass filter, with varying  $V_{GS}$  and constant  $V_{DS} = 0.4$  V.

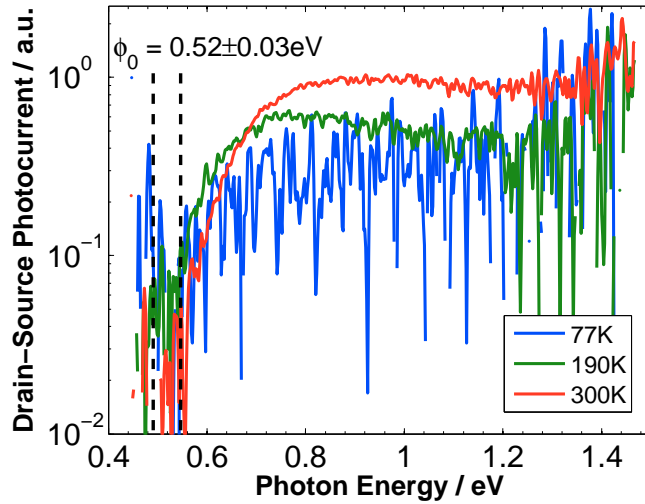


Figure 5.10: Temperature dependence of drain-source photocurrent of OFET with 300 nm  $C_{60}$  layer. Measured behind 800 nm low-pass filter, with constant  $V_{GS} = 0.4$  V and  $V_{DS} = 0.4$  V. Measured with 6 mm aperture for 300 K and 8 mm aperture for 190 K and 77 K.

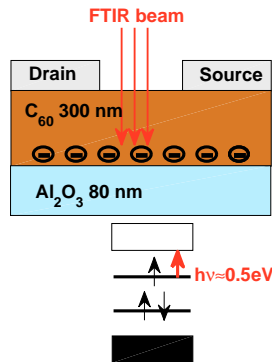


Figure 5.11: Scheme of photoexcitation of  $C_{60}$  anions and a transition of electron to LUMO state from polaron state.

The anion (polaron) excitation with onset energy close to 0.5 eV and a maximum close to 0.7 eV has been theoretically predicted in Ref [97] and Ref [98] and assigned to the transition between singly occupied molecular orbital and next LUMO level. Thus the transition was described as a consequence of the splitting of LUMO of the undoped system. The predicted excitation was experimentally measured with a photomodulation (PM) technique at both 80 K and 300 K and for modulation frequency lower than 1 kHz (the excitations was denoted as  $C_1$  in Fig. 5.12 (b) and (c)) and identified as excitation of spin 1/2 polarons ( $C_{60}^-$ ) by absorption-detected magnetic resonance technique [99]. The other photoexcitations seen in the PM spectra presented in Fig. 5.12 (a) and (b) were identified as



neutral excitations of spin 1 (triplet excitons) [99]. The calculated energy levels of all discussed excitations are shown in the inset of Fig. 5.12 (b).

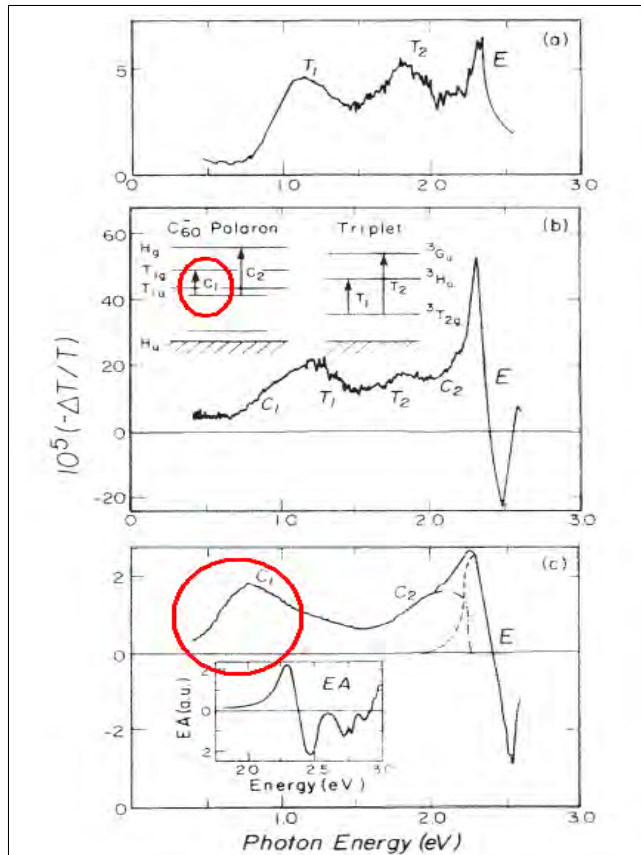


Figure 5.12: Photomodulation spectra of  $C_{60}$  film at different modulation frequency and sample temperature  $\theta$ : (a)  $f = 20$  kHz,  $\theta = 80$  K, (b)  $f = 20$  Hz,  $\theta = 80$  K, (c)  $f = 500$  Hz,  $\theta = 300$  K. Figure taken from [99]. The red circle marks the polaron excitation at energy around 0.6 eV.

The assumption of  $C_{60}^-$  absorption can be further endorsed by a photoinduced absorption (PIA) experiment performed within this work on the blend of copper-phthalocyanine (CuPC) and  $C_{60}$  [113]. In the discussed experiment a CuPC/ $C_{60}$  blend was pumped with a 720 nm (1.72 eV) laser, exciting the phthalocyanine and inducing a charge transfer into  $C_{60}$  forming a  $C_{60}^-$ , which was simultaneously probed by the FTIR beam. Fig. 5.13 shows the correspondence of OFET photocurrent spectra and PIA spectra close to the onset energy. Significant is the fact that, due to the difference in the experimental method, the peak close to 1.1 eV associated with the photoexcitation of triplet exciton [99] is seen only in the PIA experiment. In PIA the absorption of investigated sample is measured optically, thus the photo-creation of both mobile and immobile charges can be detected. Whereas in spectrally resolved photocurrent experiment only mobile photo-created charges can be detected. The presence of a  $C_{60}^-$  in zinc-phthalocyanine ZnPC/ $C_{60}$  blend upon pumping with a 633 nm (1.96 eV) laser and a subsequent charge transfer was also confirmed in the light induced electron spin resonance (L-ESR) experiment [114].

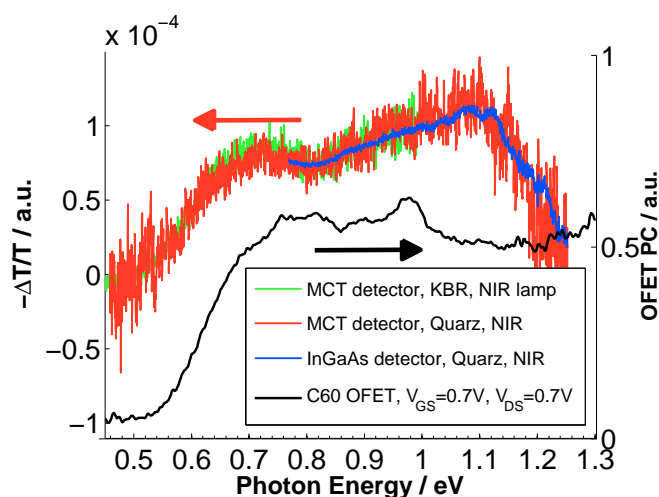


Figure 5.13: Comparison of spectrally resolved photocurrent of  $C_{60}$  OFET with spectra of photoinduced absorption (PIA) in CuPC/ $C_{60}$  blend.

Additionally a qualitative study of light intensity dependence of drain-source photocurrent was done. Fig. 5.14 shows the rise of photocurrent with increasing light intensity, realized by using different aperture size limiting the probe beam. However due to the lack of intensity measurement available a direct dependence of photoresponse on intensity can not be plotted.

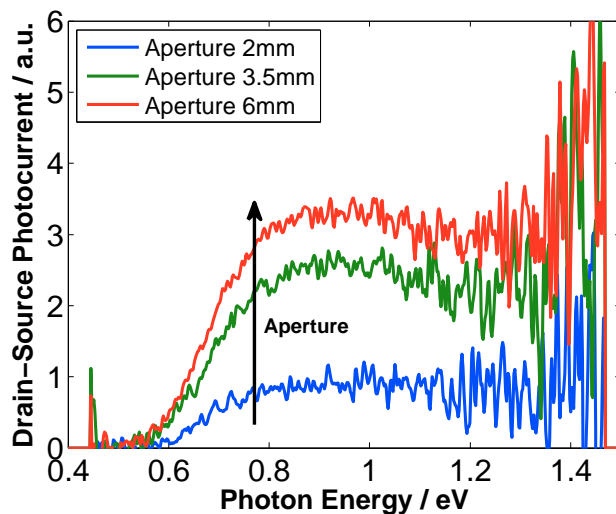


Figure 5.14: Light intensity (aperture) dependence of drain-source photocurrent of OFET with 300 nm  $C_{60}$  layer. Measured behind 800 nm low-pass filter, with constant  $V_{GS} = 0.4$  V and  $V_{DS} = 0.4$  V.

Since the sub-bandgap excitation was observed both in p-Si/fullerene heterojunction and in  $C_{60}$  based OFET it is interesting to compare both results. Fig. 5.15 reveals the photoresponse onset of 0.53 eV, i.e. virtually equal for both experiments within uncertainties  $\pm 0.03$  eV. As mentioned before such a correspondence might be a hint that the photoresponse in heterojunctions originates from excitation of a sub-bandgap localized state into delocalized band of LUMO. The

discussed state should be, analogously to transistor, understand as a polaron state, created by donation of electron tunneling from the silicon. It remains an open question whether this state is an interface or bulk state. The assumption of interface state would match with the explanation of diodes photocurrent given as pseudo-internal-photoemission, whereas bulk state interpretation would endorse the proposed mechanism of dark reverse current realized by hopping of charges through organic layer. In case of transistor one should expect an interface state since the conduction channel is usually formed at the interface between semiconductor and dielectric, however a bulk contribution can not be ruled out.

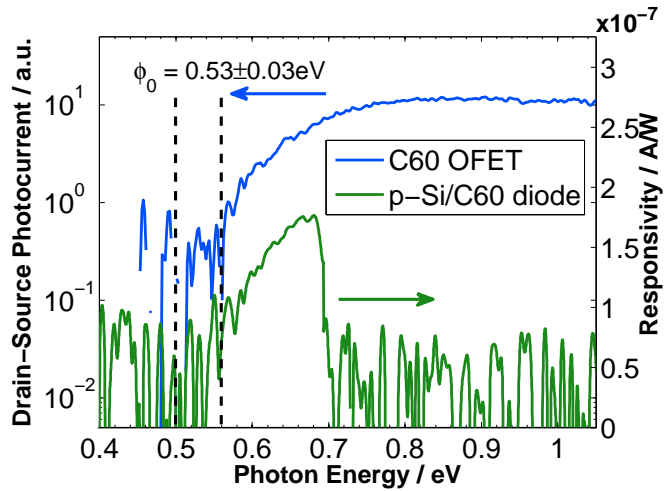


Figure 5.15: Comparison of spectrally resolved photocurrent of  $C_{60}$  OFET with photocurrent of a p-Si/ $C_{60}$  heterojunction, measured at 300 K, at short circuit condition and restricted by Ge filter.

# Chapter 6

## Other p-Si/organic heterojunction photodiodes

In this Chapter we will present the results of a study on inorganic–organic photodiodes based on various materials other than fullerenes, namely the derivative of perylene DiMe-PTCDI and two materials from the group of Indigoids (Indigo and Tyrian Purple). The analyzed devices proved to be of superior quality as compared with p-Si/PCBM devices, featuring an almost two orders of magnitude higher responsivity in the IR. A short characteristics of each of the used materials will be given at the beginning of each part, followed by the results of electrical and photoelectrical characterization of the diodes, performed in the same setups as described above. Due to a relatively high signal level in the spectrally resolved photoresponse experiments it was possible to operate the FTIR in the fast scan mode for all measurements. The calibration of the devices responsivities was performed with 0.8 eV laser diode and a calibrated InGaAs detector as described in Section 3.2.

Since equally detailed studies as for PCBM based devices have not been done, only a brief report of measurements will be given for each material. As a summary, all results will be compared and followed by conclusions towards the applicability of the photodiode operation model developed for p-Si/fullerene devices.

### 6.1 p-Si/peryene diimide heterojunction diodes

#### 6.1.1 DiMe-PTCDI material characteristics

Perylene chromophors are widely used industrially as dyes for paints, textiles, and cosmetics, allowing the realization of various colours by the utilization of alternative side groups attached to the polymer backbone. The solubility of the material can be adapted analogously.

Perylene as well as its derivatives are characterized by their thermal, chemical, and photochemical stability, i.e. a high stability to environmental factors matching the demands of industrial use [115].

In contrast to the unsubstituted perylene molecule [116], perylene diimides are considered as an electron conducting materials, and have been successfully used in organic solar cells [34, 117, 118] as well as in thin film transistors with n-type mobilities on the order of up to  $1 \text{ cm}^2/\text{Vs}$  [21, 119–121].

The chemical structure of perylene derivative N,N'-Dimethyl-3,4,9,10- Perylenetetracarboxylic diimide (DiMe-PTCDI) is shown in Fig. 6.1.

The molecule DiMe-PTCDA is made by derivatizing electron-rich perylene with two mutually-conjugated electron-withdrawing imide groups, resulting in a material with high electron affinity [122]. It is widely believed [17, 120] that the electron withdrawing imide groups are lowering the electron density as well as lowering the energetic levels of the electron-conducting  $\pi^*$  molecular orbitals (LUMO) in the inner ring  $\pi$ -system. The bandgap of DiMe-PTCDI was reported to be 2.2 eV [17].

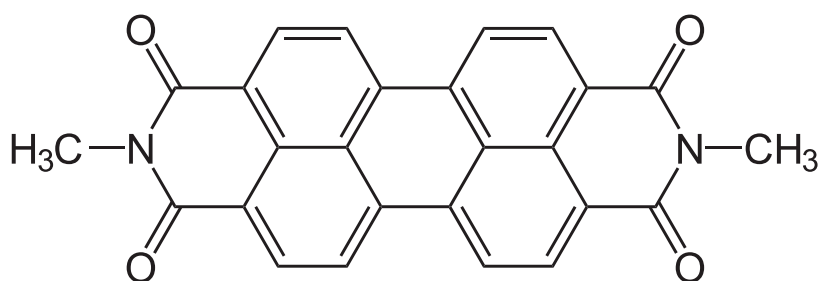


Figure 6.1: Chemical structure of the Perylene-diimide derivative: N,N'-Dimethyl-3,4,9,10-Perylenetetracarboxylic diimide (DiMe-PTCDI).

### 6.1.2 Morphology of the organic layer

The DiMe-PTCDI layer was deposited on p-Si substrate by evaporation from a hot-wall-epitaxy source at a rate of 0.1 Å/s, see Section 3.1 for details. The scanning electron microscope images in Fig. 6.2 and Fig. 6.3 show the formation of a closed DiMe-PTCDI layer on top of the p-Si substrate. From the topography of the DiMe-PTCDI surface, it appears that crystallites with a lateral dimensions of several hundred nanometers are formed. Such a formation of a closed layer followed by crystallites is a growth mode which typically arises, if the interaction of the molecules with the substrate (e.g. within the first few monolayers of growth) is dominant in comparison to the intermolecular attraction. With increasing layer thickness the growth is not anymore dominantly influenced by Si surface, and the intermolecular attraction between the DiMe-PTCDI molecules leads to the formation of crystallites [123].

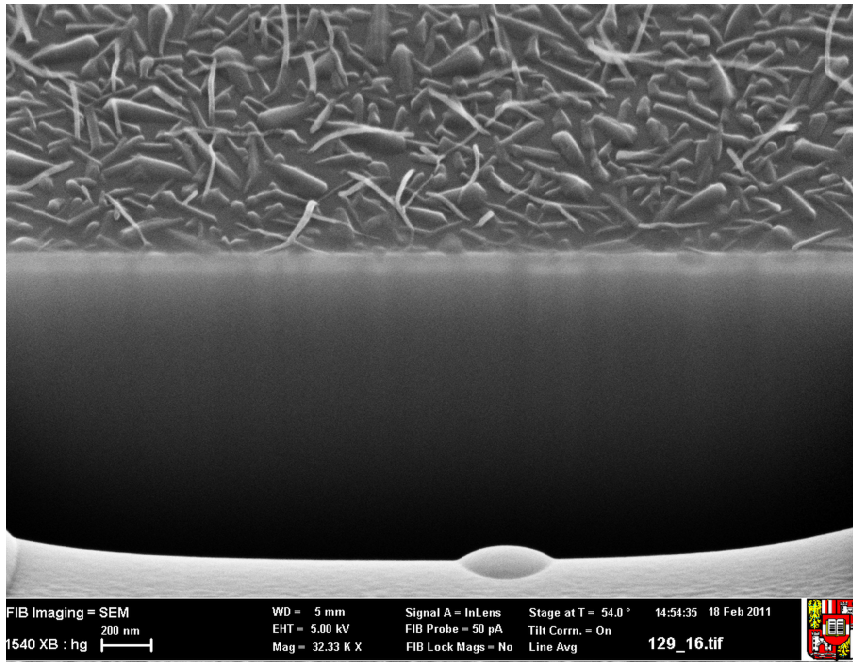


Figure 6.2: Scanning electron microscope cross section (viewing angle is  $45^\circ$ ) of the DiMe-PTCDI/p-Si heterojunction. A groove through the heterojunction is made with an focused ion beam (FIB). The groove is not ‘sharp’ and the resulting contrast in the picture is not uniform as seen by the gray regions.

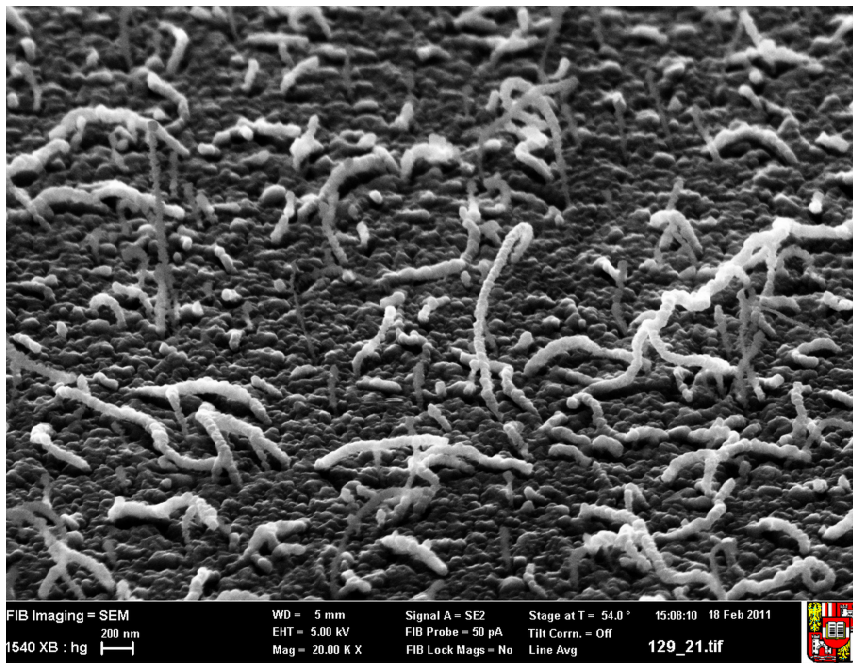


Figure 6.3: Scanning electron microscope picture of surface of DiMe-PTCDI/p-Si heterojunction. Viewing angle is  $45^\circ$ .

### 6.1.3 Electrical characteristics

Fig. 6.4 shows the current density-voltage characteristics of Al/p-Si/DiMe-PTCDI/Al heterojunction with thickness of organic layer on the order of 25 nm, measured at 300 K and 77 K. The diodes exhibited generally similar dependence to the p-Si/PCBM diodes with similar observed rectification ratio of  $1 \cdot 10^4$ , between -2V to +2V at 300 K and  $7.4 \cdot 10^{10}$  at 77 K what is in comparison with fullerene device two times lower at 300 K and in the same range at 77 K. On the other hand the series resistance hampering the injection in forward direction was in perylene devices lower, resulting in an order of magnitude higher current density at 2 V.

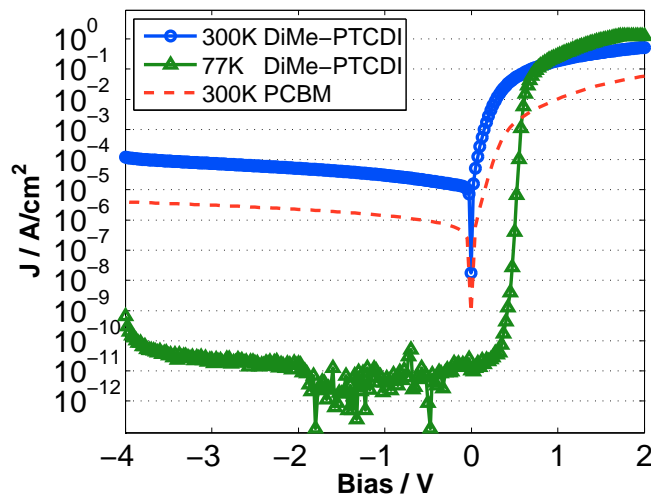


Figure 6.4: Current density-voltage characteristics Al/p-Si/DiMe-PTCDI/Al heterojunction measured at 300 K and 77 K. Thickness of organic layer was 25 nm. Additionally the characteristics of Al/p-Si/PCBM/Al at 300K is shown for comparison.



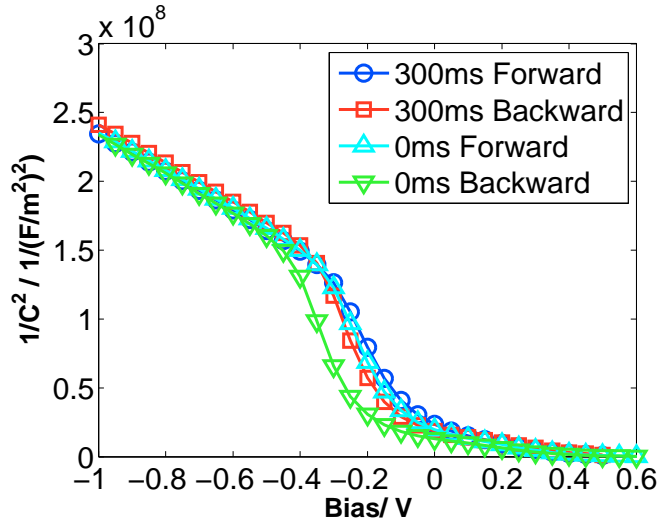


Figure 6.5:  $1/C^2$  vs  $V$  characteristics of Al/p-Si/DiMe-PTCDI/Al heterojunction, measured at 300 K and frequency 1 kHz, with 300 ms and 0 ms delay between each measurement point. The voltage sweep was done starting from -1 V to +1 V (Forward direction) and subsequently without releasing the bias from +1 V to -1 V (Backward direction).

Fig 6.5 shows the result of capacitance-voltage analysis on DiMe-PTCDI device. The presence of a barrier for charge carriers is clearly visible, however a detailed study of voltage dependence revealed a hysteresis of the capacitance values. The measurement was done in two modes: for increasing and subsequently for decreasing external bias from -1V to +1V and +1V to -1V, and in the opposite direction starting at +1V to -1V and back. Regardless of the starting point the result remained the same, suggesting that the crucial part is the decrease of bias into negative direction where a shift in the  $1/C^2$  curve in negative direction is observed. The magnitude of the shift depends on the time delay between the measurement steps. For a longer time (300 ms) the hysteresis is very small and extends for a fast measurement done with 0 ms delay. This suggests that charge traps are present at the interface and/or in the bulk of organic material. However a more detailed transient studies would be necessary to analyze the nature and the energy of those levels. It is clear that the application of the C-V model developed for p-Si/PCBM devices might lead to erroneous conclusions in the presence of charge traps, therefore a  $V_{bi}$  estimation from C-V measurement was not performed.

Nevertheless, based on the fact that the LUMO level in pristine DiMe-PTCDI was measured electrochemically to be at -4.15 eV i.e. similarly to fullerenes higher than the VB of Si (-4.8 eV [82]), we assumed at least qualitatively a similar band alignment at the interface. Moreover, by assuming that the barrier height is associated with the onset of photocurrent ( $0.45 \pm 0.03$  eV see Fig. 6.13), the electron conducting extended electronic states (i.e. the LUMO and the higher unoccupied states) of the organic thin film are energetically within the bandgap of the p-Si. The assumed value of barrier height allows us to draw a schematic picture of energy-band alignment at the interface (see Fig. 6.6).



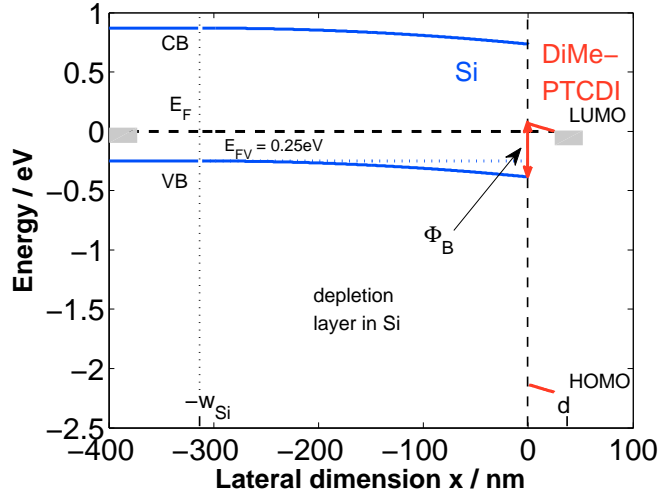


Figure 6.6: Energy-band diagram for the Al/p-Si/DiMe-PTCDI/Al heterojunction photodiode at zero bias. Parameters used in energy levels calculation:  $\epsilon_{DiMe-PTCDI}$  [124],  $d = 25$  nm.

At forward bias (p-Si positive relative to the DiMe-PTCDI) electrons are efficiently injected from the Al top-contact into the DiMe-PTCDI layer. The electron injection from the DiMe-PTCDI into the Si conduction band (CB) is energetically unfavorable and the current has to traverse the inorganic-organic interface as a recombination current between electrons in the DiMe-PTCDI and holes in the p-Si. However due to possible influence of interface trap states seen in the hysteresis of C-V data, we do not present an equally detailed analysis as given for PCBM.

On the other hand, since the width of the depletion layer in Si is on the same order as in PCBM based device (compare Fig. 4.10 and Fig. 6.6), the almost two order of magnitude larger reverse current can not be attributed to the generation in the Si space-charge region. Alternative transport channels like enhanced interface tunneling due to for example band bending in the DiMe-PTCDI layer or hopping via deep trap states have to be assumed. Those channels are opened by the tempering step, since without this step, dark current densities in agreement with the Si space-charge generation-recombination model are observed.

Also for the activation of the dark-reverse current features inconsistent with the Si space charge generation-recombination model are observed. In Fig. 6.7 it is shown that the dark reverse current is thermally activated with the two distinctive activation energies estimated to be  $0.47 \pm 0.02$  eV for temperatures between 250 K and 300 K, and  $0.22 \pm 0.02$  eV for temperatures lower than 200 K.

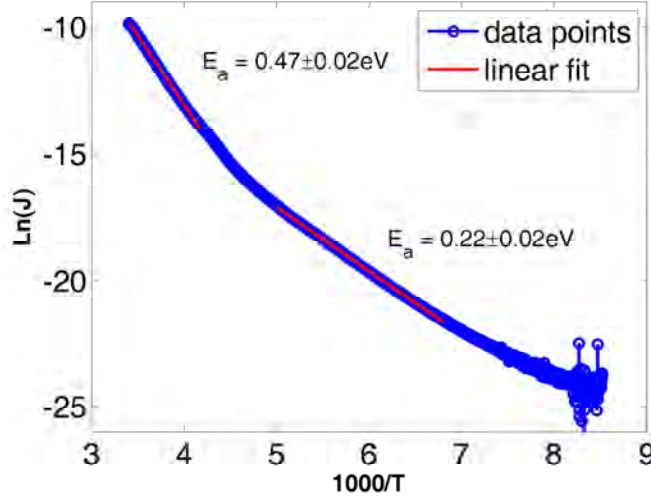


Figure 6.7: Arrhenius plot of dark current at reverse bias -1.1 V.

### 6.1.4 Photoresponse - spectrally resolved photocurrent

In this section the results of photoresponse spectral studies of Al/p-Si/DiMe-PTCDI/Al devices will be shown, with focus on a detailed estimation of PC onset energy, the temperature dependence and the influence of the organic layer thickness on the responsivity values.

At the beginning we will present the complementary current density-voltage characteristics under illumination of the device presented in the previous Section under dark conditions. The photovoltaic effect is observed at room temperature (Fig. 6.8) as well as at 77 K (Fig. 6.9) under the illumination of both the spectrally restricted NIR lamp of FTIR spectrometer and a laser diode emitting at 0.8 eV. Fig. 6.10 and Fig. 6.11 show the room temperature and 77 K J-V characteristics presented in the linear scale. The observed open circuit voltage  $V_{OC}$  at room temperature was close to 10 mV under the illumination of a 0.8 eV laser diode, whereas at 77 K it was in the range between 0.33 V to 0.37 V depending on the light source used.

The short circuit current density  $J_{SC}$  under 0.8 eV laser diode illumination was  $4.3 \mu\text{A}/\text{cm}^2$  at room temperature and  $5.8 \mu\text{A}/\text{cm}^2$  at 77 K. The measured value of  $J_{SC}$  corresponds to a signal-to-noise ratio of 242 (see Fig. 6.12).

A more detailed temperature dependence of  $J_{SC}$ , under illumination converted to responsivity is presented further on in Fig. 6.14 and Fig. 6.15 .

Fig. 6.8 and Fig. 6.10 reveal a photoconductivity effect under forward bias, with signal-to-noise ratio in the range of 1 to 2. The origin of this photocurrent could be possibly ascribed to the optical excitation of electrons trapped in localized states at the interface and/or bulk of the organic material. Those states might be responsible for hysteresis observed in C-V measurement. However, a more detailed studies of spectrally resolved photoresponse at forward bias is required to identify the origin of observed photoconductivity.

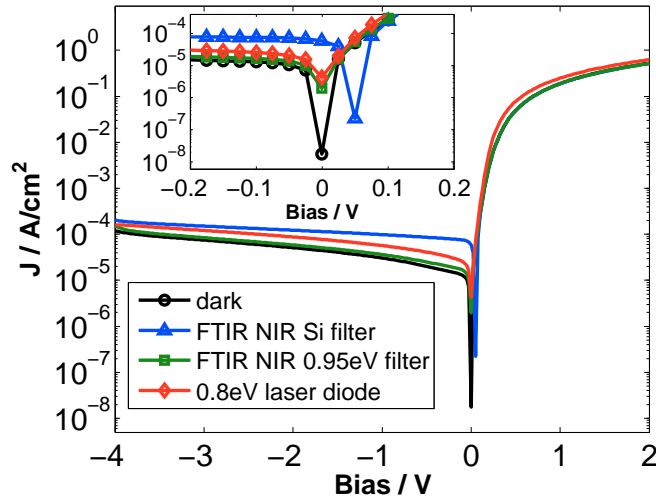


Figure 6.8: The comparison of J-V characteristics of Al/p-Si/DiMePTCDI/Al diode in dark and under illumination with a tungsten lamp of FTIR spectrometer restricted with Si filter and with 0.95 eV band-pass filter and a J-V characteristic under illumination with a laser diode emitting at 0.8 eV ( $1.55 \mu\text{m}$ ) with power of  $\approx 200 \text{ mWcm}^{-2}$ . Measured at room temperature.

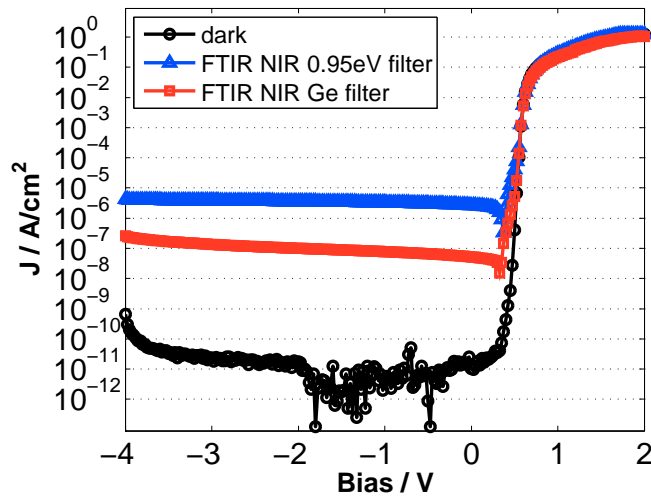


Figure 6.9: The comparison of J-V characteristics of Al/p-Si/DiMePTCDI/Al diode in dark and under illumination with a tungsten lamp of FTIR spectrometer restricted with 0.95 eV band-pass filter and with Ge filter. Measured at 77 K.

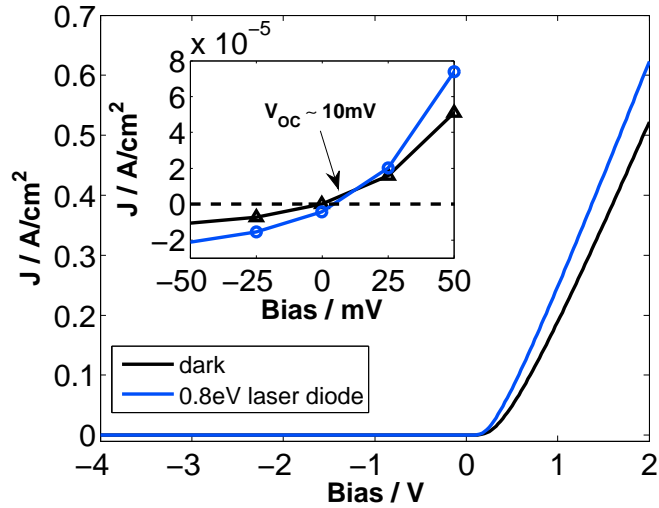


Figure 6.10: J-V characteristics of Al/p-Si/DiMe-PTCDI/Al diode measured at 300 K in dark and under illumination of a laser diode emitting at 0.8 eV ( $1.55 \mu$ ) with power of 4.9 mW. The open circuit voltage is shown.

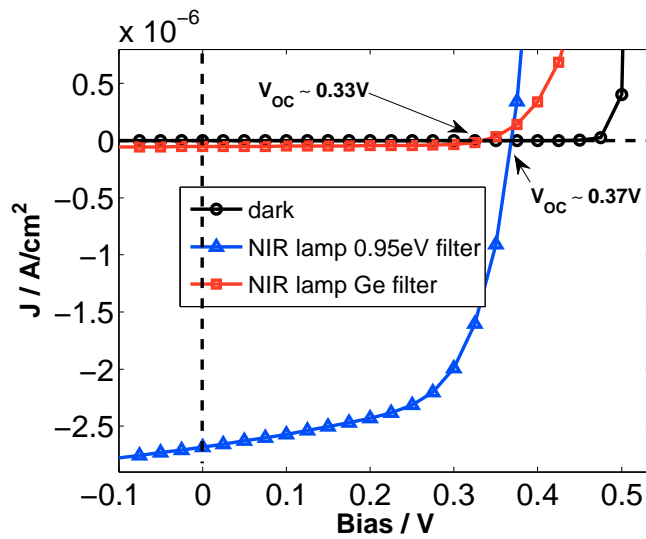


Figure 6.11: J-V characteristics of Al/p-Si/DiMe-PTCDI/Al diode measured at 77 K in dark and under illumination of spectrally restricted tungsten lamp of FTIR spectrometer. The open circuit voltage is shown.

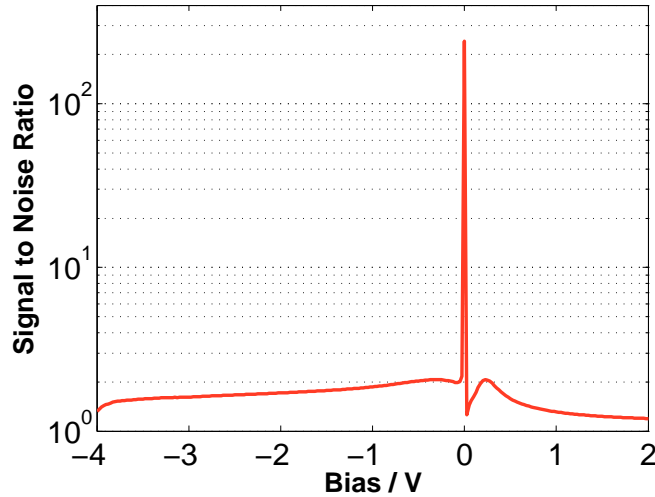


Figure 6.12: Signal to Noise Ratio of Al/p-Si/DiMe-PTCDI/Al diode measured at 300 K under illumination of a laser diode emitting at 0.8 eV ( $1.55 \mu$ ) with power of 4.9 mW.

To get the possibly best insight into the onset energy of photocurrent at short circuit condition a spectral measurement with tungsten lamp restricted by germanium filter was done. Fig. 6.13 shows the result of the measurement at 300 K. The estimated onset energy is  $0.45 \pm 0.03$  eV.

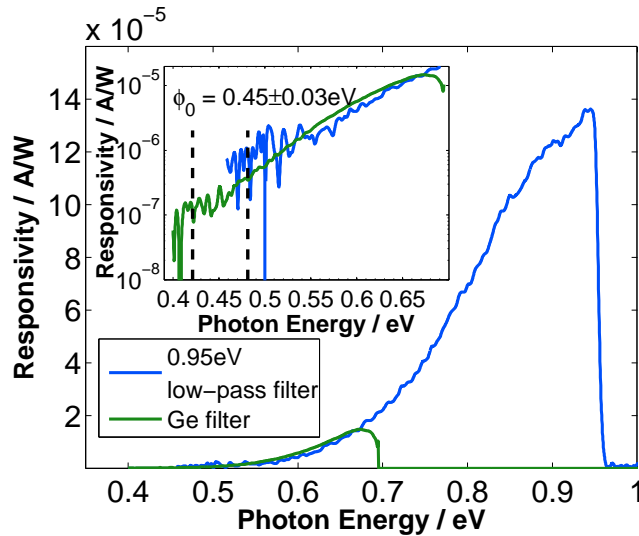


Figure 6.13: Responsivity spectra of Al/p-Si/DiMe-PTCDI/Al heterojunction, measured short circuit condition, at 300 K, behind 0.95 eV band-pass filter and Ge filter. Thickness of DiMe-PTCDI layer was 25 nm Inset: semi-logarithmic plot, the uncertainty of onset estimation is shown.

From the detector performance point of view it is important to point out that the responsivity of perylene based device at photon energy 0.8 eV equals  $6.94 \cdot 10^{-5}$  A/W, what is an order of magnitude higher than for the  $C_{60}$  based device and almost two orders of magnitude higher than for the spin-casted PCBM based device (see Tabel 7.1 for comparison).

Fig. 6.14 shows the temperature dependence of a short circuit photoresponse spectra measured behind a 0.95 eV band-pass filter.

The detail study behind germanium filter of the temperature dependence on onset energy has not been done and

As can be seen from the inset of Fig. 6.14 for the given very low signal-to-noise ratio close to the photoresponse onset, the onset value seems to be independent of the temperature and is estimated to be  $0.55 \pm 0.03$  eV. This results is 0.1 eV higher than the more accurate value obtained from the measurement using Ge filter for 300 K. Figures 6.14 and 6.15 reveal the temperature dependence of the responsivity. For a photon energy of 0.8 eV at 300 K a drop to 80% of the value at 77 K is observed, what indicates a better temperature stability than for the PCBM device where a drop to 50% was observed (see Fig. 4.25). However for  $C_{60}$  device no significant difference between 300 K and 77 K in photoresponse was observed (see Fig. 4.51).

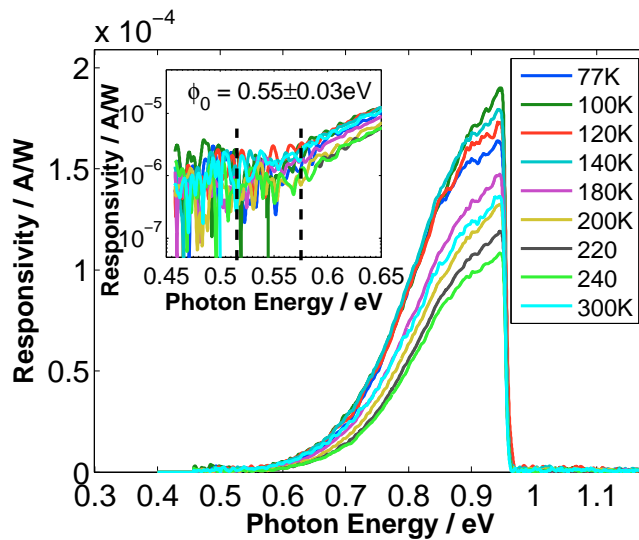


Figure 6.14: Temperature dependence of responsivity spectra of Al/p-Si/DiMe-PTCDI/Al heterojunction, measured behind 0.95 eV band-pass filter. Thickness of DiMe-PTCDI layer was 25 nm Inset: semi-logarithmic plot, the uncertainty of onset estimation is shown.

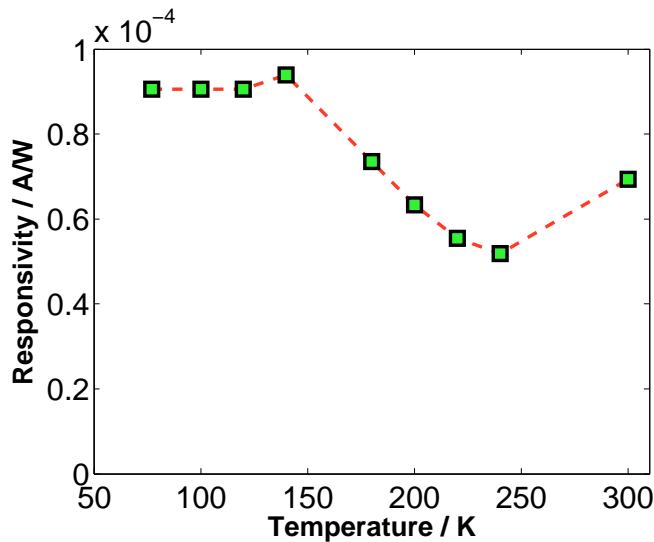


Figure 6.15: Temperature dependence of responsivity of Al/p-Si/DiMe-PTCDI/Al heterojunction measured at 0.8 eV ( $1.55 \mu\text{m}$ ).

To study the dependence of the responsivity on the organic layer thickness, three different sets of samples were fabricated with 100 nm, 25 nm and 12 nm thickness. The superior sample proved to be the one with 25 nm thick DiMe-PTCDI layer, see Fig. 6.16 and Fig. 6.17, showing around two orders of magnitude higher responsivity than for the 12 nm and 100 nm samples. However the theoretical analysis of light intensity distribution in the device presented in Appendix A shows that the thicker sample should result in an increased photocurrent through increased absorption. However, since the absorption in discussed case is a sub-bandgap process, for simplicity the model used in Appendix A assumed a non-absorbing media (extinction coefficient  $k = 0$ ) and allowed only calculation of light intensity distribution in the multilayer structure. Assuming only interface absorption, for a 100 nm thick structure around 3.3 times more light (photon energy 0.8 eV) is present at the interface than for a 25 nm (see Fig. 6.18). If we include the possible additional bulk absorption through excitation of charges from localized sub-bandgap levels into delocalized LUMO level the influence of thickness in the total absorption is even higher, an integration over the total thickness of the light intensity distribution function predicts an order of magnitude higher intensity of absorbed light of 0.8 eV energy for a 100 nm sample than for 25 nm sample (see Fig. 6.19). The opposite obtained result suggests that the photocurrent, regardless of the actual generation mechanism, is transport limited and despite the higher amount of generated charges in case of thicker layers they are not able to be extracted and contribute to the observed photocurrent. The limitation might be related to the increased number of boundaries between crystallites and/or to the reduction of grain sizes in the material that would hamper the transport and reduce the effective mobility severely [125, 126]. On the other hand the 12 nm thick sample resulted in a two orders of magnitude lower PC than the 25 nm sample, from the transport limitation point of view the opposite should be expected, and from the light intensity distribution point of view a decrease for the thinner sample of only factor 2 in case of interface effect and factor 3.4 in case of bulk effect is predicted. This might suggest that for such a thin layer, the layer morphology is different as compared the thicker layers and

leads to a more complicated picture of thickness dependent transport limitation. In general one should expect an optimal thickness for which all competing processes are balanced. A further study with a broader range of thickness including device performance measurement, transport properties and morphology should be performed to clarify this issue.

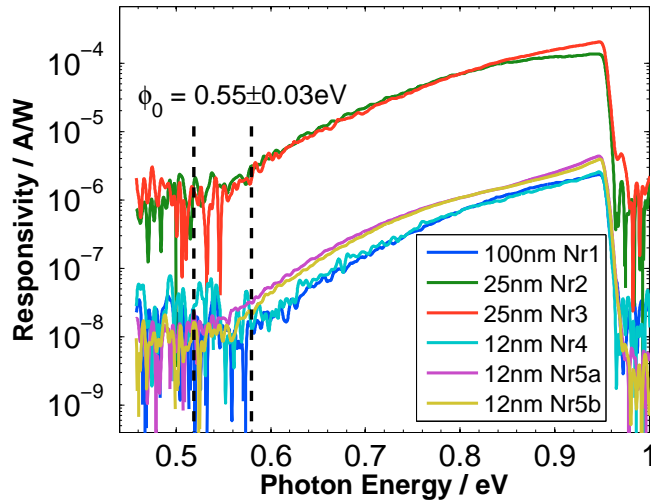


Figure 6.16: Dependence of the responsivity spectra on organic layer thickness of Al/p-Si/DiMe-PTCDI/Al heterojunctions.

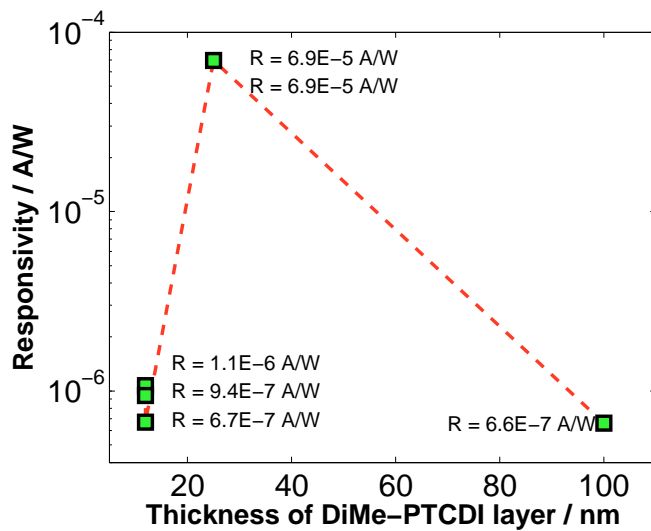


Figure 6.17: Dependence of the responsivity spectra on organic layer thickness of Al/p-Si/DiMe-PTCDI/Al heterojunction measured at 0.8 eV ( $1.55 \mu\text{m}$ ). The labels for each point indicate the statistical variation of the responsivity values measured for different devices.



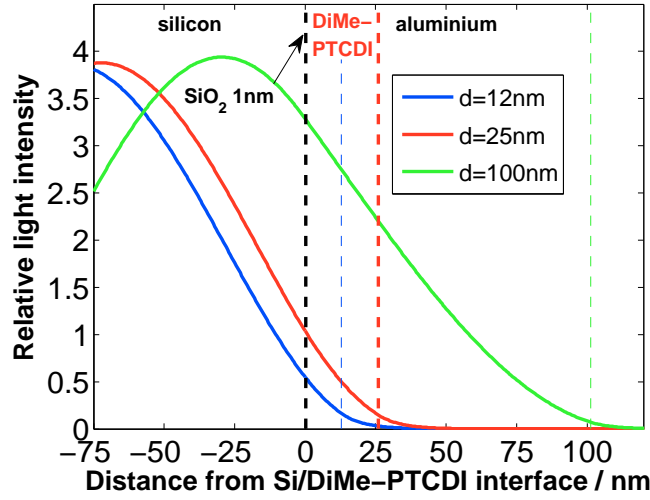


Figure 6.18: Distribution of light intensity in p-Si/SiO<sub>2</sub>/DiMe-PTCDI/Al multilayered structure for photon energy 0.8 eV, for three DiMe-PTCDI layer thicknesses. Based on Eq. A.19, with following parameters: thickness of native oxide SiO<sub>2</sub> = 1 nm as measured by ellipsometry on Si wafer kept for hours in air,  $d_{DiMe-PTCDI} = 25$  nm,  $d_{Al} = 100$  nm, refractive indexes of all materials as presented Table A.

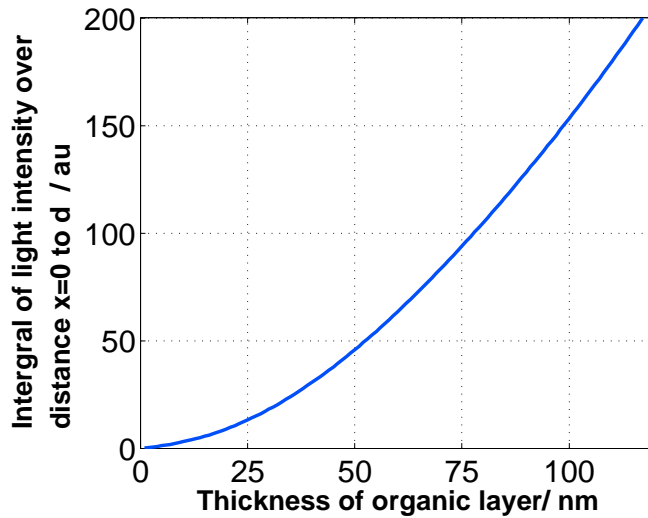


Figure 6.19: Relative light intensity for a photon energy of 0.8 eV absorbed in the whole bulk of organic layer (integrated from  $x = 0$  to  $d$ ) according to Eq. A.20 as a function of the organic layer thickness.

### 6.1.5 The influence of p-Si surface treatment on electrical characteristics and photoresponse

Similarly to the results presented in Section 4.3 for C<sub>60</sub> based diodes, the crucial point in device fabrication is the thermal treatment of silicon surface right before

the deposition of organic material, resulting in a surface clean of various contaminants and free of hydrogen termination. The discussion presented in previous Sections refers to samples that were annealed at 600 K before the deposition of organic layer. In the following Section they will be compared qualitatively with the sample fabricated without annealing step.

It has been reported in literature that the special surface treatment might enhance the interaction of organic molecules with the surface. Particularly a dipole layer formation at the interface between perylene derivatives PTCDA and DiMe-PTCDI and Se and S passivated GaAs surface was reported in [127, 128] and a chemisorption of PTCDA on clean unpassivated Si surface was reported in [123].

In our previously presented model, the origin of the photoresponse remains ambiguous being dominantly either related to interface generation or bulk excitation of electrons. Nevertheless, in both cases the interface plays an important role since even in bulk excitation model we defined a surface tunneling process which is a part of conduction mechanism through localized states. Thus an enhancement of interface interaction at the surface might be responsible for an almost two orders of magnitude increase of photoresponse observed in the samples that were annealed. Table 6.1 summarizes the responsivities of various perylene diimide based diodes.

Table 6.1: Comparison of responsivity at 0.8 eV of p-Si/DiMe-PTCDI devices annealed at 600°C before deposition of organic layer and unannealed devices

Sample	Thickness	Responsivity / A/W
Nr 1 annealed	100 nm	6.6E-07
Nr 2 annealed	25 nm	6.9E-05
Nr 3 annealed	25 nm	6.9E-05
Nr 4 annealed	12 nm	6.7E-07
Nr 5 annealed	12 nm	1.1E-06
Nr 6 unannealed	25 nm	1.1E-06
Nr 7 unannealed	25 nm	4.5E-07

Interesting to see is the difference in J-V characteristics between annealed and unannealed devices (Fig. 6.20). The unannealed samples exhibit a higher series resistance thus a more non-ideal characteristics in the forward direction, what might be intuitively explained in terms of contribution of contamination for the series resistance. On the other hand those samples at the same time exhibit under the reverse bias a current density at the same level as PCBM based devices, which is 30 times lower current than for the annealed DiMe-PTCDI based devices, as explained in Section 6.1.3.

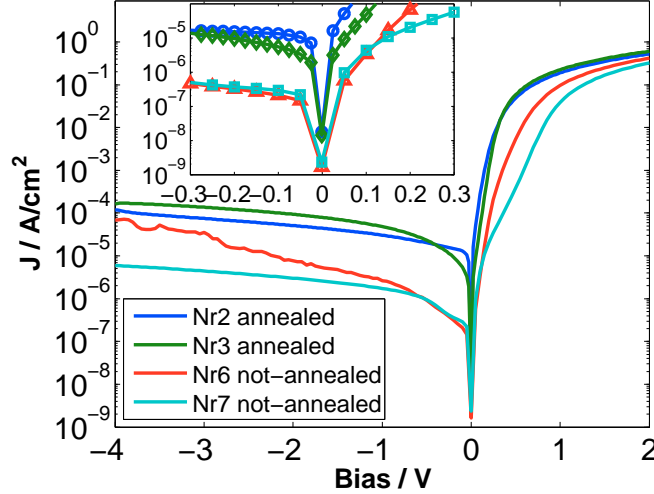


Figure 6.20: Comparison of J-V characteristics of p-Si/DiMe-PTCDI devices annealed at 600°C before deposition of organic layer and unannealed devices. Thickness of organic layer in all cases was 25 nm.

## 6.1.6 Photodetector performance

### 6.1.6.1 Detectivity measurements

To further characterize the studied device as a potential candidate for a practical IR-detecting applications, the specific detectivity  $D^*$  is calculated.  $D^*$  is an efficient figure of merit and is defined by the reciprocal of the noise equivalent power per bandwidth (NEP) normalized to the detector sensitive area  $A$ , and is given by:

$$D^* = \sqrt{A}/\text{NEP} \quad (6.1)$$

where  $\text{NEP} = \sqrt{\langle i_n^2 \rangle / \Delta f} / R$ ,  $R$  is the responsivity,  $\langle i_n^2 \rangle / \Delta f$  is the mean square of the thermal noise current per bandwidth  $\Delta f$ . In Fig. 6.21 a room temperature spectral noise current-density at 0V bias of the p-Si/DiMe-PTCDI photodiode is plotted (red line) in comparison with the one of a 10 k $\Omega$  resistor (green line). The mean square of the noise current-density of a resistor  $r$  is given by  $\langle i_n^2 \rangle / \Delta f = 4kT/r$  [129] and agrees with the measured data and hence supports the realistic value of  $D^*$ . At low frequencies a  $1/f$  noise is observed followed by a nearly flat (white) region up to the roll-off ( $f > 100$  kHz) of the I-V amplifier. The capacitance of the photodiode causes the slight decrease of the low roll-off frequency of the I-V amplifier compared to the pure resistive load. In the white noise region (3 kHz–30 kHz) we find a  $D^*$  value of  $\sim 7 \cdot 10^7$  Jones.

### 6.1.6.2 Response time measurements

In standard heterojunction photodiodes based on absorption in the bulk of one (or both) of the materials by means of band-to-band excitation followed by charge separation by an electric field in the depletion layer, the response time depends on diffusion of carriers generated outside the depletion layer, the drift time in the depletion layer and the capacitance of depletion layer [5]. In the case of our silicon–organic heterojunction, the absorption in the sub-bandgap range is assumed to take place at the interface and/or in the bulk of the organic material

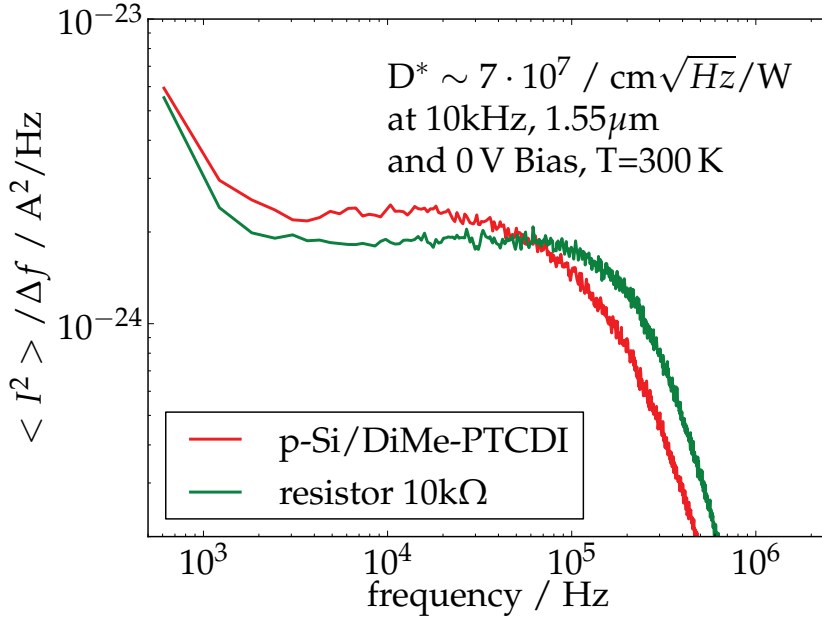


Figure 6.21: Double logarithmic presentation of the spectral noise density versus frequency at 0 V bias and 300 K of the DiMe-PTCDI/p-Si heterojunction (red) and of a 10 kΩ metal-film resistor (green).

due to promotion of electrons from localized to delocalized states. Therefore, the response time is limited by both the drift time through the organic material and by the capacitance of the device. The drift time can be roughly estimated from time-of-flight equation:  $\mu = \frac{d}{t \cdot E}$ , where  $\mu \simeq 0.5 \text{ cm}^2/\text{Vs}$  [21, 130] is the electron mobility,  $d \simeq 25 \text{ nm}$  is the organic layer thickness and  $E \simeq 6 \cdot 10^5 \text{ V/m}$  is the electric field in the device at 0V taken from the formula presented for PCBM in Eq. 4.4. The above estimation yields a drift time  $t \simeq 0.6 \text{ ns}$ . However, in the case of the studied devices with relatively large electrode area (on the order of  $0.1 \text{ cm}^{-2}$ ) and hence large capacitance, the dominant role seems to be the RC time constant [131]. The time resolved photoresponse was measured in the setup consisting of a laser diode emitting at  $1.55 \mu\text{m}$  controlled by a function generator, and beam splitter dividing the beam into the reference beam detected by a calibrated commercial InGaAs photodiode (green line in Fig. 6.22) and the probe beam detected by the heterojunction device under investigation (red line in Fig. 6.22). The sample output signal was additionally amplified. Both the amplifier and the function generator were chosen with care not to limit the response of time of the investigated photodetector. The rise and fall times obtained from Fig. 6.22 are in the range of 400 ns, resulting in the bandwidth of 2.5 MHz, what clearly shows the limiting role of capacitance. An important step in the improvement of the device bandwidth should therefore be a reduction of electrode area.

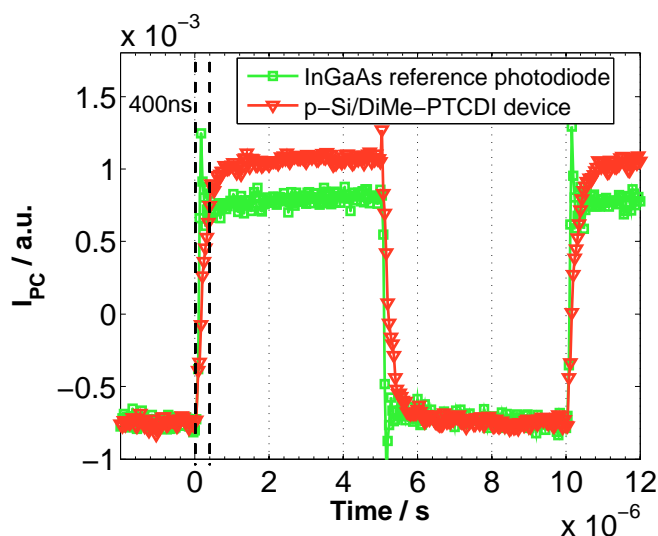


Figure 6.22: Time-resolved photocurrent of Al/p-Si/DiMe-PTCDI/Al diode at 0 V bias upon excitation by a pulsed laser diode emitting at  $1.55 \mu\text{m}$ , in comparison with response of reference InGaAs photodiode.

## 6.2 p-Si/Indigoids heterojunction diodes

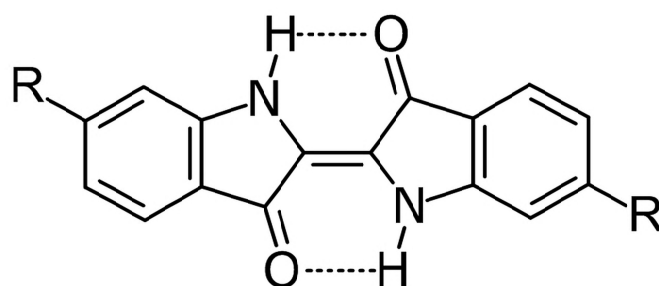
The molecular structure of both investigated Indigoids (Indigo and Tyrian Purple) is shown in Fig. 6.23. Both materials are naturally occurring and are today synthetically produced in the large scale by the dye industry for textile colouring, paints, cosmetics. As such, they are nonhazardous, environmentally friendly, low cost materials.

Indigo is an organic semiconductor of a natural origin, occurring in the plants *indigofera tinctoria* and *isatis tinctoria*. The history of colouring of textiles in different parts of the world (Egypt, China, India) dates back to ancient times. Since the end of 19<sup>th</sup> century Indigo is produced synthetically. The present production capacity reaches the amount of millions of tons per year, what is the highest number among dyes. The price on the order of few USD/kg places Indigo in an economically favorable position compared to other organic semiconductors used in modern organic electronics. An excellent degradation stability in the air is one of a key factors in industrial application of the dye [132].

Important for electronic application is the ambipolarity of Indigo, seen in OFETS, with electron and hole mobilities on the order of  $10^{-2} \text{ cm}^2/\text{Vs}$  [133]. The cyclic voltammetry experiment reported in [132] showed a reversible two-electron oxidation and reduction, illustrating the ambipolarity of transport properties. The high values of mobilities can also be elucidated by a strong  $\pi$ - $\pi$  stacking, manifested in the electronic and vibrational spectra of Indigo solutions [134–136]. The inter- and intramolecular hydrogen bonding, characteristic for the whole group of Indigoids, is responsible for the minimal solubility and a high melting point of  $390^\circ$  [133].

Tyrian purple (6,6'-dibromoindigo) was regarded as the most desirable dye of ancient times. It was in the centre of interest even before Indigo [137] and was produced from sea snails. The dye used in our studies has been prepared using known synthetic procedures [138] and purified twice by temperature gradient

sublimation. The heterojunctions were fabricated by evaporation from a hot-wall-epitaxy source at a rate of  $0.1 \text{ \AA/s}$  (see Section 3.1). The material exhibited ambipolar properties and in a standard OFET configuration showed mobilities more than an order of magnitude higher than Indigo, i.e.:  $\mu_e = 0.31 \text{ cm}^2/\text{Vs}$ ,  $\mu_h = 0.42 \text{ cm}^2/\text{Vs}$  [139].



R = H, Indigo

R = Br, 6,6'-dibromoindigo (Tyrian Purple)

Figure 6.23: Molecular structure of Indigo and Tyrian Purple.

Both Indigoids form a rectifying contact with p-Si with rectification ratio between  $-1 \text{ V}$  and  $+1 \text{ V}$  on the order of  $1.7 \cdot 10^3$  in case of Indigo (see Fig. 6.24) and  $3.7 \cdot 10^3$  in case of Tyrian Purple (see Fig. 6.25). Under illumination of a  $0.8 \text{ eV}$  laser diode, a photovoltaic effect was observed in both samples, resulting in short circuit current density  $J_{\text{SC}} = 0.1 \mu\text{A}/\text{cm}^2$  for Indigo (see Fig. 6.24) and  $J_{\text{SC}} = 2.4 \mu\text{A}/\text{cm}^2$  for Tyrian Purple (see Fig. 6.26). In both devices the observed open circuit voltage was around  $1 \text{ mV}$ . Fig. 6.26 reveals a forward bias photoconductivity in p-Si/Tyrian Purple device, with signal to noise ratio around 1.1. The origin of this effect remains unclear.

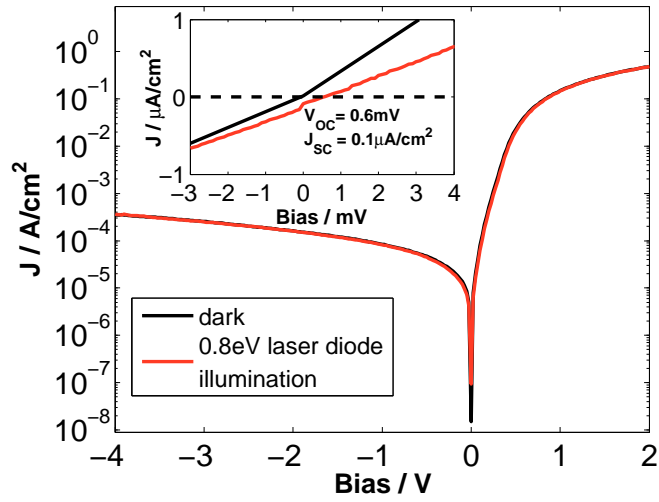


Figure 6.24: J-V characteristics of Al/p-Si/Indigo/Al heterojunction measured at 300K in the dark and under illumination of 0.8 eV laser diode. Inset: linear plot for low voltages showing the values of  $J_{SC}$  and  $V_{OC}$ .

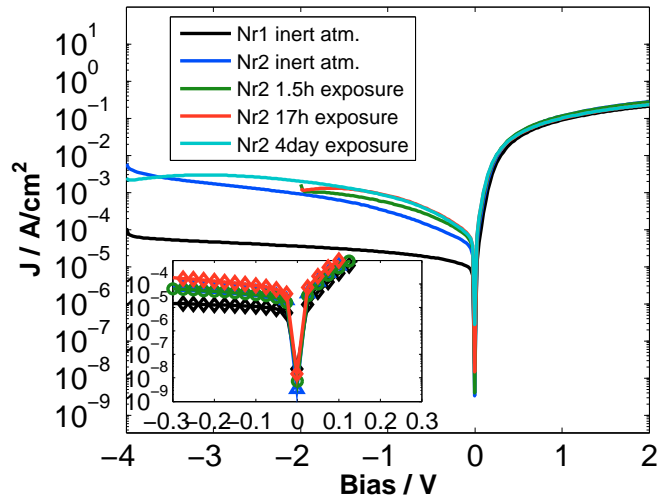


Figure 6.25: J-V characteristics of Al/p-Si/Tyrian Purple/Al device. Two samples were measured at 300K in dark in inert atmosphere. Sample Nr2 was additionally measured after exposure to air. Inset: J-V for low voltages.

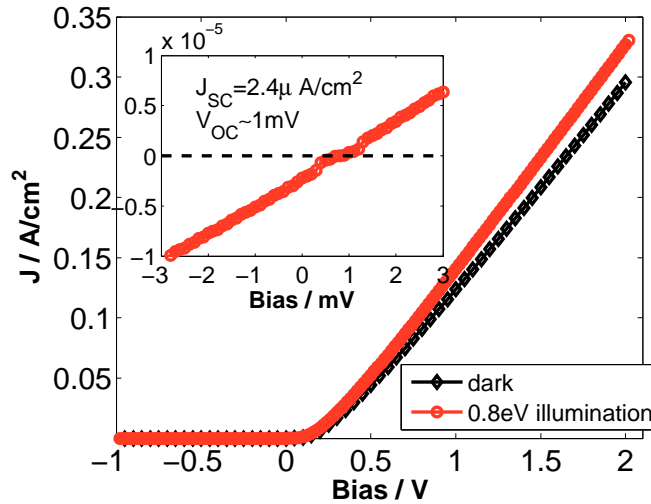


Figure 6.26: J-V characteristics of Al/p-Si/Tyrian Purple/Al device under 0.8 eV illumination and dark. The dark measurement was done with insufficient accuracy, which might lead to erroneous conclusions therefore only the forward bias is highlighted.

Fig. 6.27 shows temperature dependence of the dark reverse current for p-Si/Tyrian Purple heterojunction. The thermal activation energy is estimated to be  $E_a = 0.51 \pm 0.02$  eV.

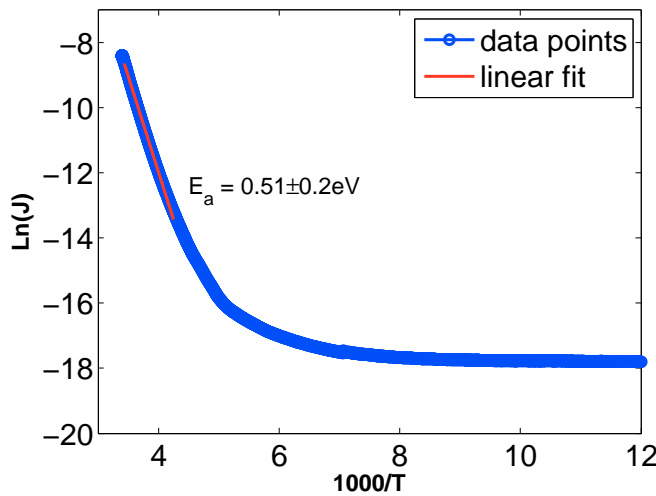


Figure 6.27: Arrhenius plot of dark current of Al/p-Si/Tyrian Purple/Al device measured at reverse bias -1.1 V.

Fig. 6.28 and Fig. 6.29 show the spectrally resolved photoresponse of both Indigoids diodes. The observed onset energy was  $0.54 \pm 0.03$  eV and  $0.48 \pm 0.03$  eV for Indigo and Tyrian Purple respectively. The observed value is again lower than the bandgap 1.7 eV of Indigo [133] and 1.8 eV of Tyrian Purple [140]. Important to notice is the fact that the Tyrian Purple exhibited a photoresponsivity similarly to perylene diimide device on the order of  $10^{-5}$  A/W, and the photoresponse of the device was stable in air with the slight deterioration of the diode itself (see Fig. 6.25).



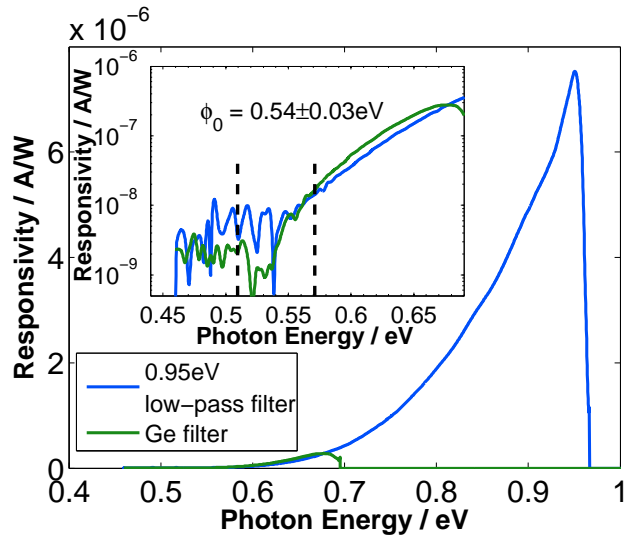


Figure 6.28: Responsivity spectra of Al/p-Si/Indigo/Al device. Measured at 300K, behind 0.95 eV band-pass filter and Ge filter. Inset: Semi-logarithmic plot, uncertainty of onset energy estimation is shown.

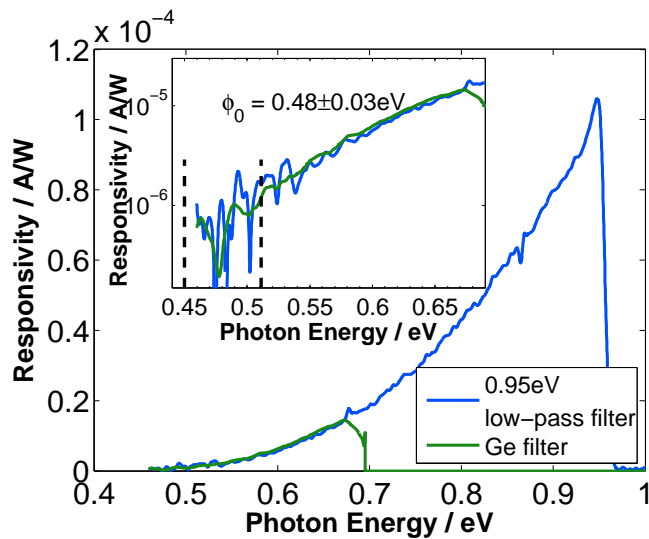


Figure 6.29: Responsivity spectra of Al/p-Si/Tyrian Purple/Al device. Measured at 300K, behind 0.95 eV band-pass filter and Ge filter. Inset: Semi-logarithmic plot, uncertainty of onset energy estimation is shown.

# Chapter 7

## Comparison of all studied heterojunctions, general conclusions

Table 7.1 summarizes the measurements results of all types of devices studied in this thesis. The comparison of responsivity is shown in Fig. 7.1. From the detector performance point of view the superior devices were those with DiMe-PTCDI and Tyrian Purple. However, the mechanisms of diodes operation remain ambiguous. The detailed study performed on PCBM diodes allowed to estimate the barrier height from C-V measurement and to apply a generation-recombination model for the diode operation. Due to the lack of detailed comprehensive studies, a direct application of the same model for other devices was not possible within this thesis.

Even for relatively well studied fullerene devices, the origin of dark reverse current and photocurrent remains ambiguous, with pros and cons of proposed models described in Section 4.2. The electrical studies, photocurrent onset and dark current activation energy results of all studied devices lead to the following conclusions:

- Assuming for all devices interface photogeneration of a charge carrier from the silicon VB into LUMO of the organic material as the mechanism of photoresponse in IR, we could conclude that the slightly different values of PC onset correspond to different band alignment at the interface (see black squares with error bars in Fig. 7.3). However, for the studied materials other than PCBM, a C-V analysis should be performed in order to estimate the built-in field and consequently the barrier height. For this purpose diodes with good rectification and no hysteresis in the C-V characteristics are required.

In this scenario, the dark reverse current should be treated as resulting from the generation in the space charge region of silicon. In agreement with this interpretation, the obtained results for the dark reverse current activation energy ( $\simeq 0.5$  eV) i.e. all similar to half of the silicon bandgap (see red circles with error bars in Fig. 7.3) within the measurement uncertainties. The drawback of this approach for the studied devices with organic layers other than fullerenes is the observed one order of magnitude higher current density than for the PCBM devices (see Fig. 7.2). The comparison of the measured values with the theoretical curve for the generation-recombination process in the Si depletion region results in effective life

times of charge carriers one order of magnitude lower than reported in literature [89]. Moreover, a slight deviation from the predicted square root voltage dependence of the reverse current is observed. However, due to the lack of knowledge of the built-in potential and the exact energy level values at the interface from reliable C-V studies a detailed analysis was not performed.

- Table 7.2 summarizes the LUMO levels measured electrochemically for all pristine materials studied in hybrid diodes. Assuming that the difference between the Si VB ( $E_V^{Si}$ ) and the LUMO of the organic materials ( $E_{LUMO}$ ) corresponds to the barrier height and is manifested in the photocurrent onset ( $E_{PC}$ ), a linear relation for all studied materials is expected:  $E_{PC} = E_{LUMO} - E_V^{Si}$ . Fig. 7.4 reveals that the expected linear dependence is not matched and specially a huge deviation is seen in the case of Indigoids and [84]PCBM. Since the exact absolute value of LUMO levels is not known, it can only be concluded, basing on barrier height estimated from C-V measurement for PCBM and comparison of relative LUMO levels, that for all materials the LUMO level is situated above the Fermi level of the p-type silicon substrate used in this work (-4.8 V) [82]. Moreover, it is clear that the band alignment at the interface is not determined by a value of difference between work function of Si and electron affinity in organic material, i.e. for all studied materials the Schottky-Mott limit does not define the barrier height. As reported in literature for various interfaces (organic semiconductor/metal [86], organic semiconductor–organic semiconductor [87], organic semiconductor–insulator [111] or organic semiconductor–inorganic semiconductor [114, 141]) the band alignment is defined by dipoles formed at the interface. A more detailed interface analysis with photoemission and inverse photoemission method should be performed in order to identify the relative position of respective bands at the hybrid interfaces studied in this work.
- The measurement of a spectrally resolved photoresponse at short circuit condition, for determining the onset energy is not sufficient to identify the phototransition of electron as either direct i.e. from the VB of p-Si to the LUMO of the organic material, or via an intermediate step i.e. a localized state in the organic material at the interface, referred to as pseudo-IPE (see Fig. 4.30).
- Assuming for all devices deep trap photogeneration in the organic layer as the PC mechanism, we could assign the different values of the PC onsets to different energetical positions of localized levels in the organic layer. The presence of such localized states at energies  $\simeq 0.5$  eV below LUMO, either interface or bulk, has not been reported except for the case of  $C_{60}$  (see Chapter 5). The presence of localized polaron  $C_{60}^-$  was predicted theoretically [97, 98] and reported experimentally [99]. Moreover it was also seen in the photoconductivity of  $C_{60}$  OFET presented in this work.
- The deep trap photogeneration could be responsible for the observed photoconductivity under forward bias in p-Si/DiMe-PTCDI and p-Si/Tyrian Purple devices shown in Fig. 6.11 and Fig. 6.26 respectively.

- An open question remains whether the possible presence of deep trap states responsible for photoresponse implies their participation in the proposed reverse current mechanism via hopping transport through localized states. Such an explanation could be endorsed if we, assume (based on Fig. 7.3) the correspondence of PC onset and activation energy for each material. However, a deep trap states with high enough density forming a band throughout the bulk of the material were up to now not reported in literature.
- Important to notice is the observed hysteresis in perylene device which might suggest the presence of an interface dipole that might be responsible for a superior responsivity through increase of local electric field.

To conclude, further detailed studies are required in order to analyze the origin of photocurrent in devices based on DiMe-PTCDI and Indigoids. Nevertheless their superior quality makes them an interesting and relatively easy (due to high signal-to-noise ratio in photoelectrical experiments) object to study.

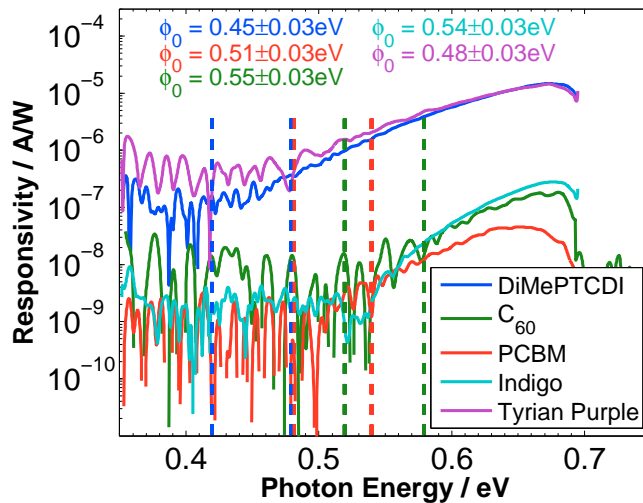


Figure 7.1: Comparison of responsivity spectra of all studied types of devices. Measured at 300 K, behind germanium filter. Onset uncertainty for each case is shown. Different noise level for each sample stems from the fact that during the measurement we tried to achieve a similar level of signal at the lock-in amplifier with different sensitivity for each sample corresponding to the value of measured photocurrent

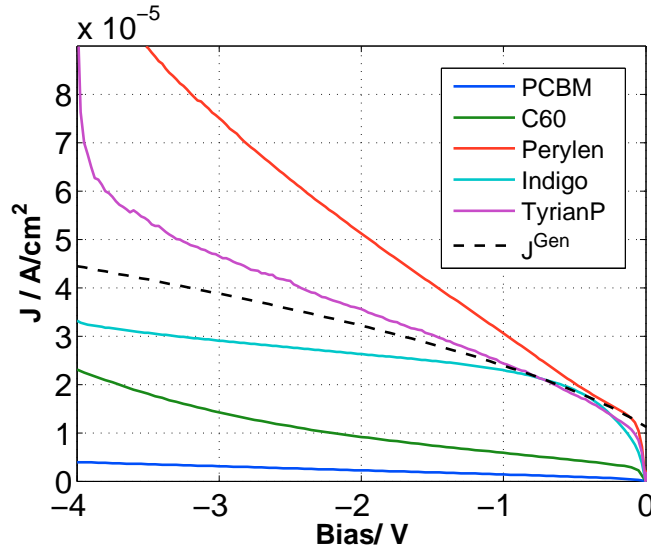


Figure 7.2: Comparison of reverse bias J-V characteristics of all studied types of devices. Measured at 300 K. Dotted line shows a results of modeling with depletion layer generation formula (Eq. 4.58) for p-Si/DiMe-PTCDI device, assuming effective life time of thermally generated minority carriers  $\tau_e = 9$  ns, and  $qV_{bi} = PC_{\text{onset}} - E_{FV} = 0.2$  eV.

Table 7.1: Comparison of responsivity measured at photon energy 0.8 eV and 300 K, photocurrent onset energy, activation energy and barrier height obtained from C-V measurement (if measured) for all studied devices Al/p-Si/organic layer/Al.

Organic layer	Thickness	Responsivity A/W	PC Onset at 300 K / eV	$E_{\text{activation}}$ eV	$\Phi_B$ from CV eV
DiMe-PTCDI	25 nm	6.9E-05	0.45±0.03	0.47±0.02	
Tyrian Purple	30 nm	4.3E-05	0.48±0.03	0.51±0.02	
C <sub>60</sub>	25 nm	7.4E-06	0.55±0.03	0.51±0.02	
Indigo	50 nm	1.9E-06	0.54±0.03		
PCBM	165 nm	1.4E-06	0.51±0.03	0.54±0.02	0.6±0.05

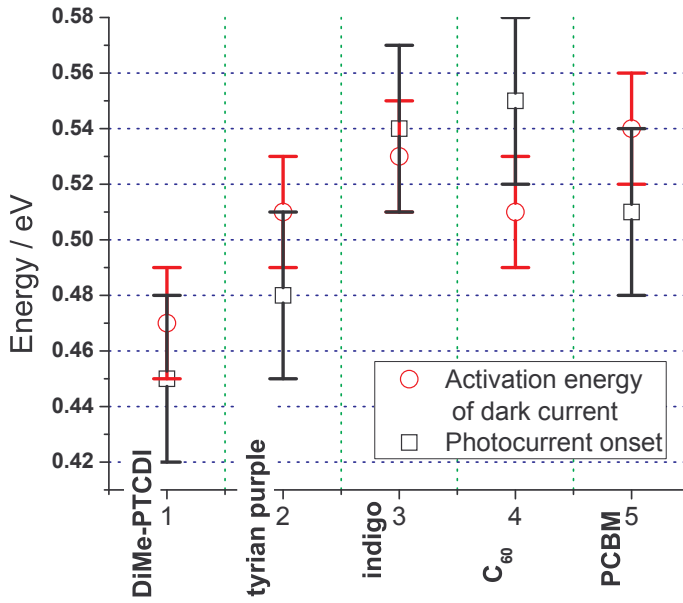


Figure 7.3: Comparison of photocurrent onset energy and dark current activation energy for all studied Al/p-Si/organic layer/Al devices.

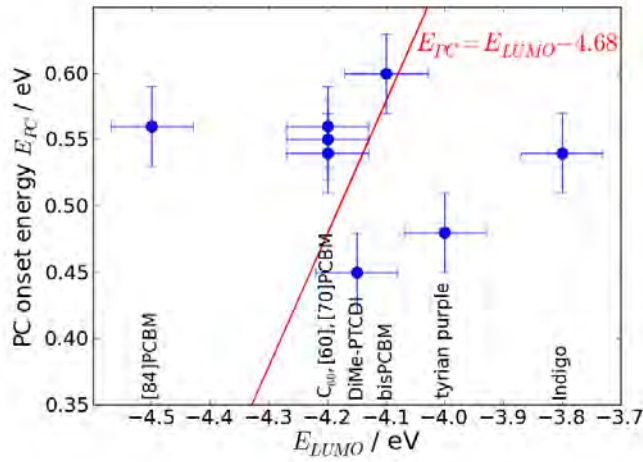


Figure 7.4: Values of PC onset of different devices presented as a function of LUMO levels of different materials. The red line represents the hypothetical linear dependence  $E_{PC} = E_{LUMO} - E_V^{Si}$ , where  $E_V^{Si}$  was used as a fitting parameter and the value -4.68 eV results from a least-square fit.

Table 7.2: Comparison of photocurrent onset energy, reverse current activation energy for all studied devices Al/p-Si/organic layer/Al and energy of LUMO level for all studied materials. The LUMO values for [60]PCBM, DiMe-PTCDI, Tyrian Purple and Indigo were obtained electrochemically using the same setup and the same reference electrode. The values for [70]PCBM and C<sub>60</sub> were assumed equal to [60]PCBM following reported observations [83], similarly the value for bisPCBM was assumed 100 meV higher than for [60]PCBM [100] and for [84]PCBM was assumed around 350 meV lower than for [60]PCBM [101].

Organic layer	PC Onset eV	E <sub>activation</sub> eV	E <sub>LUMO</sub> eV
[60]PCBM	0.56±0.03	0.54±0.02	-4.2
[70]PCBM	0.54±0.03		-4.2
bisPCBM	0.6±0.03		-4.1
[84]PCBM	0.56±0.03		-4.5
C <sub>60</sub>	0.55±0.03	0.51±0.02	-4.2
DiMe-PTCDI	0.45±0.03	0.47±0.02	-4.15
Tyrian Purple	0.48±0.03	0.51±0.02	-4 [140]
Indigo	0.54±0.03		-3.8 [133]

# Chapter 8

## Summary and outlook

In summary this work demonstrated that an inorganic-organic heterojunction diodes can be utilized for sensing NIR light (specifically at  $1.55\mu\text{m}$ ). A photovoltaic effect is observed up to a wavelength of  $2.7\mu\text{m}$  and it is argued that it originates from an optical excitation of electrons from the Si valence band into the LUMO level of an organic material, with possible intermediate step i.e. an occupied localized states in the organic thin film with a subsequent charge-carrier separation at the heterointerface. A novel comprehensive model for the operation of p-Si/PCBM hybrid diode, based on an interface generation-recombination current, was proposed. The band diagram based on energy values obtained experimentally from C-V measurement was presented. Based on the detailed understanding of the diode operation principle, further improvements of the device with respect to its application as infrared photodetector compatible with standard Si technology [142] as well as the development of photodetectors based on alternative organic semiconductors becomes possible. The simple fabrication, operation at room-temperature, compatibility with the CMOS process together with the responsivity, specific detectivity and response time reported here demonstrate a high potential of this IR detector concept.

In order to increase the performance of the device further, basic physical studies of existing detectors and organic materials are planned. These experiments will be aiming at comprehensive understanding of physical processes governing the light absorption in sub-bandgap range responsible for photodetector operation. The experiments planned within future project will feature:

- studies of the influence of different Si doping concentrations on the photocurrent onset, in order to identify whether the onset is independent of the doping concentration in Si and whether the photoexcitation process can be described as pseudo-IPE process
- probing of density and energy position of localized states at the interface and/or in the bulk of the organic material with electrical transient methods, photoemission spectroscopy (in situ UPS studies) and photoinduced absorption
- investigation of OFETs fabricated from different materials, in order to study the possible excitation of polaron states generated in the transistor channel as a result of increasing gate bias



- spectral analysis of the photoconductivity observed in pSi/DiMe-PTCDI and pSi/Tyrian Purple diodes under forward bias, to measure the onset energy of PC and compare with short circuit PC
- further detailed analysis of hysteresis observed in C-V experiments on pSi/DiMe-PTCDI diodes with transient electrical methods
- detailed analysis of pSi/Indigo, pSi/Tyrian Purple diodes: C-V investigation of possible existence of hysteresis observed for DiMe-PTCDI, J-V, SEM
- optimization of response time of the detector by reduction of active electrode area, thus reduction of RC limitation of the bandwidth
- analysis of n-Si/Indigo, n-Si/Tyrian Purple diodes with respect to their ambipolarity seen in OFETs [133, 140]
- analysis of n-Si/p-organic material (a p-type material of choice, quinacridone)
- studies of the influence of the doping level of the organic material on the operation of a photodiode

In his review from 2003 [35] Forrest asked for an application niche for such a device concept where its advantages over conventional or even all-organic devices, such as low environmental and energetic cost of fabrication and integration with Si integrated circuits, room temperature operation and low power consumption (short circuit operation), would be shown. The use of such a structure for IR detection could indeed be one.

# Appendix A

## Cavity analysis

In this Section, a theoretical analysis of light intensity distribution in a multilayer structure is presented. Table A.1 presents schematically the investigated Al/p-Si/organic/Al multilayer structure with the values of material properties and variables used in the optical analysis. The back Al contact is omitted as it does not lay in the optical path, the Si substrate layer is considered as semi-infinite due to its huge thickness ( $250\mu\text{m}$ ) compared to the wavelength ( $1\text{-}3\mu\text{m}$ ).

Table A.1: Investigated multilayer structure.  $A'_n$  and  $B'_n$  are the respective amplitudes of plane waves in medium  $n$  at  $x = x_{n-1}$   $A_n$  and  $B_n$  are the respective amplitudes of plane waves in medium  $n$  at  $x = x_n$ . The reported values of refractive indexes are for a photon energy  $0.8\text{ eV}$ .

Si	SiO <sub>2</sub>		organic		Al		vac.
$n_0$	$n_1$		$n_2$		$n_3 = n_3^R - ik_3$		$n_4$
3.4 [143]	1.44 [144]		1.85 [145]		1.44- $i$ 16 [144]		1
$A_0$	$A'_1$	$A_1$	$A'_2$	$A_2$	$A'_3$	$A_3$	$A'_4$
$B_0$	$B'_1$	$B_1$	$B'_2$	$B_2$	$B'_3$	$B_3$	$B'_4$
$x_0$	$x_1$		$x_2$		$x_3$		
	$d_1$		$d_2$		$d_3$		

To analyze the theoretical distribution of light intensity in the investigated structures we will apply the matrix formulation for multilayer system presented in a textbook by Yeh [146]. The  $xy$  plane is considered as the plane of incidence and the whole medium is homogenous in the  $y$ -direction. The electric field of a plane-wave solution of the wave equation can be written as:

$$\vec{E} = \vec{E}(x)e^{i(\omega t - k_y y)} \quad (\text{A.1})$$

where the  $x$ -direction is perpendicular to the interfaces. For any value of  $y = y_0$ , the electric field distribution  $\vec{E}(x)$  consists of right-traveling wave ( $A(x)$ ) and left-traveling wave ( $B(x)$ ) and for the given multilayer structure is:

$$E_y(x) = \begin{cases} A_0 e^{-ik_0 x(x-x_0)} + B_0 e^{ik_0 x(x-x_0)}, & x < x_0 \\ A_1 e^{-ik_1 x(x-x_1)} + B_1 e^{ik_1 x(x-x_1)}, & x_0 < x < x_1 \\ A_2 e^{-ik_2 x(x-x_2)} + B_2 e^{ik_2 x(x-x_2)}, & x_1 < x < x_2 \\ A_3 e^{-ik_3 x(x-x_3)} + B_3 e^{ik_3 x(x-x_3)}, & x_2 < x < x_3 \\ A'_4 e^{-ik_4 x(x-x_3)} + B'_4 e^{ik_4 x(x-x_3)}, & x > x_3 \end{cases} \quad (\text{A.2})$$

where we have assumed that the electric field vector is polarized perpendicular to the plane of incidence (s-polarization). For p-polarization (the magnetic field vector  $\vec{H}$  perpendicular to the plane of incidence) similar ansatz has to be made for the corresponding component of magnetic field vector  $H_y(x)$ .

In Eq. A.2  $k_{nx}$  are respective  $x$  components of the wave vectors:

$$k_{nx} = \left[ \left( \frac{n_n \omega}{c} \right)^2 - k_y^2 \right]^{1/2} = \left( \frac{\omega}{c} \right) n_n \cos \theta_n = \frac{2\pi}{\lambda} n_n \cos \theta_n \quad (\text{A.3})$$

where  $\theta_n$  is the angle of incidence, (normal incidence  $\theta_n = 0$ ). The  $y$  components of the wave vectors must have the same value in all the layers in order to satisfy the boundary conditions at the interfaces.

Imposing the boundary conditions of Maxwell equation i.e. the continuity of tangential components of the electric field vector  $\vec{E}$  and magnetic field vector  $\vec{H}$  at the interface between two media leads to a set of linear equations describing the system. Those equations can be presented using the matrix formulation, what for the given structure leads to:

$$\begin{pmatrix} A_0 \\ B_0 \end{pmatrix} = \begin{pmatrix} M_{11} & M_{12} \\ M_{21} & M_{22} \end{pmatrix} \begin{pmatrix} A'_4 \\ B'_4 \end{pmatrix} \quad (\text{A.4})$$

with the matrix  $M$  given by:

$$\begin{pmatrix} M_{11} & M_{12} \\ M_{21} & M_{22} \end{pmatrix} = D_0^{-1} \left[ \prod_{n=1}^3 D_n P_n D_n^{-1} \right] D_4 \quad (\text{A.5})$$

The matrices  $D_n$  are so-called dynamical matrices of the medium  $n$  stemming from boundary conditions of Maxwell equations and can be written as:

$$D_n = \begin{pmatrix} 1 & 1 \\ n_n \cos \theta_n & -n_n \cos \theta_n \end{pmatrix} \text{ for s polarized waves} \quad (\text{A.6})$$

$$D_n = \begin{pmatrix} \cos \theta_n & \cos \theta_n \\ n_n & -n_n \end{pmatrix} \text{ for p polarized waves} \quad (\text{A.7})$$

and  $P_n$  is the so-called propagation matrix, which accounts for propagation through the bulk of the layer:

$$P_n = \begin{pmatrix} e^{i\phi_n} & 0 \\ 0 & e^{-i\phi_n} \end{pmatrix} \quad (\text{A.8})$$

where  $\phi_n$  is given by:  $\phi_n = k_{nx} d_n$  Using the matrix equation A.4 we can obtain the general reflection coefficient for the plane wave that is incident from medium 0 (silicon):

$$r = \left( \frac{B_0}{A_0} \right)_{B'_4=0} = \left( \frac{M_{21}}{M_{11}} \right) \quad (\text{A.9})$$

Similarly to Eq. A.4 we can formulate the relation between amplitudes in media 0 and 1:

$$\begin{pmatrix} A_0 \\ B_0 \end{pmatrix} = D_0^{-1} D_1 \begin{pmatrix} A'_1 \\ B'_1 \end{pmatrix} = D \begin{pmatrix} A'_1 \\ B'_1 \end{pmatrix} = \begin{pmatrix} D_{11} & D_{12} \\ D_{21} & D_{22} \end{pmatrix} \begin{pmatrix} A'_1 \\ B'_1 \end{pmatrix} \quad (\text{A.10})$$

and

$$\begin{pmatrix} A'_1 \\ B'_1 \end{pmatrix} = P_1 \begin{pmatrix} A_1 \\ B_1 \end{pmatrix} = \begin{pmatrix} e^{i\phi_1} & 0 \\ 0 & e^{-i\phi_1} \end{pmatrix} \begin{pmatrix} A_1 \\ B_1 \end{pmatrix} \quad (\text{A.11})$$

what using the expression for  $r$  gives:

$$r = \frac{B_0}{A_0} = \frac{D_{21}A'_1 + D_{22}B'_1}{D_{11}A'_1 + D_{12}B'_1} \quad (\text{A.12})$$

finally  $A'_1$ :

$$A'_1 = B'_1 \frac{D_{22} - rD_{12}}{rD_{11} - D_{21}} = B'_1 \Delta^{-1} \quad (\text{A.13})$$

and  $A_1$  and  $B_1$  are:

$$A_1 = e^{-i\phi_1} A'_1 \quad (\text{A.14a})$$

$$B_1 = e^{i\phi_1} B'_1 \quad (\text{A.14b})$$

Using Eq. A.10, Eq. A.13 and Eq. A.14 we can express  $A_1$  and  $B_1$  as  $A_0$ :

$$A_0 = D_{11}A'_1 + D_{12}B'_1 = D_{11}A'_1 + D_{12}A'_1 \Delta \quad (\text{A.15})$$

$$A'_1 = \frac{A_0}{D_{11} + D_{12}\Delta} \quad (\text{A.16})$$

$$A_1 = e^{-i\phi_1} \frac{A_0}{D_{11} + D_{12}\Delta} \quad (\text{A.17a})$$

$$B_1 = e^{i\phi_1} \frac{A_0 \Delta}{D_{11} + D_{12}\Delta} \quad (\text{A.17b})$$

we can now formulate the expression for electric field of the plane wave in the organic layer:

$$E(x) = A_1 e^{-ik_{1x}(x-d_1)} + B_1 e^{ik_{1x}(x-d_1)} = \frac{A_0}{D_{11} + D_{12}\Delta} \left( e^{-i\phi_1} e^{-ik_{1x}(x-d_1)} + \Delta e^{i\phi_1} e^{ik_{1x}(x-d_1)} \right) \quad (\text{A.18})$$

Finally the time averaged light intensity as a function of photon energy, organic layer thickness and the position in the organic layer can be obtained from:

$$I \propto E \cdot E^* \quad (\text{A.19})$$

where  $*$  denotes the conjugation. To study the influence of organic layer thickness on the intensity of light that is absorbed and induce photocurrent, assuming that the absorption takes place at the interface we calculate Eq. A.19 as a function of organic layer thickness for  $x = 0$  and for a given photon energy. On the other hand assuming the bulk absorption we can calculate the total absorbed light intensity (for a given photon energy) in the whole bulk of organic layer depending on thickness:

$$I_{absorbed}^{h\nu_1}(d_1) = \int_{x=0}^{x=d_1} I^{h\nu_1}(d_1, x) dx \quad (\text{A.20})$$

## Appendix B

# Analysis of applicability of Schottky model

In this section we will analyze the applicability of Schottky metal–semiconductor model regarding the studied devices p-Si/organic layer/metal. The ideal J-V characteristics of a Schottky diode can be expressed as [5, 147]:

$$J = J_0 (\exp(eV/k_B T) - 1) \quad (\text{B.1})$$

where  $J_0$  i.e. the saturation current density can be given by:

$$J_0 = A^* T^2 \exp(-e\Phi/k_B T) \quad (\text{B.2})$$

where  $A^*$  is the effective Richardson constant and  $\Phi$  is the barrier height at the metal–semiconductor interface.

Fig. B.1 and Fig. B.2 show the Richardson plot in  $1/T$  vs  $\ln J/T^2$  coordinates [148] at 1 V reverse bias for respectively p-Si/PCBM/AL and p-Si/DiMe-PTCDI/Al junctions. The linear fit yields from the intersection with y-axis  $A_{PCBM}^* = 6 \cdot 10^{-3} \text{ A/cm}^2\text{K}^2$  and  $A_{DiMe-PTCDI}^* = 17 \cdot 10^{-3} \text{ A/cm}^2\text{K}^2$  and from the slope the barrier height of  $\Phi_{PCBM} = 0.5 \text{ eV}$  and  $\Phi_{DiMe-PTCDI} = 0.44 \text{ eV}$ . The obtained values of barrier height for both materials match within measurement uncertainties the photo current onset energy that is believed to be defined by band discontinuities at the interface. The value for PCBM is a bit smaller than the barrier height obtained from C-V  $\Phi_{B(C-V)} = 0.6 \pm 0.05 \text{ eV}$ . However, the values of Richardson constant for both devices are several orders of magnitude smaller than the typical value of the Richardson constant for a p-Si/Al Schottky diode:  $A^* = 32 \text{ A/cm}^2\text{K}^2$  [5, 149]. From this simple analysis it is concluded, that thermionic emission is not the dominant mechanism describing the (actually much lower) measured saturation current density.

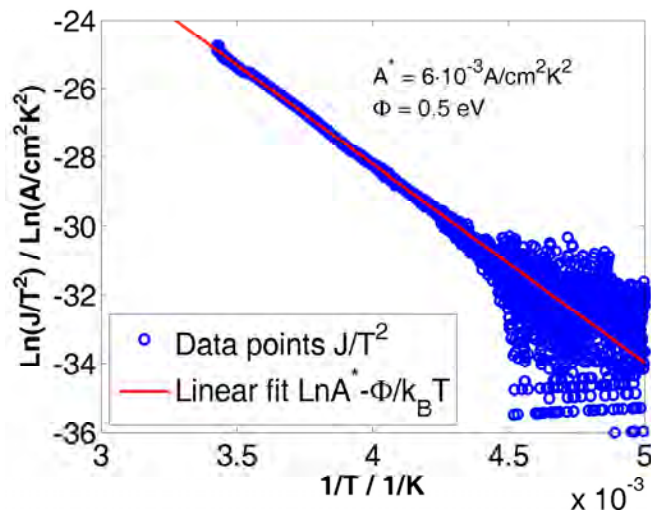


Figure B.1: Richardson plot at 1 V reverse bias for Al/p-Si/PCBM/Al heterojunction.

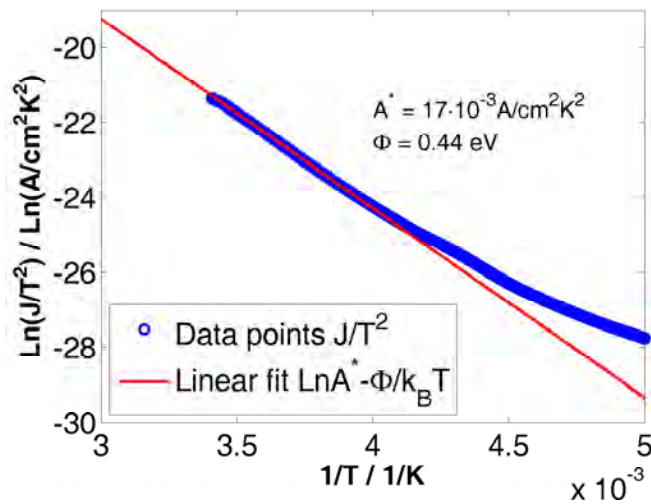


Figure B.2: Richardson plot at 1 V reverse bias for Al/p-Si/DiMe-PTCDI/Al heterojunction.

# Bibliography

- [1] C. K. Chiang, C. R. Fincher, Y. W. Park, A. J. Heeger, H. Shirakawa, E. J. Louis, S. C. Gau, and A. G. MacDiarmid, "Electrical Conductivity in Doped Polyacetylene," *Phys. Rev. Lett.*, vol. 39, pp. 1098–1101, Oct. 1977.
- [2] H. Shirakawa, E. J. Louis, A. G. MacDiarmid, C. K. Chiang, and A. J. Heeger, "Synthesis of electrically conducting organic polymers: halogen derivatives of polyacetylene, (CH)," *J. Chem. Soc.*, no. 16, pp. 578–580, 1977.
- [3] M. A. Green, K. Emery, Y. Hishikawa, W. Warta, and E. D. Dunlop, "Solar cell efficiency tables (version 40)," *Progress in Photovoltaics: Research and Applications*, vol. 20, no. 5, pp. 606–614, 2012.
- [4] A. L. Roes, E. A. Alsema, K. Blok, and M. K. Patel, "Ex-ante environmental and economic evaluation of polymer photovoltaics," *Progress in Photovoltaics: Research and Applications*, vol. 17, no. 6, pp. 372–393, 2009.
- [5] S. M. Sze and K. K. Ng, *Physics of semiconductor devices*. Wiley-Interscience publication, Wiley-Interscience, 2007.
- [6] G. J. Matt, T. Fromherz, M. Bednorz, S. Zamiri, G. Goncalves, C. Lungenschmied, D. Meissner, H. Sitter, N. S. Sariciftci, C. J. Brabec, and G. Bauer, "Fullerene sensitized silicon for near- to mid-infrared light detection.," *Advanced Materials*, vol. 22, pp. 647–650, Feb. 2010.
- [7] P. Stallinga, *Electrical Characterization of Organic Electronic Materials and Devices*. Chichester UK: Wiley, 2009.
- [8] J. L. Bredas and G. B. Street, "Polarons, bipolarons, and solitons in conducting polymers," *Accounts of Chemical Research*, vol. 18, no. 10, pp. 309–315, 1985.
- [9] N. F. Mott, "Conduction in glasses containing transition metal ions," *Journal of Non-Crystalline Solids*, vol. 1, no. 1, pp. 1–17, 1968.
- [10] B. I. Shklovski, "Hopping conduction in lightly doped semiconductors," *Soviet Physics Semiconductors - USSR*, vol. 6, no. 7, pp. 1053–1075, 1973.
- [11] A. Aharony, Y. Zhang, and M. P. Sarachik, "Universal crossover in variable range hopping with Coulomb interactions," *Phys. Rev. Lett.*, vol. 68, pp. 3900–3903, June 1992.

- [12] H. Bäessler, "Charge Transport in Disordered Organic Photoconductors a Monte Carlo Simulation Study," *physica status solidi (b)*, vol. 175, no. 1, pp. 15–56, 1993.
- [13] A. I. Gubanov, *Quantum electron theory of amorphous conductors*. New York: New York, Consultants Bureau, english tr ed., 1965.
- [14] G. Caserta, B. Rispoli, and A. Serra, "Space-Charge-Limited Current and Band Structure in Amorphous Organic Films," *physica status solidi (b)*, vol. 35, no. 1, pp. 237–248, 1969.
- [15] G. H. Heilmeyer and S. E. Harrison, "Charge Transport in Copper Phthalocyanine Single Crystals," *Phys. Rev.*, vol. 132, pp. 2010–2016, Dec. 1963.
- [16] E. Orti, J. L. Brédas, and C. Clarisse, "Electronic structure of phthalocyanines: Theoretical investigation of the optical properties of phthalocyanine monomers, dimers, and crystals," *The Journal of Chemical Physics*, vol. 92, no. 2, p. 1228, 1990.
- [17] J. P. Meyer, D. Schlettwein, D. Wöhrle, and N. I. Jaeger, "Charge transport in thin films of molecular semiconductors as investigated by measurements of thermoelectric power and electrical conductivity," *Thin Solid Films*, vol. 258, no. 1–2, pp. 317–324, 1995.
- [18] P. Stallinga, "Electronic Transport in Organic Materials: Comparison of Band Theory with Percolation/(Variable Range) Hopping Theory.," *Advanced Materials*, pp. 3356–3362, June 2011.
- [19] G. Horowitz, R. Hajlaoui, and P. Delannoy, "Temperature Dependence of the Field-Effect Mobility of Sexithiophene. Determination of the Density of Traps," *J. Phys. III France*, vol. 5, no. 4, pp. 355–371, 1995.
- [20] G. Horowitz, M. E. Hajlaoui, and R. Hajlaoui, "Temperature and gate voltage dependence of hole mobility in polycrystalline oligothiophene thin film transistors," *Journal of Applied Physics*, vol. 87, no. 9, pp. 4456–4463, 2000.
- [21] R. J. Chesterfield, J. C. McKeen, C. R. Newman, P. C. Ewbank, D. A. da Silva Filho, J.-L. Brédas, L. L. Miller, K. R. Mann, and C. D. Frisbie, "Organic Thin Film Transistors Based on N-Alkyl Perylene Diimides: Charge Transport Kinetics as a Function of Gate Voltage and Temperature," *The Journal of Physical Chemistry B*, vol. 108, no. 50, pp. 19281–19292, 2004.
- [22] H. A. Albuquerque, A. G. de Oliveira, G. M. Ribeiro, R. L. da Silva, W. N. Rodrigues, and R. M. Rubinger, "Reduction of variable range hopping conduction in low-temperature molecular-beam epitaxy GaAs," *Journal of Applied Physics*, vol. 95, no. 7, pp. 3553–3556, 2004.
- [23] D. C. Look, D. C. Walters, M. O. Manasreh, J. R. Sizelove, C. E. Stutz, and K. R. Evans, "Anomalous Hall-effect results in low-temperature molecular-beam-epitaxial GaAs: Hopping in a dense EL2-like band," *Phys. Rev. B*, vol. 42, pp. 3578–3581, Aug. 1990.



- [24] S. N. Mott, "Electrons in glass," *Rev. Mod. Phys.*, vol. 50, pp. 203–208, Apr. 1978.
- [25] B. Mishori, E. A. Katz, D. Faiman, and Y. Shapira, "Studies of electron structure of C<sub>60</sub> thin films by surface photovoltage spectroscopy," *Solid State Communications*, vol. 102, no. 6, pp. 489–492, 1997.
- [26] H. Grussbach and M. Schreiber, "Determination of the mobility edge in the Anderson model of localization in three dimensions by multifractal analysis," *Phys. Rev. B*, vol. 51, pp. 663–666, Jan. 1995.
- [27] N. F. Mott, "Electrons in disordered structures," *Advances in Physics*, vol. 16, no. 61, pp. 49–144, 1967.
- [28] M. Cutler and N. F. Mott, "Observation of Anderson Localization in an Electron Gas," *Phys. Rev.*, vol. 181, pp. 1336–1340, May 1969.
- [29] S. R. Forrest, M. L. Kaplan, P. H. Schmidt, W. L. Feldmann, and E. Yanowski, "Organic-on-inorganic semiconductor contact barrier devices," *Applied Physics Letters*, vol. 41, no. 1, pp. 90–93, 1982.
- [30] S. R. Forrest, M. L. Kaplan, P. H. Schmidt, and J. V. Gates, "Evaluation of III-V semiconductor wafers using nondestructive organic-on-inorganic contact barriers," *Journal of Applied Physics*, vol. 57, no. 8, pp. 2892–2895, 1985.
- [31] S. R. Forrest, M. L. Kaplan, and P. H. Schmidt, "Semiconductor analysis using organic-on-inorganic contact barriers. II. Application to InP-based compound semiconductors," *Journal of Applied Physics*, vol. 60, no. 7, pp. 2406–2418, 1986.
- [32] J. R. Ostrick, A. Dodabalapur, L. Torsi, A. J. Lovinger, E. W. Kwock, T. M. Miller, M. Galvin, M. Berggren, and H. E. Katz, "Conductivity-type anisotropy in molecular solids," *Journal of Applied Physics*, vol. 81, no. 10, pp. 6804–6808, 1997.
- [33] P. Peumans, A. Yakimov, and S. R. Forrest, "Small molecular weight organic thin-film photodetectors and solar cells," *Journal of Applied Physics*, vol. 93, no. 7, pp. 3693–3723, 2003.
- [34] C. W. Tang, "Two-layer organic photovoltaic cell," *Applied Physics Letters*, vol. 48, no. 2, p. 183, 1986.
- [35] S. R. Forrest, "Organic-inorganic semiconductor devices and 3, 4, 9, 10 perylenetetracarboxylic dianhydride: an early history of organic electronics," *J. Phys.: Condens. Matter*, vol. 15, pp. 2599–2610, 2003.
- [36] M. Aydin and F. Yakuphanoglu, "Molecular control over Ag/p-Si diode by organic layer," *Journal of Physics and Chemistry of Solids*, vol. 68, pp. 1770–1773, Sept. 2007.
- [37] M. Aydin and F. Yakuphanoglu, "Electrical and interface state density properties of the 4H-nSiC/[6,6]-phenyl C61-butyric acid methyl ester/Au diode," *Microelectronic Engineering*, vol. 85, pp. 1836–1841, Aug. 2008.

- [38] O. Güllü, a. Türüt, and S. Asubay, "Electrical characterization of organic-on-inorganic semiconductor Schottky structures," *Journal of Physics: Condensed Matter*, vol. 20, p. 045215, Jan. 2008.
- [39] D. Zahn, "Transport gap of organic semiconductors in organic modified Schottky contacts," *Applied Surface Science*, vol. 212-213, pp. 423–427, May 2003.
- [40] R. Forrest, M. L. Kaplan, and P. H. Schmidt, "Organic-on-inorganic semiconductor contact barrier diodes . I . Theory with applications to organic thin films and prototype devices," *J. Appl. Phys.*, vol. 55, pp. 1492–1507, 1984.
- [41] S. Antohe, N. Tomozeiu, and S. Gogonea, "Properties of the Organic-on-Inorganic Semiconductor Barrier Contact Diodes In/PTCDI/p-Si and Ag/CuPc/p-Si," *physica status solidi (a)*, vol. 125, no. 1, pp. 397–408, 1991.
- [42] S. R. Forrest, M. L. Kaplan, P. H. Schmidt, and J. M. Parsey, "Organic-on-GaAs contact barrier diodes," *Journal of Applied Physics*, vol. 58, no. 2, p. 867, 1985.
- [43] K. M. Chen, Y. Q. Jia, S. X. Jin, K. Wu, W. B. Zhao, C. Y. Li, Z. N. Gu, and X. H. Zhou, "Heterojunction of solid C<sub>60</sub> and crystalline silicon: rectifying properties and energy-band models," *Journal of Physics: Condens. Matter*, vol. 7, pp. L201–L207, 1995.
- [44] K. Kita, C. Wen, M. Ihara, and K. Yamada, "Photovoltage generation of Si/C<sub>60</sub> heterojunction," *J. Appl. Phys.*, vol. 79, no. August 1995, pp. 2798–2800, 1996.
- [45] E. A. Katz and D. Faiman, "Fullerene Science and Technology A Photovoltaic C<sub>60</sub>/Si Heterojunction," *Fullerene Science and Technology*, vol. 6, no. March 2012, pp. 103–111, 1998.
- [46] N. K. Ojima, M. Y. Amaguchi, and N. I. Shikawa, "Analysis of Photovoltaic Properties of C<sub>63</sub>/Si Heterojunction Solar Cells," *Japanese Journal of Applied Physics*, vol. 39, no. 3, pp. 1176–1179, 2000.
- [47] A. Rogalski, "Infrared detectors: status and trends," *Progress in Quantum Electronics*, vol. 27, no. 2-3, pp. 59–210, 2003.
- [48] M. Casalino, G. Coppola, M. Iodice, I. Rendina, and L. Sirleto, "Near-Infrared Sub-Bandgap All-Silicon Photodetectors: State of the Art and Perspectives," *Sensors*, vol. 10, pp. 10571–10600, 2010.
- [49] Y. Liu, C. W. Chow, W. Y. Cheung, and H. K. Tsang, "In-line channel power monitor based on helium ion implantation in silicon-on-insulator waveguides," *Photonics Technology Letters, IEEE*, vol. 18, no. 17, pp. 1882–1884, 2006.
- [50] T. Baehr-Jones, M. Hochberg, and A. Scherer, "Photodetection in silicon beyond the band edge with surface states," *Optics express*, vol. 16, pp. 1659–68, Feb. 2008.

- [51] H. Chen, X. Luo, and A. W. Poon, "Cavity-enhanced photocurrent generation by 1.55  $\mu\text{m}$  wavelengths linear absorption in a p-i-n diode embedded silicon microring resonator," *Applied Physics Letters*, vol. 95, no. 17, p. 171111, 2009.
- [52] F.D.,Jr. Shepherd and A. C. Yang, "Silicon Schottky retinas for infrared imaging," in *Electron Devices Meeting, 1973 International*, vol. 19, pp. 310–313, 1973.
- [53] F.D.,Jr. Shepherd, "Schottky diode based infrared sensors," *Proceedings of SPIE*, vol. 443, pp. 42–49, 1984.
- [54] P. W. Pellegrini, A. Golubovic, and C. E. Ludington, "Comparison of iridium silicide and platinum silicide photodiodes," *Proceedings of SPIE*, vol. 782, pp. 93–98, 1987.
- [55] T. L. Lin and J. Maserjian, "Novel  $\text{Si}_{1-x}\text{Ge}_x/\text{Si}$  heterojunction internal photoemission long-wavelength infrared detectors," *Applied Physics Letters*, vol. 57, no. 14, pp. 1422–1424, 1990.
- [56] B. V. Zeghbrock, *Principles of Semiconductor Devices*. Boulder: <http://ecee.colorado.edu/~bart/book/book/index.html>, web book ed., 2006.
- [57] D. Meier, H. Davis, A. Shibata, T. Abe, K. Kinoshita, C. Bishop, S. Mahajan, A. Rohatgi, P. Doshi, and M. Finnegan, "Self-doping contacts and associated silicon solar cell structures," *Crystalline Silicon Solar Cells and Technologies, 2nd World conference and exhibition on photovoltaic solar energy conversation*, pp. 1491–1494, 1998.
- [58] S. M. Sze, *Semiconductor Devices, Physics and Technology*. John Wiley & Sons, 2002.
- [59] W. Kern, *Handbook of Semiconductor Wafer Cleaning Technology - Science, Technology, and Applications*. William Andrew Publishing/Noyes, 1993.
- [60] M. Murty and H. A. Atwater, "Silicon epitaxy on hydrogen-terminated Si(001) surfaces using thermal and energetic beams," *Surface Science*, vol. 374, no. 1–3, pp. 283–290, 1997.
- [61] T. Takahagi, I. Nagai, A. Ishitani, H. Kuroda, and Y. Nagasawa, "The formation of hydrogen passivated silicon single-crystal surfaces using ultraviolet cleaning and HF etching," *Journal of Applied Physics*, vol. 64, no. 7, pp. 3516–3521, 1988.
- [62] J. Humenberger, K. Gresslehner, W. Schirz, K. Lischka, and H. Sitter, "Large Area (100)CdTe and CdZnTe Layers on (100)GaAs Grown by Hot Wall Beam Epitaxy for HgCdTe Photovoltaic MWIR-Detectorarray Application," *Mat. Res. Soc. Symp. Proc.*, vol. 216, p. 53, 1990.
- [63] H. Sitter, A. Andreev, G. J. Matt, and N. S. Sariciftci, "Hot-Wall-Epitaxy - The method of choice for the growth of highly ordered organic epilayers," *Mol. Cryst. Liq. Cryst.*, vol. 385, pp. [171]/51–[180]/60, 2002.

- [64] A. Andreev, G. J. Matt, C. J. Brabec, H. Sitter, D. Badt, H. Seyringer, and N. S. Sariciftci, "Highly Anisotropically Self-Assembled Structures of para-Sexiphenyl Grown by Hot-Wall Epitaxy," *Advanced Materials*, vol. 12, no. 9, pp. 629–633, 2000.
- [65] G. J. Matt, T. B. Singh, N. S. Sariciftci, A. Montaigne Ramil, and H. Sitter, "Switching in C<sub>60</sub>-fullerene based field effect transistors," *Applied Physics Letters*, vol. 88, no. 26, p. 263516, 2006.
- [66] M. S. Dresselhaus, G. Dresselhaus, and P. C. Eklund, *Science of fullerenes and carbon nanotubes*. Academic Press, Inc., 1995.
- [67] S. Kobayashi, T. Takenobu, S. Mori, A. Fujiwara, and Y. Iwasa, "Fabrication and characterization of C<sub>60</sub> thin-film transistors with high field-effect mobility," *Applied Physics Letters*, vol. 82, no. 25, pp. 4581–4583, 2003.
- [68] R. W. Lof, M. A. van Veenendaal, B. Koopmans, H. T. Jonkman, and G. A. Sawatzky, "Band gap, excitons, and Coulomb interaction in solid C<sub>60</sub>," *Phys. Rev. Lett.*, vol. 68, pp. 3924–3927, June 1992.
- [69] T. Takahashi, S. Suzuki, T. Morikawa, H. Katayama-Yoshida, S. Hasegawa, H. Inokuchi, K. Seki, K. Kikuchi, K. Ikemoto, and Y. Achiba, "Pseudo-gap at the Fermi level in K<sub>3</sub>C<sub>60</sub> observed by photoemission and inverse photoemission," *Phys. Rev. Lett.*, vol. 68, pp. 1232–1235, Feb. 1992.
- [70] S. Krause, M. B. Casu, A. Schöll, and E. Umbach, "Determination of transport levels of organic semiconductors by UPS and IPS," *New Journal of Physics*, vol. 10, no. 8, p. 85001, 2008.
- [71] S. L. Ren, Y. Wang, A. M. Rao, E. McRae, J. M. Holden, T. Hager, K. Wang, W.-T. Lee, H. F. Ni, J. Selegue, and P. C. Eklund, "Ellipsometric determination of the optical constants of C<sub>60</sub> (Buckminsterfullerene) films," *Applied Physics Letters*, vol. 59, no. 21, pp. 2678–2680, 1991.
- [72] P. C. Eklund, A. M. Rao, Y. Wang, P. Zhou, K.-A. Wang, J. M. Holden, M. S. Dresselhaus, and G. Dresselhaus, "Optical properties of C<sub>60</sub>- and C<sub>70</sub>-based solid films," *Thin Solid Films*, vol. 257, no. 2, pp. 211–232, 1995.
- [73] J. C. Hummelen, B. W. Knight, F. LePeq, F. Wudl, J. Yao, and C. L. Wilkins, "Preparation and Characterization of Fulleroid and Methanofullerene Derivatives," *The Journal of Organic Chemistry*, vol. 60, no. 3, pp. 532–538, 1995.
- [74] H. Hoppe and N. S. Sariciftci, "Organic solar cells: An overview," *Journal of Materials Research*, vol. 19, pp. 1924–1945, Mar. 2011.
- [75] T. Singh, N. Marjanovic, G. J. Matt, S. Gunes, N. Sariciftci, A. Montaigneramil, A. Andreev, H. Sitter, R. Schwodiauer, and S. Bauer, "High-mobility -channel organic field-effect transistors based on epitaxially grown C<sub>60</sub> films," *Organic Electronics*, vol. 6, pp. 105–110, June 2005.

- [76] C. J. Brabec, N. S. Sariciftci, and J. C. Hummelen, "Plastic Solar Cells," vol. 11, no. 1, pp. 15–26, 2001.
- [77] K. M. Chen, "The bias-temperature effect in a rectifying Nb/C<sub>60</sub>/p-Si structure: evidence for mobile negative charges in the solid C<sub>60</sub> film," *J. Phys.: Condens. Matter*, vol. 6, pp. 367–372, 1994.
- [78] C. J. Brabec, A. Cravino, D. Meissner, N. S. Sariciftci, T. Fromherz, M. Minse, L. Sanchez, and J. C. Hummelen, "Origin of the Open Circuit Voltage in Plastic Solar Cells," *Advanced Functional Materials*, vol. 11, no. 5, pp. 374–380, 2001.
- [79] V. D. Mihailetschi, P. W. M. Blom, J. C. Hummelen, and M. T. Rispens, "Cathode dependence of the open-circuit voltage of polymer:fullerene bulk heterojunction solar cells," *Journal of Applied Physics*, vol. 94, no. 10, pp. 6849–6854, 2003.
- [80] N. F. Mott, "Note on the contact between a metal and an insulator or semi-conductor," *Mathematical Proceedings of the Cambridge Philosophical Society*, vol. 34, pp. 568–572, 1938.
- [81] W. Schottky, "Theory of blocking layer and point rectifiers," *Zeitschrift für Physik*, vol. 113, pp. 367–414, 1939.
- [82] S. Suto, K. Sakamoto, and T. Wakita, "Vibrational properties and charge transfer of C<sub>60</sub> adsorbed on Si(111)-(7x7) and Si(100)-(2x1) surfaces," *Physical Review B*, vol. 56, no. 12, pp. 7439–7445, 1997.
- [83] E. J. Meijer, D. M. de Leeuw, S. Setayesh, E. van Veenendaal, B. H. Huisman, P. W. M. Blom, J. C. Hummelen, U. Scherf, J. Kadam, and T. M. Klapwijk, "Solution-processed ambipolar organic field-effect transistors and inverters.," *Nature materials*, vol. 2, pp. 678–82, Oct. 2003.
- [84] M. Scharber, D. Mühlbacher, M. Koppe, P. Denk, C. Waldauf, A. Heeger, and C. J. Brabec, "Design Rules for Donors in Bulk-Heterojunction Solar Cells—Towards 10% Energy-Conversion Efficiency," *Advanced Materials*, vol. 18, pp. 789–794, Mar. 2006.
- [85] C. M. Cardona, W. Li, A. E. Kaifer, D. Stockdale, and G. C. Bazan, "Electrochemical Considerations for Determining Absolute Frontier Orbital Energy Levels of Conjugated Polymers for Solar Cell Applications," pp. 2367–2371, 2011.
- [86] I. G. Hill, A. Rajagopal, A. Kahn, and Y. Hu, "Molecular level alignment at organic semiconductor-metal interfaces," *Applied Physics Letters*, vol. 73, no. 5, p. 662, 1998.
- [87] I. Hill, "Organic semiconductor interfaces: electronic structure and transport properties," *Applied Surface Science*, vol. 166, pp. 354–362, Oct. 2000.
- [88] W. Shockley and W. T. Read, "Statistics of the Recombinations of Holes and Electrons," *Phys. Rev*, vol. 87, no. 5, pp. 835–842, 1952.

- [89] H. Veloric and M. Prince, "High-Voltage Conductivity-Modulated Silicon Rectifier," *The Bell System Technical Journal*, vol. 36, pp. 975–1004, 1957.
- [90] J. L. Moll, "The Evolution of the Theory for the Voltage-Current Characteristic of P-N Junctions," *Proceedings of the IRE*, vol. 46, pp. 1076–1082, June 1958.
- [91] R. Schmechel, "Gaussian disorder model for high carrier densities: Theoretical aspects and application to experiments," *Physical Review B*, vol. 66, p. 235206, 2002.
- [92] V. V. Afanas'ev, *Internal Photoemission Spectroscopy Principles and Applications*. Elsevier Ltd, 2008.
- [93] R. H. Fowler, "The Analysis of Photoelectric Sensitivity Curves for Clean Metals at Various Temperatures," *Phys. Rev.*, vol. 38, pp. 45–56, July 1931.
- [94] J. W. P. Hsu, Y. L. Loo, D. V. Lang, and J. a. Rogers, "Nature of electrical contacts in a metal–molecule–semiconductor system," *Journal of Vacuum Science & Technology B: Microelectronics and Nanometer Structures*, vol. 21, no. 4, p. 1928, 2003.
- [95] J. W. P. Hsu, D. V. Lang, K. W. West, Y.-I. Loo, and M. D. Halls, "Probing Occupied States of the Molecular Layer in Au-Alkanedithiol-GaAs Diodes," *Society*, pp. 5719–5723, 2005.
- [96] V. V. Afanasev and A. Stesmans, "Interfacial Defects in SiO<sub>2</sub> Revealed by Photon Stimulated Tunneling of Electrons," *Physical Review Letters*, pp. 2437–2440, 1997.
- [97] K. Harigaya, "Lattice distortion and energy-level structures in doped C<sub>60</sub> and C<sub>70</sub> molecules studied with the extended Su-Schrieffer-Heeger model: Polaron excitations and optical absorption," *Phys. Rev. B*, vol. 45, pp. 13676–13684, June 1992.
- [98] B. Friedman, "Electronic absorption spectra in C<sub>60</sub><sup>-</sup> and C<sub>60</sub><sup>+</sup>," *Phys. Rev. B*, vol. 48, pp. 2743–2747, July 1993.
- [99] D. Dick, X. Wei, S. Jeglinski, R. E. Benner, Z. V. Vardeny, D. Moses, V. I. Srdanov, and F. Wudl, "Transient Spectroscopy of Excitons and Polarons in C<sub>60</sub> Films from Femtoseconds to Milliseconds," *Phys. Rev. Lett.*, vol. 73, pp. 2760–2763, Nov. 1994.
- [100] M. Lenes, G.-J. A. H. Wetzelaer, F. B. Kooistra, S. C. Veenstra, J. C. Hummelen, and P. W. M. Blom, "Fullerene Bisadducts for Enhanced Open-Circuit Voltages and Efficiencies in Polymer Solar Cells," *Advanced Materials*, vol. 20, no. 11, pp. 2116–2119, 2008.
- [101] T. D. Anthopoulos, F. B. Kooistra, H. J. Wondergem, D. Kronholm, J. C. Hummelen, and D. M. de Leeuw, "Air-Stable n-Channel Organic Transistors Based on a Soluble C<sub>84</sub> Fullerene Derivative," *Advanced Materials*, vol. 18, pp. 1679–1684, July 2006.

- [102] M. G. Mason, C. W. Tang, L. S. Hung, P. Raychaudhuri, J. Madathil, D. J. Giesen, L. Yan, Q. T. Le, Y. Gao, S.-T. Lee, L. S. Liao, L. F. Cheng, W. R. Salaneck, D. A. dos Santos, and J. L. Bredas, "Interfacial chemistry of Alq<sub>3</sub> and LiF with reactive metals," *Journal of Applied Physics*, vol. 89, no. 5, pp. 2756–2765, 2001.
- [103] D. Grozea, A. Turak, X. D. Feng, Z. H. Lu, D. Johnson, and R. Wood, "Chemical structure of Al/LiF/Alq interfaces in organic light-emitting diodes," *Applied Physics Letters*, vol. 81, no. 17, pp. 3173–3175, 2002.
- [104] Q. T. Le, L. Yan, Y. Gao, M. G. Mason, D. J. Giesen, and C. W. Tang, "Photoemission study of aluminum/tris-(8-hydroxyquinoline) aluminum and aluminum/LiF/tris-(8-hydroxyquinoline) aluminum interfaces," *Journal of Applied Physics*, vol. 87, no. 1, pp. 375–379, 2000.
- [105] E. D. Glowacki, K. L. Marshall, C. W. Tang, and N. S. Sariciftci, "Doping of organic semiconductors induced by lithium fluoride/aluminum electrodes studied by electron spin resonance and infrared reflection-absorption spectroscopy," *Applied Physics Letters*, vol. 99, no. 4, p. 043305, 2011.
- [106] L. S. Hung, C. W. Tang, and M. G. Mason, "Enhanced electron injection in organic electroluminescence devices using an Al/LiF electrode," *Applied Physics Letters*, vol. 70, no. 2, pp. 152–154, 1997.
- [107] T. Mori, H. Fujikawa, S. Tokito, and Y. Taga, "Electronic structure of 8-hydroxyquinoline aluminum/LiF/Al interface for organic electroluminescent device studied by ultraviolet photoelectron spectroscopy," *Applied Physics Letters*, vol. 73, no. 19, pp. 2763–2765, 1998.
- [108] G. Parthasarathy, C. Shen, A. Kahn, and S. R. Forrest, "Lithium doping of semiconducting organic charge transport materials," *Journal of Applied Physics*, vol. 89, no. 9, pp. 4986–4992, 2001.
- [109] P. A. Heiney, J. E. Fischer, A. R. McGhie, W. J. Romanow, A. M. Denenstien, J. P. McCauley Jr., A. B. Smith, and D. E. Cox, "Orientational ordering transition in solid C<sub>60</sub>," *Phys. Rev. Lett.*, vol. 66, pp. 2911–2914, June 1991.
- [110] M. Hirose, N. Altaf, and T. Arizumi, "Contact Properties of Metal-Silicon Schottky Barriers," *Japanese Journal of Applied Physics*, vol. 9, no. 3, pp. 260–264, 1970.
- [111] P. Stadler, A. M. Track, M. Ullah, H. Sitter, G. J. Matt, G. Koller, T. B. Singh, H. Neugebauer, N. Serdar Sariciftci, and M. G. Ramsey, "The role of the dielectric interface in organic transistors: A combined device and photoemission study," *Organic Electronics*, vol. 11, pp. 207–211, Feb. 2010.
- [112] L.-L. Chua, P. K. H. Ho, H. Sirringhaus, and R. H. Friend, "High-stability ultrathin spin-on benzocyclobutene gate dielectric for polymer field-effect transistors," *Applied Physics Letters*, vol. 84, no. 17, pp. 3400–3402, 2004.
- [113] G. J. Matt, M. Bednorz, and et. al., "Unpublished results," 2012.

- [114] P. Stadler, "Doctoral thesis," Johannes Kepler University Linz, Austria 2011.
- [115] X. He, H. Liu, Y. Li, Y. Liu, F. Lu, Y. Li, and D. Zhu, "A New Copolymer Containing Perylene Bisimide and Porphyrin Moieties : Synthesis and Characterization," vol. 206, no. 21, pp. 2199–2205, 2005.
- [116] J.-W. Lee, H.-S. Kang, M.-K. Kim, K. Kim, M.-Y. Cho, Y.-W. Kwon, J. Joo, J.-I. Kim, and C.-S. Hong, "Electrical characteristics of organic perylene single-crystal-based field-effect transistors," *Journal of Applied Physics*, vol. 102, no. 12, p. 124104, 2007.
- [117] K. Rostalski and D. Meissner, "Photocurrent spectroscopy for the investigation of charge carrier generation and transport mechanisms in organic p / n-junction solar cells," *Solar Energy Materials*, vol. 63, pp. 37–47, 2000.
- [118] S. Ferrere and B. a. Gregg, "New perylenes for dye sensitization of TiO<sub>2</sub>," *New Journal of Chemistry*, vol. 26, pp. 1155–1160, Aug. 2002.
- [119] P. R. L. Malenfant, C. D. Dimitrakopoulos, J. D. Gelorme, L. L. Kosbar, T. O. Graham, A. Curioni, and W. Andreoni, "N-type organic thin-film transistor with high field-effect mobility based on a N,N[<sup>sup</sup>']-dialkyl-3,4,9,10-perylene tetracarboxylic diimide derivative," *Applied Physics Letters*, vol. 80, no. 14, p. 2517, 2002.
- [120] B. a. Jones, M. J. Ahrens, M.-H. Yoon, A. Facchetti, T. J. Marks, and M. R. Wasielewski, "High-mobility air-stable n-type semiconductors with processing versatility: dicyanoperylene-3,4:9,10-bis(dicarboximides).," *Angewandte Chemie (International ed. in English)*, vol. 43, pp. 6363–6, Nov. 2004.
- [121] M. Irimia-Vladu, P. a. Troshin, M. Reisinger, L. Shmygleva, Y. Kanbur, G. Schwabegger, M. Bodea, R. Schwödauier, A. Mumyatov, J. W. Fergus, V. F. Razumov, H. Sitter, N. S. Sariciftci, and S. Bauer, "Biocompatible and Biodegradable Materials for Organic Field-Effect Transistors," *Advanced Functional Materials*, vol. 20, pp. 4069–4076, Dec. 2010.
- [122] J. E. Anthony, A. Facchetti, M. Heeney, S. R. Marder, and X. Zhan, "n-Type organic semiconductors in organic electronics.," *Advanced materials*, vol. 22, pp. 3876–92, Sept. 2010.
- [123] J. B. Gustafsson, E. Moons, S. M. Widstrand, and L. S. O. Johansson, "Thin PTCDA films on Si(0 0 1): 1.Growth mode," *Surface Science*, vol. 572, no. 1, pp. 23–31, 2004.
- [124] I. Thurzo, H. Mendez, and D. Zahn, "Dielectric relaxation in a hybrid Ag/DiMe-PTCDI/GaAs device," *Journal of Non-Crystalline Solids*, vol. 351, pp. 2003–2008, Aug. 2005.
- [125] M. Ullah, I. I. Fishchuk, A. Kadashchuk, P. Stadler, A. Pivrikas, C. Simbrunner, V. N. Poroshin, N. S. Sariciftci, and H. Sitter, "Dependence of Meyer–Neldel energy on energetic disorder in organic field effect transistors," *Applied Physics Letters*, vol. 96, no. 21, p. 213306, 2010.



- [126] M. Ullah, A. Pivrikas, I. I. Fishchuk, A. Kadashchuk, P. Stadler, C. Simbrunner, N. S. Sariciftci, and H. Sitter, "Electric field and grain size dependence of Meyer–Neldel energy in C<sub>60</sub> films," *Synthetic Metals*, vol. 161, no. 17–18, pp. 1987–1990, 2011.
- [127] T. U. Kampen, G. Gavrilă, H. Méndez, D. R. T. Zahn, A. R. Vearey-Roberts, D. A. Evans, J. Wells, I. McGovern, and W. Braun, "Electronic properties of interfaces between perylene derivatives and GaAs(001) surfaces," *Journal of Physics: Condensed Matter*, vol. 15, no. 38, p. S2679, 2003.
- [128] H. E. Katz and J. Huang, "Thin-Film Organic Electronic Devices," *Annual Review of Materials Research*, vol. 39, no. 1, pp. 71–92, 2009.
- [129] H. Nyquist, "Thermal Agitation of Electric Charge in Conductors," *Phys. Rev.*, vol. 32, no. 1, pp. 110–113, 1928.
- [130] P. R. L. Malenfant, C. D. Dimitrakopoulos, J. D. Gelorme, L. L. Kosbar, T. O. Graham, A. Curioni, and W. Andreoni, "N-type organic thin-film transistor with high field-effect mobility based on a N,N'-dialkyl-3,4,9,10-perylene tetracarboxylic diimide derivative," *Applied Physics Letters*, vol. 80, no. 14, pp. 2517–2519, 2002.
- [131] G. Ginev, T. Riedl, R. Parashkov, H.-H. Johannes, and W. Kowalsky, "Organic-GaAs heterostructure diodes for microwave applications," *Applied Surface Science*, vol. 234, no. 1-4, pp. 22–27, 2004.
- [132] E. D. Glowacki, L. Leonat, G. Voss, M. Bodea, Z. Bozkurt, M. Irimia-Vladu, S. Bauer, and N. S. Sariciftci, "Natural and nature-inspired semiconductors for organic electronics," *Proc. of SPIE*, vol. 8118, pp. 81180M–1, 2011.
- [133] M. Irimia-Vladu, E. D. Glowacki, P. a. Troshin, G. Schwabegger, L. Leonat, D. K. Susarova, O. Krystal, M. Ullah, Y. Kanbur, M. a. Bodea, V. F. Razumov, H. Sitter, S. Bauer, and N. S. Sariciftci, "Indigo - A Natural Pigment for High Performance Ambipolar Organic Field Effect Transistors and Circuits," *Advanced Materials*, vol. 24, pp. 375–380, Nov. 2011.
- [134] A. Baeyer and V. Drewsen, "Darstellung von Indigblau aus Orthonitrobenzaldehyd," *Berichte der deutschen chemischen Gesellschaft*, vol. 15, no. 2, pp. 2856–2864, 1882.
- [135] W. Lüttke and M. Klessinger, "Theoretische und spektroskopische Untersuchungen an Indigofarbstoffen, I. Infrarot- und Lichtabsorptionsspektren einfacher Indigofarbstoffe," *Chemische Berichte*, vol. 97, no. 8, pp. 2342–2357, 1964.
- [136] E. Steingruber, *Indigo and Indigo Colorants*. Ullmann's Encyclopedia of Industrial Chemistry, 2004.
- [137] C. J. Cooksey, "Tyrian Purple: 6,6'-Dibromoindigo and Related Compounds," *Molecules*, vol. 6, pp. 736–769, 2001.

- [138] G. Voß and H. Gerlach, "Regioselektiver Brom/Lithium-Austausch bei 2,5-Dibrom-1-nitrobenzol. Eine einfache Synthese von 4-Brom-2-nitrobenzaldehyd und 6,6'-Dibromindigo," *Chemische Berichte*, vol. 122, no. 6, pp. 1199–1201, 1989.
- [139] Y. Kanbur, M. Irimia-Vladu, E. D. Glowacki, G. Voss, M. Baumgartner, G. Schwabegger, L. Leonat, M. Ullah, H. Sarica, S. Erten-Ela, R. Schwödiauer, H. Sitter, Z. Küçükyavuz, S. Bauer, and N. S. Sariciftci, "Vacuum-processed polyethylene as a dielectric for low operating voltage organic field effect transistors," *Organic Electronics*, vol. 13, pp. 919–924, May 2012.
- [140] E. D. Glowacki, L. Leonat, G. Voss, M.-A. Bodea, Z. Bozkurt, A. M. Ramil, M. Irimia-Vladu, S. Bauer, and N. S. Sariciftci, "Ambipolar organic field effect transistors and inverters with the natural material Tyrian Purple," *AIP Advances*, vol. 1, no. 4, p. 042132, 2011.
- [141] T. Kampen, H. Mendez, and D. R. T. Zahn, "Energy Level Alignment at Molecular Semiconductor/GaAs(100) Interfaces: Where is the LUMO?," *26th ICPS, IOP Conf. Series 171*, p. H215, 2003.
- [142] G. J. Matt, T. Fromherz, M. Bednorz, H. Neugebauer, N. S. Sariciftci, and G. Bauer, "Fullerene sensitized silicon for near- to mid-infrared light detection," *Physica Status Solidi (B)*, vol. 247, pp. 3043–3046, Dec. 2010.
- [143] H. R. Philipp and E. A. Taft, "Optical Constants of Silicon in the Region 1 to 10 eV," *Phys. Rev.*, vol. 120, pp. 37–38, Oct. 1960.
- [144] *Taken from the library of the optical constants of various materials at the Department of Optoelectronics*. Gliwice, Poland: Silesian University of Technology.
- [145] M. Friedrich, C. Himcinschi, G. Salvan, M. Anghel, A. Paraian, T. Wagner, T. U. Kampen, and D. R. T. Zahn, "VASE and IR spectroscopy: excellent tools to study biaxial organic molecular thin films: DiMe-PTCDI on S-passivated GaAs(100)," *Thin Solid Films*, vol. 455–456, no. 0, pp. 586–590, 2004.
- [146] P. Yeh, *Optical waves in layered media*. Wiley series in pure and applied optics, Wiley, 1988.
- [147] E. H. Rhoderick, "Metal-semiconductor contacts," *Solid-State and Electron Devices, IEE Proceedings I*, vol. 129, p. 1, Feb. 1982.
- [148] D. K. Schroder, *Semiconductor material and device characterization*. John Wiley & Sons, Inc., third ed., 2006.
- [149] J. M. Andrews and M. P. Lepselter, "Reverse current-voltage characteristics of metal-silicide Schottky diodes," *Solid-State Electronics*, vol. 13, no. 7, pp. 1011–1023, 1970.

# Curriculum vitae

## **Mateusz Andrzej Bednorz**

Address: Blütenstraße 23/164  
A4040 Linz, Austria  
Cell Phone: +436803219759  
Email: mateusz.bednorz@jku.at



## **Personal Details**

Nationality: Polish  
Date of birth: 17<sup>th</sup> July 1981  
Place of birth: Gliwice, Poland

## **Education**

**09.2000–06.2005**

Silesian University of Technology, Gliwice, Poland

Faculty of Mathematics and Physics

Course: Technical Physics

Specialization: Optoelectronics

Degree: MSc. Eng., with Honours, GPA - 4.79 (out of 5.0)

Master Thesis: Development of optoelectronic toxic gas sensor

**03.2008–03.2013** Dissertation at the Institute of Semiconductor and Solid State Physics, Johannes Kepler University Linz, Austria

## **Other occupation in R&D**

- 2004 - Summer training at Institute of Low Temperature and Structure Research Polish Academy of Science in Wrocław
- 2005 - 2007 Research Assistant at Department of Optoelectronics, of Institute of Physics, Silesian University of Technology, Gliwice, Poland

## **Research interest**

inorganic-organic hybrid heterojunctions, photodetectors, internal photoemission spectroscopy, organic electronics, organic photovoltaics, integrated optics, computer modelling and measurements of optical waveguides, thin films technology, optical gas sensors, polymer thin films in gas sensor applications

## Awards and scholarships

- Scholarship and Award of the Dean for good marks, during all years of Master studies
- Scholarship of Polish Ministry of Education 2004/2005 for excellent achievements in the field of studies
- Award of 2<sup>nd</sup> kind at XIV Adam Smoliński Polish Contest for the best Master Thesis in the field of Optoelectronics, 2004/2005
- First Award for the Young Scientist for the best Poster at Advanced Laser Technologies Conference, 9-12.09.2006 Brasov, Romania

## Important publications

- E. Maciak, Z. Opilski, T. Pustelny, M. Bednorz, "An optical detection of NH<sub>3</sub> gas by means of a WO<sub>3</sub> thin films based on surface plazmon resonance technique," *Journal de Physique IV*, vol. 129, p.131–136, 2005
- M. Bednorz, A. Stolarczyk, E. Maciak, T. Pustelny, Z. Opilski, M. Urbańczyk, "Influence of humidity variations on performance of Nafion based ammonia optical sensor," *Journal de Physique IV*, vol. 137, p.23–29, 2006
- M. Bednorz, M. Urbańczyk, T. Pustelny, A. Piotrowska, E. Papis, Z. Sidor, E. Kamińska, , "Application of SU8 polymer in waveguide interferometer ammonia sensor," *Molecular and Quantum Acoustics*, vol. 27, p.31–40, 2006
- G. J. Matt, T. Fromherz, M. Bednorz, S. Zamiri, G. Goncalves, C. Lungenschmied , D. Meissner, H. Sitter, N. S. Sariciftci, C. J. Brabec, G. Bauer, "Fullerene sensitized silicon for near- to mid-infrared light detection," *Advanced Materials*, vol. 22, p.647–650, 2010
- G. J. Matt, T. Fromherz, M. Bednorz, H. Neugebauer, N. S. Sariciftci, G. Bauer, "Fullerene sensitized silicon for near- to mid-infrared light detection," *Physica Status Solidi*, vol. 247, p.3043–3046, 2010
- "Extending Absorption," *Research Highlights Nature Photonics*, vol. 4, p.128, 2010
- M. C. Scharber, C. Lungenschmied, H. J. Egelhaaf, G. J. Matt, M. Bednorz, T. Fromherz, J. Gao, D. Jarzab and M. A. Loi, "Charge transfer excitons in low band gap polymer based solar cells and the role of processing additives," *Energy & Environmental Science*, vol. 4, p.5077–5083, 2011
- M. Bednorz, T. Fromherz, G. J. Matt, C. J. Brabec, M. C. Scharber, N. S. Sariciftci, "Electrical properties of pSi/[6,6] phenyl-C61 butyric acid methyl ester/Al hybrid heterojunctions: Experimental and theoretical evaluation of diode operation," *Journal of Applied Physic*, vol. 112, p.114508, 2012

- M. Bednorz, G. J. Matt, E. Głowacki, T. Fromherz, C. J. Brabec, M. C. Scharber, H. Sitter, N. S. Sariciftci, "Silicon/organic hybrid heterojunction based IR photodetector operating in the telecom regime," *Accepted for print in Organic Electronics*

## Conference presentations

- February, 2005 Ustroń, Poland, Winter Workshop on Acoustoelectronics and Optoelectronics WoA&O, Oral presentation: "Investigation of interferometric structures in gas sensor applications"
- February, 2006 Ustroń, Poland, Winter Workshop on Acoustoelectronics and Optoelectronics WoA&O, Oral presentation: "New approaches in optical toxic gas sensors"
- September 2006, Brasov, Romania, Advanced Laser Technologies Conference, Poster presentation
- February, 2007 Wisła, Poland, 36 Winter School on Wave and Quantum Acoustics, Oral presentation: "Application of SU8 polymer in waveguide interferometer ammonia sensor"
- May 2007, Wrocław, Poland, International Meeting of SPIE Student Chapters, Oral presentation: "Application of SU8 polymer in waveguide interferometer ammonia sensor"
- August 2008, Rome, Italy, The 22<sup>nd</sup> Conference of the Condensed Matter Div. of the European Physical Society, Poster presentation
- June 2009, Strasbourg, France, E-MRS Spring Meeting, Poster presentation
- March 2010, Plannersalm, Austria, 5<sup>th</sup> Winterschool on Organic Electronics, Oral presentation: "Detection of near to mid infrared light with an organic/inorganic hybrid hetero-junction"
- April 2011, San Francisco, USA, MRS Spring Meeting, Oral presentation: "Room Temperature Detection of Light at 1.55  $\mu\text{m}$  using C<sub>60</sub> Based Devices"
- March 2012, Plannersalm, Austria, 6<sup>th</sup> Winterschool on Organic Electronics, Oral presentation: "Silicon/organic hybrid heterojunction infrared photodetector operating at room temperature in the telecommunication range"
- April 2012, San Francisco, USA, MRS Spring Meeting, Oral presentation: "Silicon/organic hybrid heterojunction infrared photodetector operating at room temperature in the telecommunication range"

## **Social activities**

Former President of Students Chapter of SPIE at the Silesian University of Technology

## **Skills**

Languages:

English: Fluent

German: Very Good

Polish: Mother tongue

Czech: Very Good passive, conversant active

Slovak: Very Good passive, conversant active

PC skills: MatLab, AutoCad, LabView, Origin, Optiwave Software(OptiFDTD, OptiBPM), Delphi, Pascal, MsOffice

## **Hobbies**

Sports(mountain bike cycling, skiing, mountain hiking, jogging), History